UCL Université catholique de Louvain

École polytechnique de Louvain (EPL)

# Magnetic and magnetotransport properties of 3D interconnected NiCo/Cu and Co/Cu multilayered nanowire networks

Dissertation presented by
**Joséphine LEBRUN**

for obtaining the Master's degree in
**Chemical and Materials Engineering**

Supervisor
**Luc PIRAUX**

Readers
**Tristan DA CÂMARA SANTA CLARA GOMES, Benoit HACKENS**

Academic year 2017-2018

# *Acknowledgements*

After one year of work in the laboratory of the second floor of the Boltzmann building, I would really like to thank all the people who supported and guided me, who were present during my master thesis. I had the chance to be surrounded with smiling people, always ready to help me.

First of all, I would like to thank my supervisor *Professor Luc Piraux* for his presence, his assistance and encouragements. Likewise, I would like to thank *Tristan da Camara*. Without him I could not have accomplished nor learned as much as I did during this master thesis. I am grateful for his presence, answers, advice and re-lecture; I really enjoyed learning at his side. I am also grateful for the help of *Yenni Velasquez*. Each time the AGM was not working, she was there to help me and retry the measurement again and again. I also had the opportunity to be accompagnied by Tristan or Yenni during the SEM session were I received information and more details on the working principle of the machine, and the structure of the analysed nanowires. Thanks for everything.

Furthermore, I would like to thank *Kyara Hallet* whom I was working with. She was present to discuss some good (or strange) results and helped me to make some measurements when problems arised.

Finally, I would like to thank my familly for giving me the opportunity to pursue my very interesting studies. I am very grateful to *Philippe Greiner* at my side for his support, accurate re-lecture, and English corrections.

*Joséphine* LEBRUN

*Louvain-la-Neuve, June 2018*

# *Abstract*

**Magnetic and magnetotransport properties of 3D interconnected NiCo/Cu and Co/Cu multilayered nanowire networks**

by Joséphine LEBRUN

Magnetic nanowires present a new field of research. Nanowire networks are studied because of their interesting properties and great potential in numerous applications including data storage, high frequency devices, microwave absorption, resistive switching memories, as well as catalyser, medical devices and batteries. More and more fabrication techniques are developed, always looking to improve their properties. Electrodeposition appears to be an elegant, versatile and cheap method to create nanowire networks. It allows for measurements in the current perpendicular to plane geometry thanks to a template made of a porous polycarbonate membrane.

Multilayered crossed nanowire networks show interesting giant magnetoresistance properties. To study these properties, it is necessary to observe the magnetic behaviour first. In the case of nanowires, this behaviour is mainly governed by shape anisotropy and dipolar interactions. These properties are present both at individual nanowire level and at network level. As a consequence, the characterisation of the individual and global properties of the networks is of utmost importance to understand the behaviour correctly before producing new devices.

This master thesis is the continuity of a previous work studying Nickel-Cobalt/Copper multilayered crossed nanowires [44]. Very high giant magnetoresistance values were obtained, but those could not be reproduced reliably. The samples presented in this work show stable and reproducible results but with slightly reduced GMR values. The electrodeposition uses electrolytes with lower concentrations of materials than in the previous work. These electrolytes were elaborated to enable homogeneous depositions without blocking the templates' pores. The results are satisfying, as good GMR results are obtained with low sample-to-sample variability. The multilayered crossed nanowires are made of ferromagnetic layers composed of Cobalt or Cobalt-Nickel alloys, and non-magnetic layers composed of Copper. The composition of the ferromagnetic layers is analysed with a scanning electron microscope. Two types of templates are used, with different porosities and nanowire diameters. For the higher porosity template, Cobalt appears to be better suited. For the lower porosity template, the Nickel-Cobalt alloy delivers higher giant magnetoresistance values – and even more so at low temperature.

*Keywords:* magnetism, giant magnetoresistance, magnetic anisotropy, hysteresis, dipolar coupling, nanowires, ferromagnetism, 3D nanostructure

# Table of Contents

**Acknowledgements** i

**Abstract** iii

**Table of Contents** v

**List of Abbreviations** vii

**List of Symbols** ix

**Introduction** 1

**1 State of the art** 3
- 1.1 Ferromagnetism in 3d transition metals . . . 3
  - 1.1.1 Magnetic Properties . . . 3
  - 1.1.2 Electric and magneto-electric properties . . . 17
  - 1.1.3 Giant Magnetoresistance . . . 22
- 1.2 Ferromagnetic nanowire network . . . 26
  - 1.2.1 Fabrication process . . . 27
  - 1.2.2 Single nanowires . . . 30
  - 1.2.3 Parallel nanowire arrays . . . 34
  - 1.2.4 Crossed nanowire networks . . . 39

**2 Synthesis and characterisation of interconnected multilayer nanowire networks** 45
- 2.1 Synthesis of a 3D network . . . 45
- 2.2 Composition and morphology characterisation - SEM . . . 49
- 2.3 Magnetic characterisation - AGM . . . 54
- 2.4 Magnetotransport characterisation - AMR and GMR . . . 56

**3 Results and discussion** 61
- 3.1 $Ni_{50}Co_{50}$/Cu multilayer crossed nanowire networks . . . 61
  - 3.1.1 Optimisation of the electrolyte . . . 61
  - 3.1.2 High porosity template . . . 66
  - 3.1.3 Low porosity template . . . 70
- 3.2 $Ni_{25}Co_{75}$/Cu multilayer crossed nanowire networks . . . 71
  - 3.2.1 High porosity template . . . 71
  - 3.2.2 Low porosity template . . . 73
- 3.3 Co/Cu multilayer crossed nanowire networks . . . 74
  - 3.3.1 Optimisation of the electrolyte . . . 77
  - 3.3.2 High porosity template . . . 79
  - 3.3.3 Low porosity template . . . 82
- 3.4 Summary of the magnetotransport results . . . 90

**Conclusion and perspectives** 93

**A Appendix A** **97**
A.1 Diamagnetism and paramagnetism . . . . . 97
A.2 Ferromagnetism . . . . . 100
A.3 GMR . . . . . 103
A.3.1 Development of the GMR definition . . . . . 103
A.3.2 Models for GMR measurements . . . . . 104

**Bibliography** **107**

# List of Abbreviations

| | |
|---|---|
| 2D | Two-dimensional |
| 3D | Three-dimensional |
| 40nm NWs | Nanowires with diameter of 40 nanometres |
| $\mu$m | Micrometer (unit) |
| $\mu$W | Microwatt (unit) |
| $\Omega$ | Ohm (unit) |
| A | Ampere (unit) |
| Ag | Silver (element) |
| AgCl | Silver chloride |
| AGM | Alternating gradient field magnetometer |
| AMR | Anisotropic magnetoresistance |
| Ar | Argon (element) |
| Au | Gold (element) |
| bcc | Body-centred cubic |
| C | Coulomb (unit) |
| Co | Cobalt (element) |
| $CoSO_4$ | Cobalt(II) sulphate |
| Cr | Chromium (element) |
| Cu | Copper (element) |
| cos | Cosine |
| CGS | "Centimetre, gramme, second" unit system |
| CNWs | Crossed nanowires |
| CPP | Current perpendicular to plane configuration |
| DOS | Density of States |
| EPL | Ecole Polytechnique de Louvain |
| EDX | Energy-dispersive X-ray spectroscopy analysis system |
| F | Ferromagnetic layer |
| fcc | Face-centered cubic |
| Fe | Iron (element) |
| $FeSO_4$ | Iron(II) sulphate |
| FE-SEM | Field-emission scanning electron microscope |
| g | Gram (unit) |
| GMR | Giant magnetoresistance |
| Gs | Gauss (unit) |
| $H_2O$ | Water |
| $H_2SO_4$ | Sulphuric acid |
| $H_3BO_3$ | Boric acid |
| hcp | Hexagonal close-packed |
| $I_2$:KI | Iodine-based etching solution |
| IP | In plane |
| J | Joules |
| K | Kelvin (unit) |
| k$\Omega$ | Kilo Ohm (unit) |

| | |
|---|---|
| kg | Kilogram (unit) |
| kOe | Kilo Oersted (unit) |
| l | Litre (unit) |
| LT | Low temperature |
| m | Meter (unit) |
| M | Metal |
| M | Molar (unit) |
| mm | Millimetre (unit) |
| MR | Magnetoresistance |
| ms | Millisecond (unit) |
| N | Non-magnetic |
| nA | Nano Ampere (unit) |
| NaOH | Sodium hydroxide |
| Ni | Nickel (element) |
| NiCo | Nickel-cobalt alloy |
| $NiSO_4$ | Nickel(II) sulfate |
| $Ni(SO_3NH_2)_2$ | Nickel-II-sulphamate |
| nm | Nanometer (unit) |
| NTs | Nanotubes |
| NW | Nanowire |
| NWs | Nanowires |
| Oe | Oersted (unit) |
| OOP | Out of plane |
| PC | Polycarbonate |
| pH | "Potentiel hydrogène" measuring the acidity |
| Pt | Platinum |
| Ref | Reference |
| RT | Room temperature |
| s | Second (unit) |
| SI | International unit system |
| sin | Sinus |
| T | Temperature |
| TEM | Transmission Electron Microscopy |
| TMR | Tunnelling magnetoresistance |
| UCL | Catholic University of Louvain |
| V | Volt (unit) |
| W | Watt (unit) |
| XR | X rays |
| XRD | X-ray diffraction |
| ZAF | Algorithms using the atomic number Z, the absorbance A and the fluorescence F |

# List of Symbols

| | |
|---|---|
| $\pm$ | More or less |
| $\alpha$, $\beta$, $\gamma$, $\theta$, $\phi$ | Angles |
| $\alpha$ | Spin asymmetry coefficient |
| $\alpha$ | Angle of a nanowire axis with the template normal |
| $\alpha_{max}$ | Maximal angle of a nanowire axis with the template normal |
| $\beta$ | Azimuthal angle between the nanowire and the direction of the magnetic field applied in-plane. |
| $\theta$ | Angle of a nanowire axis with direction of the magnetic field applied in-plane. |
| $\delta$ | Wall thickness |
| $\epsilon$ | Error inferior to the half of the last significant number chosen |
| $\epsilon_F$ | Fermi energy |
| $\lambda$ | Radiation wavelength |
| $\rho$ | Resistivity |
| $\rho_\uparrow$ | Resistivity contribution of majority electrons |
| $\rho_\downarrow$ | Resistivity contribution of majority electrons |
| $\rho_\parallel$ | Resistivity when the magnetisation is parallel to the current |
| $\rho_\perp$ | Resistivity when the magnetisation is perpendicular to the current |
| $\rho_\perp^{OOP}$ | Resistivity when the magnetisation is perpendicular to the current computed from measurement with magnetic field in the out-of-plane direction |
| $\rho_\perp^{IP}$ | Resistivity when the magnetisation is perpendicular to the current computed from measurement with magnetic field in the in-plane direction |
| $\rho_0$ | Resistivity of a demagnetised sample |
| $\rho_\mu$ | Resistivity expressed in $\mu\Omega$cm |
| $\rho_{av}$ | Averaged resistivity of a demagnetised sample |
| $\rho_M$ | Resistivity from electron-spin scattering |
| $\rho_L$ | Resistivity from electron-phonon interaction |
| $\rho_r$ | Residual resistivity |
| $\rho_i$ | Ideal resistivity |
| $\bar{\rho}_{IP}$ | Resistivity when the magnetisation saturated in in-plane direction |
| $\bar{\rho}_{OOP}$ | Resistivity when the magnetisation saturated in out-of-plane direction |
| $\rho_P$ | Resistivity in parallel ferromagnetic layers configuration |
| $\sigma$ | Conductivity |
| $\sigma_\uparrow$ | Conductivity contribution of majority electrons |
| $\sigma_\downarrow$ | Conductivity contribution of minority electrons |
| $\tau$ | Relaxation time |
| $\chi$ | Magnetic susceptibility |
| $\mu_0$ | Vacuum permeability |
| $\mu_B$ | Bohr magneton |

| | |
|---|---|
| $a$ | Lattice parameter |
| $A$ | Atomic mass |
| $AMR$ | Anisotropic magnetoresistance value |
| $AMR^{OOP}$ | Anisotropic magnetoresistance measured with magnetic field in out-of-plane direction |
| $AMR^{IP}$ | Anisotropic magnetoresistance measured with magnetic field in in-plane direction |
| $\mathbf{B}$ | Magnetic induction |
| $C_1, C_2$ | Constant |
| $\mathrm{d}$ | Derivative |
| $d_\uparrow$ | d band for majority electrons |
| $d_\downarrow$ | d band for minority electrons |
| $e$ | Electron charge |
| $E$ | Electric field |
| $E_a$ | Anisotropy energy |
| $E_{ex}$ | Exchange energy |
| $E_z$ | Zeeman energy |
| $f$ | Frequency |
| $F$ | Faraday constant |
| $F_L$ | Lorentz Force |
| $F_x$ | Force in the direction $x$ |
| $GMR_{OOP}$ | Maximal giant magnetoresistance measured with magnetic field in out-of-plane direction |
| $GMR_{IP}$ | Maximal giant magnetoresistance measured with magnetic field in in-plane direction |
| $\mathbf{H}$ | Magnetic field |
| $H_\parallel$ | Magnetic field applied parallel to the nanowire |
| $H_\perp$ | Magnetic field applied perpendicular to the nanowire |
| $H_a$ | Applied external magnetic field |
| $H_c$ | Coercive Field |
| $H_d$ | Demagnetising field |
| $H_{dip}$ | Dipolar interaction field |
| $H_{eff}$ | Effective anisotropy field |
| $H_{IP}$ | Magnetic field applied in the in-plane direction |
| $H_{IP;\parallel I}$ | Magnetic field applied in the in-plane direction parallel to the global current flow |
| $H_{IP;\perp I}$ | Magnetic field applied in the in-plane direction perpendicular to the global current flow |
| $H_{mc}$ | Magnetocrystalline anisotropy field |
| $H_{ms}$ | Magnetostatic anisotropy field |
| $\hbar$ | Reduced Plank constant |
| $i, j$ | Index |
| $I$ | Current |
| $j$ | Current density |
| $j$ | Current density |
| $J$ | Exchange integral |
| $k_B$ | Boltzmann constant |
| $K_1$ | Magnetocrystalline anisotropy constant |
| $K_u$ | Uniaxial anisotropy constant |
| $l$ | Mean free path |
| $L$ | Length |
| $L_s$ | Spin diffusion length |
| $m$ | Magnetic moment |
| $m$ | Total mass deposited |
| $\mathbf{M}$ | Magnetisation |
| $M_{10\ kOe}$ | Magnetisation for an applied field of 10 kilo Oersted |
| $m^*$ | Electron effective mass |

| | |
|---|---|
| $m_e$ | Electron mass |
| $M^{n+}$ | Metallic ions with $n$ electron missing |
| $M_r$ | Remanence magnetisation |
| $M_s$ | Saturated magnetisation |
| $\mathbf{m}$ | Magnetic moment |
| $n$ | Number of atoms per unit cell |
| $n$ | Electron density |
| $n$ | Total number of moles reduces |
| $N$ | Number of electrons |
| $n_\uparrow$ | Density of majority electrons |
| $n_\downarrow$ | Density of majority electrons |
| $N_A$ | Avogadro's number |
| $n_{Co}$ | Cobalt atomic density |
| $n_{Ni}$ | Nickel atomic density |
| $n_w$ | Weiss coefficient |
| $\mathcal{N}$ | Demagnetising tensor |
| $\mathcal{N}_x$, $\mathcal{N}_y$, $\mathcal{N}_z$ | Demagnetising factors |
| $P$ | Pondering factor function of the membrane porosity |
| $Q$ | Total charge deposited |
| $R$ | Resistance |
| $R_\parallel$ | Resistance state reached when the magnetisation is parallel to the current in the whole sample |
| $R_0$ | Resistance in absence of magnetic field |
| $R_{H=0}$ | Resistance when the magnetic field is turned back to zero |
| $R_{OOP}$ | Resistance when the magnetisation saturated in out-of-plane direction |
| $R_{IP}$ | Resistance when the magnetisation saturated in in-plane direction |
| $R_{max}$ | Maximal resistance state reached during a magnetotransport measurement |
| $R_{sat}$ | Resistance when the magnetisation is saturated in a given direction |
| $RRR$ | Residual resistivity ratio |
| $S$ | Spin number |
| $S$ | Section |
| $t$ | Time |
| $t$ | Thickness |
| $T_C$ | Curie temperature |
| $v$ | Electron velocity |
| $V$ | Tension drop |
| $x$, $y$, $z$ | Directions |
| $x$ | Distance |
| $x_{Ni}$ | Nickel atomic fraction |
| $Z$ | Number of valence electrons |

# Introduction

Today, more and more research is being carried out in the field of Spintronics. This area of physics associates two concepts: the intrinsic spin of the electron – and its associated magnetic moment – is combined with its electric charge. Nowadays, Moore's law arrives at its limits. In industrial electronics, the atomic scale is reached. The reduced size of our devices generates heating problems. A new property of particles needs to be exploited if we want to further optimise our apparatus and reduce their size. Instead of only using the electric charge of a particle, we now also look to exploit its quantum property, namely the spin.

The discovery of giant magnetoresistance (GMR) made this new field of Science more accessible. This quantum mechanical effect is characterised by a large change of resistance induced by the application of a magnetic field. GMR presents a large interest for its application in magnetic field sensors such as data storage in hard disks drives, biosensors, logic-in-memory architectures, etc. The GMR effect is observed in systems made of alternating thin layers of ferromagnetic and non magnetic materials. In this master thesis, the GMR of multilayered crossed nanowire (MCNW) networks is studied, using Nickel-Cobalt alloys as ferromagnetic materials and Copper as non magnetic material. The nanowires (NWs) are grown inside a polycarbonate template using an electrodeposition method. This method presents a simple and accessible way to create the desired networks.

To understand the GMR phenomenon, one must first go back to the origin of ferromagnetism. The 3d metals iron (Fe), nickel (Ni) and cobalt (Co) possess a particular filling of bands, which gives them spontaneous magnetic properties below a certain temperature. When nanostructures are created, the magnetic properties must be well understood inside the bulk material first. Then, these properties can be analysed in a single NW, a parallel NW array, and finally in a MCNW network.

The objective of this master thesis is to estimate the influence of varying Cobalt content in a Nickel-Cobalt alloy on the GMR, and to study the magnetic properties of these alloys in MCNW networks. This master thesis focuses on one part of these alloys, depending on the Nickel-Cobalt ratio of the alloys used. The $Ni_{100}Co_0/Cu$ (i.e. Ni/Cu) to $Ni_{75}Co_{25}/Cu$ MCNW networks are studied by Kyara Hallet in another work; the $Ni_{50}Co_{50}/Cu$ to $Ni_0Co_{100}/Cu$ (i.e. Co/Cu) MCNW networks are studied in this master thesis.

This work is structured in three main sections. First, the state of the art provides the reader with the important concepts, necessary to understand the following chapters of the thesis. Previous results and discoveries in this field of research are also mentioned at the end of this first chapter. Next, the characterisation techniques are described. Here, all the parameters are given on how the samples are prepared and fabricated and how each measurement is elaborated. Finally, the last chapter presents the obtained results: how the magnetic and GMR properties vary when the ferromagnetic layer thickness, the non magnetic layer thickness, the temperature and the porosity are modified. After these three main chapters, the conclusion presents the final results and discusses further perspectives.

# Chapter 1

# State of the art

The systems studied in this thesis are 3D interconnected ferromagnetic nanowire (NW) networks. The state of the art contains three sections. The first section provides general concepts about magnetic, electric and magneto-electric properties of ferromagnetic 3d transition metals, and about nanostructures made of successive layers of ferromagnetic (F) and non-magnetic (NM) layers. These concepts help to understand the process leading to giant magnetoresistance (GMR) in NWs. The second section describes first the fabrication process of the crossed nanowire (CNW) network. Then, the magnetic and magnetotransport properties of a single NW are presented. After that, the evolution of this magnetic and magnetotransport properties are described when passing from a single NW to a parallel array of NW and to finally arrive to a crossed network of NW. Some GMR results obtained in previous work [44] are presented in this last section.

## 1.1 Ferromagnetism in 3d transition metals

The systems studied in this thesis are 3D interconnected ferromagnetic nanowire (NW) networks. This state of the art contains three sections. The first section provides general concepts about magnetic, electric and magneto-electric properties of ferromagnetic 3d transition metals, and about nanostructures made of successive layers of ferromagnetic (F) and non-magnetic (NM) layers. These concepts help to understand the process leading to giant magnetoresistance (GMR) in NWs. The second section first describes the fabrication process of the crossed nanowire (CNW) network. Then, the magnetic and magnetotransport properties of a single NW are presented. After that, the changes on these magnetic and magnetotransport properties when forming a parallel array of NWs and finally a crossed network of NWs, are described. Some GMR results obtained in previous work [44] are presented in this last section..

### 1.1.1 Magnetic Properties

Magnetism is a phenomenon associated with magnetic fields which arise from the motion of electric charges. The *magnetic moment*, which can be measured, describes the object's tendency to align with a magnetic field. It is a vector quantity defined as $\vec{\mu} = I \cdot A \cdot \hat{n}$ with $A$ the area of the loop of an electron rotating around a proton, $I$ the intensity of the electric current associated with the moving electron and $\hat{n}$ the normal unit vector as shown in figure 1.1.

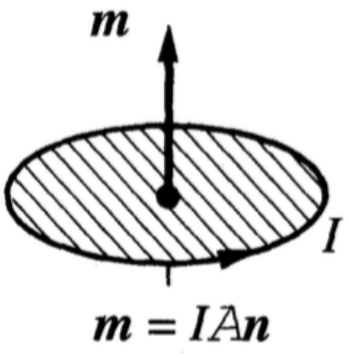


FIGURE 1.1: Illustration of the magnetic moment. The area A and current I are indicated [37].

When defining magnetic properties such as **B**, the magnetic flux density, **H** the magnetic flux strength and **M** the magnetisation, different systems can be used with different units. Table 1.1 gives the units of the 2 existing systems (SI and CGS), and the corresponding conversion factors.

| | SI | CGS | Conversion |
|---|---|---|---|
| **H** | A· m$^{-1}$ | Oe | 1 Oe= $\frac{10^3}{4\pi}$ A· m$^{-1}$ |
| **B** | T | Gs | 1 Gs = $10^{-4}$ T |
| **M** | A· m$^{-1}$ | emu· cm$^{-3}$ | 1 emu· cm$^{-3}$ = $10^3$ A· m$^{-1}$ |

TABLE 1.1: SI and CGS systems. Conversion scheme for H, B and M.

The *magnetisation* of a material is the density of magnetic moment that is induced in a magnetic material when it is placed in a magnetic field:

$$\vec{M} = \frac{1}{V}\sum_i \vec{\mu_i} = \frac{N}{V}\cdot\vec{\mu} \quad [\text{ T }] \tag{1.1}$$

with $V$ the volume of the sample and $N$ the number of atoms in the sample. The magnetisation is related to the the magnetic flux density (**B**), the magnetic flux strength (**H**) by the relation:

$$B = \mu_0(H + M) \quad [\text{ T }]$$

with $\mu_0$, the vacuum permeability.

The *electrical elemental moment*, also called the Bohr magneton, is defined as:

$$\mu_B = \frac{e\hbar}{2m_e} \quad [\text{ J}\cdot\text{T}^{-1}\text{ }]$$

with $e$ the electrical charge, $\hbar$ the Planck constant and $m_e$ the mass of an electron.

The magnetic moment of a free atom has three principal sources: the spin with which electrons are endowed, the orbital angular momentum of electrons about the nucleus and the change in the orbital moment induced by an applied magnetic field. The first two effects produce paramagnetic contributions while the third effect gives a diamagnetic contribution.

The *magnetic susceptibility* is a dimensionless number describing the degree of magnetisation of a material in response to a magnetic field. This notion is linked to the magnetisation by equation (1.2) ([30]):

$$\chi = \frac{M}{H} \quad [\text{ - }]\text{ (CGS)}\,; \quad \chi = \frac{\mu_0 M}{H} \quad [\text{ - }]\text{ (SI)} \tag{1.2}$$

In case of paramagnetic and ferromagnetic effects (Ni, Co), $\chi > 0$ while in the case of diamagnetic effects (Cu), $\chi < 0$. Many types of magnetic moments exist, such as ferrimagnetism, antiferromagnetism, helical and other more complex forms. Table 1.2 gives the order of magnitude of the magnetic susceptibility of the 3 principal magnetic orders.

| Magnetic order | Magnitude of $\chi$ [-] |
|---|---|
| Paramagnetism | $\sim 10^{-3}$ |
| Ferromagnetism | $\sim 10^{3}$ |
| Diamagnetism | $\sim -10^{-5}$ |

TABLE 1.2: Magnitude of $\chi$ for different magnetic orders.

**Pauli susceptibility of the free electron gas**

To introduce ferromagnetism, the reaction of a free electron gas when immersed in a magnetic field is first observed.

The energy of free electrons is defined as: $E = \frac{\hbar^2 k^2}{2m_e}$, with k the wave vector of the electron. Each state occupies a k-space volume $V$ that defines density of states in k-space $\frac{2\pi}{L} = \frac{(2\pi)^3}{V} = D(k)$ which can be translated into energy space $D(E)$.

$$D(E) = \frac{V}{2\pi^2}(\frac{2m}{\hbar^2})^{3/2}\sqrt{E} \quad [\text{cm}^{-3}\cdot\text{eV}^{-1}]$$

The *Fermi-Dirac distribution* gives the probability that an orbital at energy $\epsilon$ will be occupied in an ideal electron gas at thermal equilibrium, where $\mu$ is the chemical potential, equal to the Fermi energy at absolute zero.

$$f(\epsilon) = \frac{1}{e^{(\epsilon-\mu)/k_b T}+1}$$

with $k_B$ the Boltzmann constant. The Fermi surface is the surface of constant energy $\epsilon_f$ in k space. The Fermi surface separates the unfilled orbitals from the filled orbitals, at absolute zero. The electrical properties of the metal are determined by the volume and shape of the Fermi surface, because the current is due to changes in the occupancy of states near the Fermi surface. The number of occupied state in a certain volume is given by:

$$\frac{N}{V} = \int_0^\infty D(E)f(E,T)dE \quad [\text{ cm}^{-3}]$$

Figure 1.2 represents the density of states (DOS) of a two-spin-system as a function of the energy. At $T > 0$, some electrons are thermally excited following the Fermi-Dirac distribution, but the density stays the same for both spin states at zero magnetic field. When a magnetic field is present, the energy of the magnetic moment parallel to H is lowered by $\Delta E$ and the energy of the antiparallel ones is increased by $\Delta E$. This phenomenon leads to spin flip from higher energy states to lower ones with the consequence that both spin states have the same energy threshold $E_F$. The resulting magnetisation is function of the difference between up- and down-spins:

$$M = \frac{N\uparrow - N\downarrow}{V} = 2\cdot\frac{1}{2}D(E_F)\cdot\mu_0\mu_B H \quad [\text{ A}\cdot\text{m}^{-1}]$$

and thus the Pauli susceptibility:

$$\chi_{Pauli} = \frac{M}{H} = \mu_0\mu_B^2 D(E_F) \quad [\text{ - }] \tag{1.3}$$

The Pauli susceptibility approaches $10^{-5}$ for alkali metals. The magnetic susceptibility is considerably higher for most transition metals with unfilled inner electron shells. The high values suggest that the density of orbitals is unusually high for transition metals. But this is not sufficient to explain the presence of a magnetic moment even when no field is applied. There must be some other interactions to explain this high magnetic order.

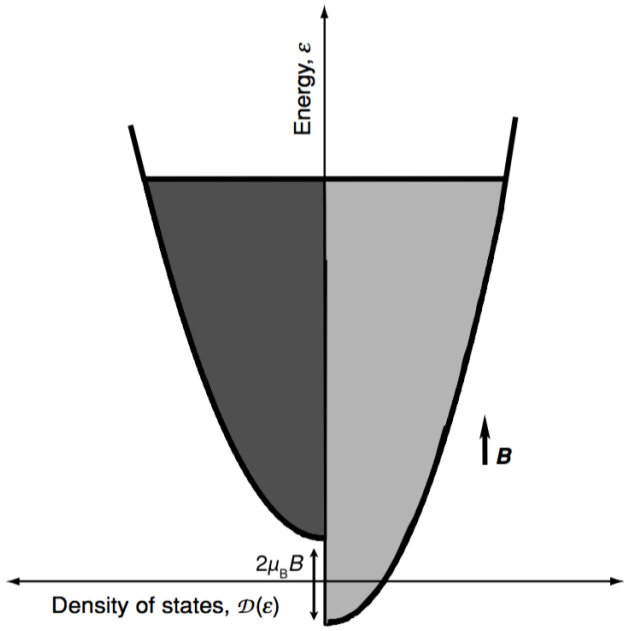


FIGURE 1.2: Spin splitting of the up and down densities of states in a magnetic field. [10]

**Ferromagnetism**

A ferromagnet has a spontaneous magnetic moment; a magnetic moment even in zero applied field. The existence of a spontaneous moment suggests that electron spins and magnetic moments are arranged in a regular manner [30].

Ferromagnets have interacting magnetic moments. Below a certain temperature called the Curie temperature and noted $T_C$, they show a spontaneous magnetic moment. Figure 1.3 illustrates the decrease of the magnetisation as the temperature increases. Above $T_C$, they behave as a paramagnet.

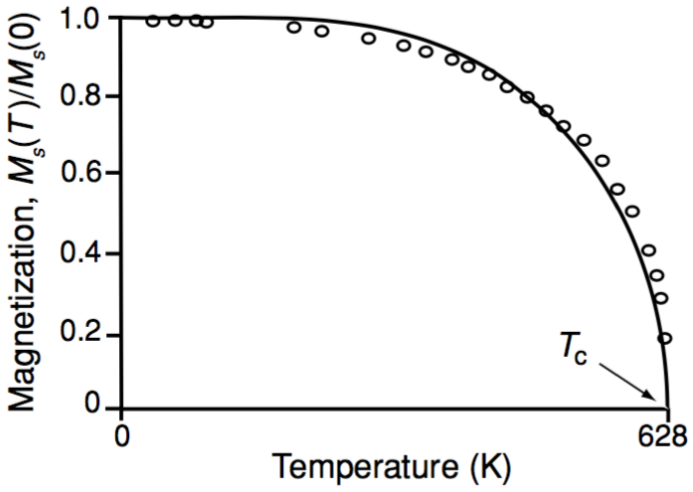


FIGURE 1.3: Temperature dependence of the spontaneous magnetisation of Ni. $T_C$ is indicated at 628K. [10]

Local dipolar fields are not sufficient and can not explain high ordering temperature in compounds such as Fe, Co or Ni. This is why Pierre Weiss postulates the existence of an exchange interaction field (or molecular field), $B_{mol}$, in addition to the external applied magnetic field. This exchange field corresponds to the interaction tending to line up the magnetic moments parallel to each other. Thermal agitation will oppose this effect, giving random orientation. The molecular field is given by:

$$B_{mol} = \lambda \mu_0 M \quad [\ \mathrm{A \cdot m^{-1}}\ ]$$

where $\lambda$ is a mean field parameter due to exchange interaction. By inserting this molecular field in the Brillouin function[1], the Curie temperature, the temperature at which spontaneous magnetisation disappears, can be found.

$$T_C = C\lambda \quad [\ \mathrm{K}\ ]$$

with $C$, the Curie constant. Typical values of the Curie temperature for ferromagnetic transition metals are given in table 1.3. $\mathrm{M}_s$ stands for the magnetisation at saturation.

| | $\mathrm{T}_c$ [K] | $\mu_0 \mathrm{M}_s$ [T] |
|---|---|---|
| $\alpha$Fe | 1033 | 2.20 |
| Ni | 1395 | 1.82 |
| Co | 6274 | 0.64 |

TABLE 1.3: Curie Temperature and saturation magnetisation of bulk Fe, Ni and Co. [27]

To understand the exchange interactions between electrons, the Pauli exclusion principle is used to calculate the energy eigenvalues of the Helium atom based on perturbation theory. This leads to the concept of exchange energy which was extended by Heisenberg to a system of spins to propose a model for the origin of ferromagnetism [5]. Developments of this concept are given in appendix A.2. Heisenberg proposed a scenario where ferromagnetism would come from exchange interaction between electrons. He proposed that the internal magnetic field in ferromagnets, arising from all spins within a domain lining up parallel to each other, could be linked to the presence of exchange coupling between neighboring ionic spins. The Heisenberg exchange term is expressed as [27]:

$$\mathcal{H} = -2J\vec{s_1} \cdot \vec{s_2} \quad [\ \mathrm{J}\ ]$$

with $J$ the exchange integral, $s_1$ and $s_2$ spin operators. The exchange energy term is truly quantum-mechanical in origin. It can be considered as an additional force (since it is an energy $U$ which varies with the distance $L$ between the spins $F = \frac{dU}{dL}$) to the Coulomb force (positive repulsive force). The "exchange force" is positive for antiparallel spin configuration (repulsion) and negative for parallel spin configuration (attraction). For multiple particles the interpretation is more complicated. For a given $J_{ij}$, if the lowest state of the Hamiltonian corresponds to all spins being aligned, then this will account for the onset of ferromagnetism, since the lowest state corresponds to the ground state.

When trying to understand the phenomenon of ferromagnetism, it is crucial to understand the band structure of ferromagnets. Figure 1.4 shows the filling of the first series of transition metals when going from Scandium to Zinc. For this series of metals, the 4s and 3d bands overlap. The 4s wave functions are broadened wave functions while the 3d's are localized. Fe, Co and Ni all present narrow bands and a large density of states at the Fermi level. This leads to a large Pauli susceptibility. Narrower bands tend to have higher susceptibility, because the density of states at $\epsilon_F$ scales as the inverse of the bandwidth. The exchange interactions lead to an instability of the d-band below $T_C$. The $\mathrm{d}_\uparrow$ and $\mathrm{d}_\downarrow$ are spontaneously out of equilibrium; these phenomena give

[1] Function that describes the dependency of the magnetisation on the external applied magnetic field and the total angular momentum of the microscopic magnetic moments of the material. The function is given in appendix A.1

magnetisation to the system. The metal becomes spontaneously ferromagnetic. The condition to fulfill to get a ferromagnet is known as the Stoner criterion.

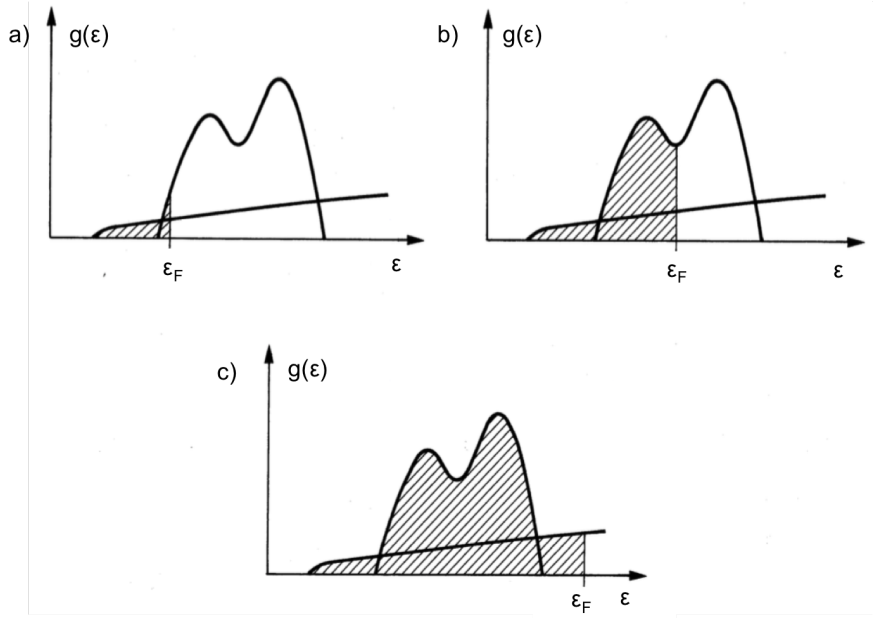


FIGURE 1.4: Filling of the d-band of the first series of transition metals starting at Scandium (a), then Nickel (b) and finally Zinc (c). [37]

**Stoner Criterion** Ferromagnetic exchange in metals does not always lead to spontaneous ferromagnetic order: the Pauli susceptibility must exceed a certain threshold. There must be an exceptionally large density of states at the Fermi level. Figure 1.5 illustrates the filling of the band of the transition metals Fe, Co and Ni. The majority spins are those whose spin polarisation is aligned parallel to the internal magnetic field of the ferromagnet.

The derivation of the Stoner criterion can be found by considering the different changes in energies when the band asymmetry appears [27]. A transfer of electrons from the $\downarrow$ band to the $\uparrow$ band would require an increase of the kinetic energy by an amount $\Delta E_{kin}$. When these electrons are transferred from one subband into unoccupied states of the other subband in order to keep spins distant according to the Pauli principle, the potential energy is decreased by an amount $\Delta E_{pot}$. Indeed, when spins are parallel, the Coulomb energy is reduced. The two $\Delta E$ can be expressed as:

- An increase of kinetic energy: $\Delta E_{kin} = \Delta N \cdot \Delta E = \frac{1}{2} D(E_F) \cdot (\Delta E)^2$
- A decrease of potential energy: $\Delta E_{pot} = -\int_0^{\lambda M} M dH_{eff} = -\frac{1}{2}\mu_0 \lambda M^2$

with $H_{eff}$=$H + \lambda M$. From the definition of the magnetisation given in equation (1.1), one can calculate the magnetisation by subtracting the numbers of up and down magnetic dipoles, $M = \mu_B(N\uparrow - N\downarrow) = \mu_N \cdot D(E_F)\Delta E$. The potential energy resulting from the band splitting can then be expressed as:

$$\Delta E_{pot} = -\frac{1}{2}\mu_0 \lambda \mu_B^2 D^2(E_F)(\Delta E)^2 \quad [\,\mathrm{J}\,]$$

Finally, the total change in energy:

$$\Delta E_{tot} = \Delta E_{pot} + \Delta E_{kin} = \frac{1}{2} D(E_F)(\Delta E)^2 \cdot [1 - \mu_0 \lambda \mu_B^2 \cdot D(E_F)] \quad [\,\mathrm{J}\,]$$

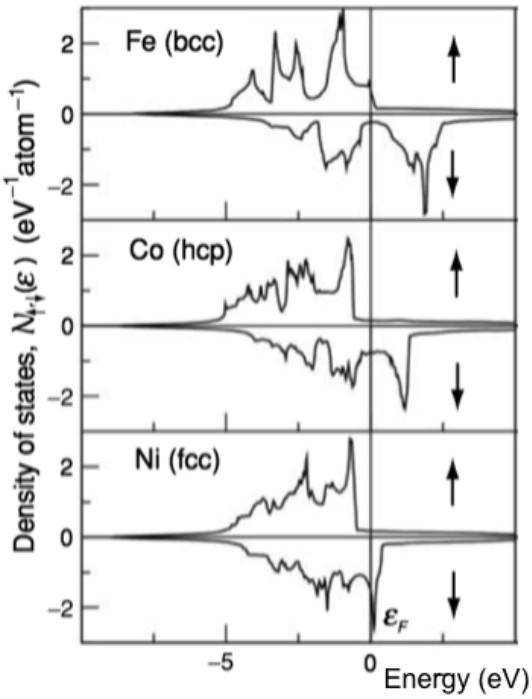


FIGURE 1.5: Density of state as a function of energy for Fe, Co and Ni in the ferromagnetic state. [10]

If the decrease in potential energy is large enough to compensate the energy gain of the system, the Stoner Criterion is satisfied, see equation (1.4). This leads to a spontaneously magnetised ground state. [35]

$$U \cdot D(E_F) \geq 1 \tag{1.4}$$

with the Coulomb repulsion $U = \mu_0 \lambda \mu_B^2$. This means that in order to fulfill the Stoner Criterion, one needs a large DOS at the Fermi level ($D(E_F)$) and a large mean field parameter ($\lambda$). From the bandscheme (figure 1.5 and figure 1.4), it can be seen that Fe, Co and Ni present a large DOS at the Fermi level, and from the high $T_C$ (table 1.3) the mean field parameter is also large for these 3 metals. By looking at the value of $U \cdot D(E_F)$ of 3d metals (table 1.4), one can see that only three metals fulfill the Stoner criterion: Fe, Co and Ni. As a consequence, these materials present ferromagnetic properties.

| 3d TM | $U \cdot D(E_F)$ [-] |
|---|---|
| Cr | 0.27 |
| Mn | 0.63 |
| **Fe** | **1.43** |
| **Co** | **1.7** |
| **Ni** | **2.04** |
| Cu | 0.11 |

TABLE 1.4: Stoner criterion for different 3d transition metals (TM). [27]

Some of their alloys also present ferromagnetic properties. The Slater Pauling curve in figure 1.6 illustrates the values of the saturation magnetisation for alloys of 3d metals. The average atomic moment saturation moment can be derived from this curve. The slope of the curve is linked to

the number of valence electron that can contribute to the atomic moment. The atomic saturation magnetisations of $\alpha$Fe, Co and Ni are 2.2 $\mu_B$, 1.7$\mu_B$ and 0.6 $\mu_B$ respectively.

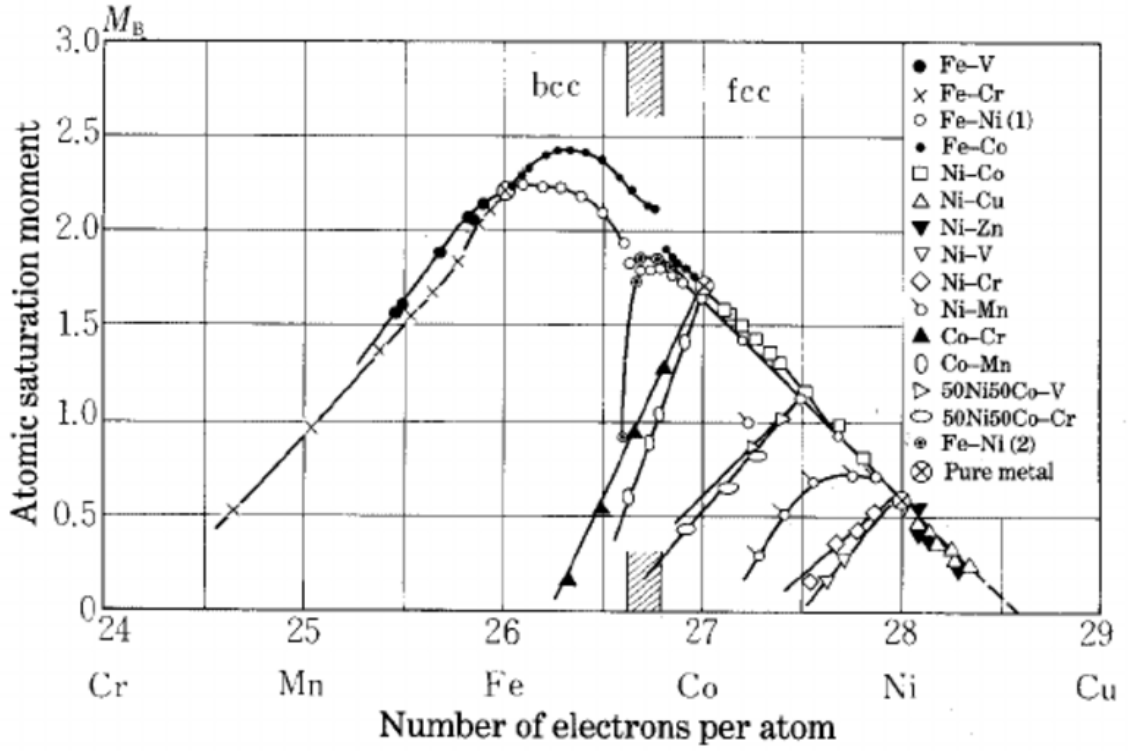


FIGURE 1.6: Slater Pauling curve. Atomic saturation moment versus the number of valence electrons per atom. [43]

**Characteristics of ferromagnetic materials: hysteresis and anisotropy**

As described before, Fe, Ni and Co all show a spontaneous magnetic moment. However, Fe bulk is not a permanent magnet. This can be explained by the presence of domains. The origin of domains can be explained by the following: when only one domain is present (figure 1.7.A), the magnetic field resulting from the magnetisation at saturation is mostly out of the material. This configuration requires a large magnetic energy. The formation of domains minimises this spatial extension of the magnetic field out of the material, so that there is no exterior magnetic field (figure 1.7.C). Moreover, domain formation allows for interaction between spins, more precisely, dipolar coupling.

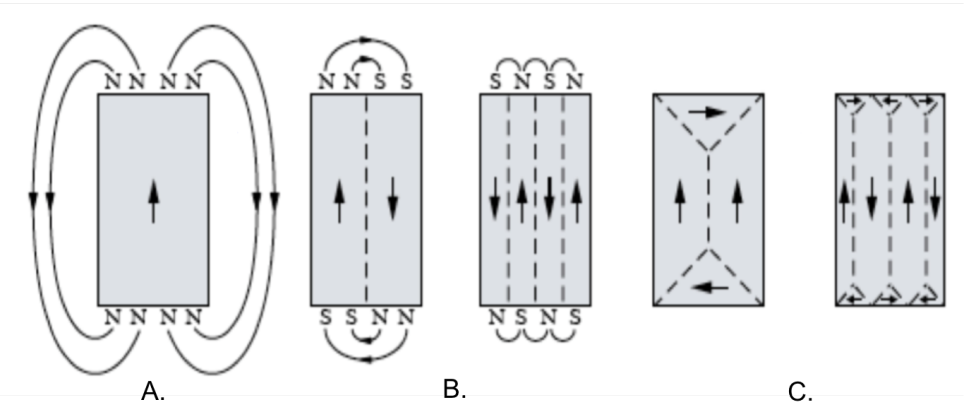


FIGURE 1.7: Origin of domains. (A) One single domain with large magnetic field outside the material. (B) Domain formation with a smaller magnetic field outside the material. (C) Smaller domains with no magnetic field outside the material. [37]

There are two types of interaction between spins:

- exchange interactions
- dipolar interactions

The exchange interactions have been explained before. Dipolar interactions are much weaker than the exchange interaction, typically a thousand times weaker between neighboring spins in a metal. However, the exchange interaction is short-range since it depends on the overall wave functions between the interacting electrons. Its strength decreases exponentially with increasing separation between the interacting electrons. In contrast, the dipolar interaction is long range and decreases with the inverse cube of the separation. As a result, the dipolar interaction becomes quite important if many spins are involved and may overwhelm the exchange interaction. This is the cause for the formation of domains in ferromagnets.

Dipolar coupling can be explained as follows: each spin generates a magnetic field that is oriented parallel to the nuclear spin vector. Two spin that are close to each other in space experience each other's magnetic field. This leads to a slightly different effective magnetic field that depends on the orientation of both magnetic dipoles.

Each nuclear spin possesses a magnetic moment. These magnetic moments interact through space; this is a dipole-dipole – or dipolar – coupling. Classically, the energy between two punctual magnetic dipoles $\mu_1$ and $\mu_2$ separated by a distance $r$ is [14]:

$$U = \left\{ \frac{\mu_1 \cdot \mu_2}{r^3} - 3\frac{(\mu_1 \cdot r)(\mu_2 \cdot r)}{r^5} \right\} \frac{\mu_0}{4\pi} \quad [\,\mathrm{J}\,]$$

with $r$ the vector between point-magnetic dipoles and $\hat{\mu}$ the magnetic moment operator.

The dipolar Hamiltonian can be expressed as $\hat{H_{dd}} = -2\hat{I} \cdot D \cdot \hat{S}$. The dipolar coupling tensor $D$ describes how the field due to spin $S$ varies with the orientation of the $I - S$ internuclear vector in the applied field. The spin angular momenta of $I$ and $S$ determine the local magnetic field they each give rise to. These angular momenta are quantized, with $B_0$ defining the quantization axis for both. Thus the local field that each spin gives rise to depends on the direction of $B_0$. The strength of field at spin I due to spin S hence depends on the relative orientation of the I-S vector in the applied field, $B_0$, as shown in figure 1.8.

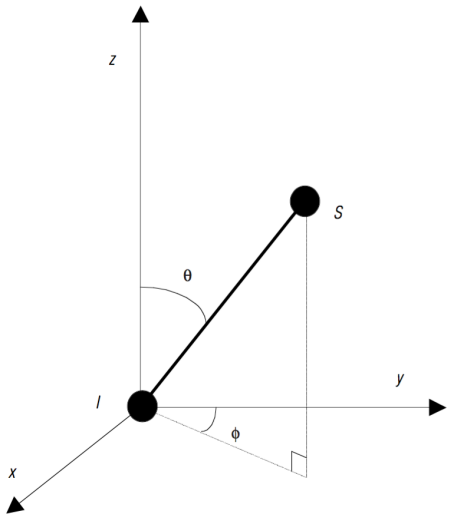


FIGURE 1.8: Specification of the orientation of the I-S internuclear vector with respect to the $B_0$ field which is oriented along the z-axis. [14]

Neighbouring domains typically have oppositely directed magnetisations, so that electrons at both sides of domain boundaries have anti-parallel spins. The exchange energy is non-zero and negative only between parallel spins. Therefore, the spins near the domain boundaries have their total energy raised by the vanishing of the exchange interaction. Spins far from the domain walls are not affected by this effect since the exchange energy is short range. Therefore, only a small price in exchange energy is paid to form domains. On the other hand, because of its long range nature, the dipolar energy of every spin drops when domains are formed. Therefore, provided the domains are not too small, domain formation is energetically encouraged. Every spin can lower its (tiny) dipolar energy by forming domains, while only few spins have their (large) exchange energy increased [5].

**Hysteresis** The magnetic properties will be influenced by several factors such as:whether a material is composed of a single domain or of multiple domains or by the way the magnetic moment of the domain(s) will follow the direction of the applied field. These magnetic characteristics can be observed thanks to a hysteresis loop. The presence of anisotropy (directional dependence of a material's magnetic properties) can then be derived from this loop. Within each domain, the magnetic moments of all atoms (those that have any residual magnetic moment) point in the same direction, so that each domain has complete spontaneous magnetic ordering and therefore an internal magnetic field. In the "unmagnetised" state, the magnetic moments of different domains point in different directions, so that they vectorially add up to zero and there is no net magnetisation of the ferromagnet as a whole. When a sufficiently strong external magnetic field is applied to magnetise the ferromagnet, the magnetic moment of every domain turns in the direction of the field, so that ultimately all domains are magnetised parallel to the field, as illustrated in figure 1.9. This is the saturated "magnetised" state.

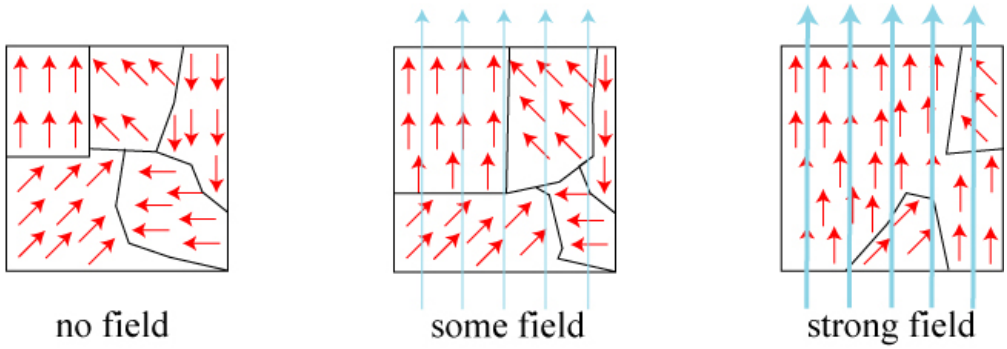


FIGURE 1.9: Different steps when applying an external field to a ferromagnet. When there is no applied field, one can see all the domains. Then the domains disappear, giving rise to one single domain with all spins pointing in the same direction. [5]

When an external magnetic field is applied to a ferromagnet, the magnetisation tends to align itself on the external magnetic field, because this decreases its energy. This effect is called the magnetostatic Zeeman energy and is minimum when the magnetisation of the system is parallel to the applied magnetic field:

$$E_Z = \mu_0 \vec{M} \cdot \vec{H} = -\mu_0 M H \cos\phi \quad [\,\mathrm{J \cdot m^{-3}}\,]$$

with $\phi$ the angle between the applied field $H$ and the magnetisation $M$. When a magnetising field is applied, domains that are already aligned along the field grow at the expense of unaligned domains, then domains align with the direction of the field until reaching the saturation magnetisation $M_s$, as indicated at the end of the red arrow in figure 1.10. When the magnetising field is removed, the domains do not necessarily return to their original alignments because crystalline defects may prevent domain wall motion, leading to a remanent magnetisation $M_R$, which is indicated at the end of the blue arrow in figure 1.10. Then, it becomes necessary to apply a strong field in the opposite direction to overcome this pinning and restore the original unmagnetised state. This phenomenon is known as **hysteresis** and the magnetic field required to reduce the magnetic moment to zero is known as the coercive field $H_c$, visible in figure 1.10 at the end of the green arrow. The slope of the hysteresis curve is called susceptibility $\chi$ as expressed in equation (1.2).

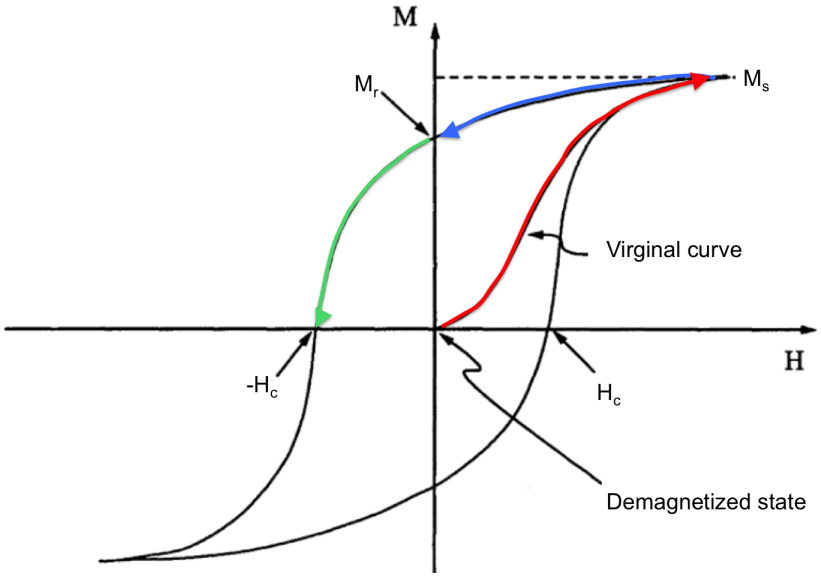


FIGURE 1.10: Hysteresis loop at $T < T_C$. The remanent magnetisation, saturation magnetisation and coercive field are indicated. [35]

There exist soft and hard ferromagnets which are characterised by different shape of hysteresis loop, as shown in figure 1.11. Soft ferromagnets can be easily demagnetised and present a low coercive field. They are used for applications which need a small variation of external magnetic field and fast response, such as a compass. The dissipated energy is lost in heat. On the opposite, hard ferromagnets are much more difficult to magnetise and demagnetise. They are characterised by large hysteresis loops, with high coercive fields and remanent magnetisations. They are used as permanent magnets. For example, $\beta-$Fe and Ni are soft ferromagnets while $\gamma$-Co is a hard ferromagnet. CoNi alloy NWs are magnetic materials that can exhibit either soft or hard ferromagnetic behaviour depending on the Co content in the alloy.

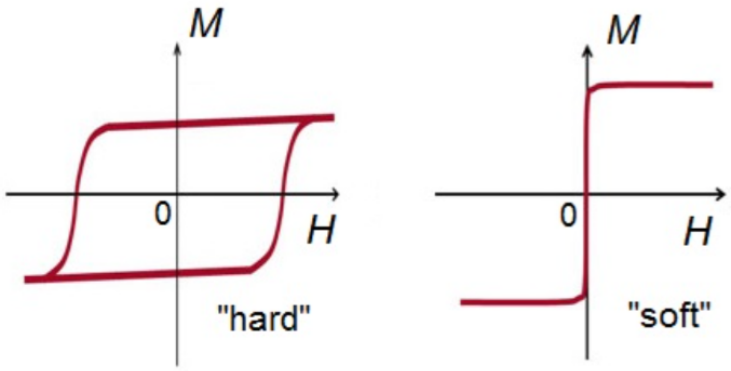


FIGURE 1.11: Left: hard ferromagnet. Right: soft ferromagnet. [27]

The shape of the hysteresis loop of hard ferromagnet find its origin in strong anisotropy. The anisotropy tends to align the magnetic moments along a specific direction which can depend on the shape of the system or on the crystalline structure. The anisotropy is defined as:

$$E_a = K_a \sin^2\theta \quad [\,\mathrm{J}\cdot\mathrm{m}^{-3}\,]$$

with $\theta$ the angle between the direction of M and the anisotropy axis and $K_a$ an anisotropy constant, as shown in figure 1.12. The anisotropy depends on temperature, and must tend to zero at $T_C$ if there is no applied field.

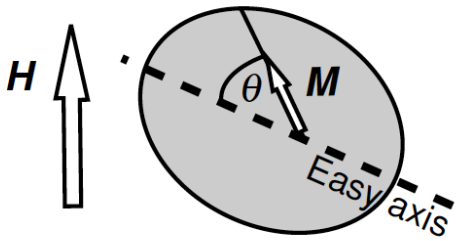


FIGURE 1.12: Magnetisation of a material presenting anisotropy [10].

Three main sources of anisotropy exist. They are related to sample shape, crystal structure and atomic or micro-scale texture.

**Shape anisotropy** The geometry of the sample can create an anisotropy. The fields in cylindrical and rectangular magnetised bodies are not uniform, even if the magnetisation is assumed to be

uniform. In the case of a large sphere (containing many atoms) the shape of the sample does not introduce additional anisotropy. In small clusters, the magnetisation reversal is complicated by the reduction of symmetry and the increased relative contribution of surface atoms. If the sample is not spherical, the magnetostatic energy of the system depends on the orientation of magnetic moments within the sample. The internal magnetic field of the material is given by [10]:

$$H_i = H_a + H_d \quad [\,\mathrm{A \cdot m^{-1}}\,]$$

where $H_a$ is the applied magnetic field and $H_d$ is the demagnetising field that is expressed as:

$$H_d = \mathcal{N}_{ij} M_j \quad [\,\mathrm{A \cdot m^{-1}}\,]$$

where $\mathcal{N}_{ij}$ is the demagnetising tensor and the indices $ij$ stand for the 3 directions x, y or z. The demagnetising factors $(\mathcal{N}_x, \mathcal{N}_y, \mathcal{N}_z)$ are the components of the diagonal of the matrix. The sum of these factors is one. Demagnetising factors of some common shapes are given in table 1.5.

| Shape | Magnetising direction | $\mathcal{N}$ |
|---|---|---|
| Long Needle | Parallel to axis | 0 |
| | Perpendicular to axis | 1/2 |
| Sphere | Any direction | 1/3 |
| Thin film | Parallel to plane | 0 |
| | Perpendicular to plane | 1 |

TABLE 1.5: Demagnetising factor for simple shapes. Data from [10]

If only shape anisotropy is present, the anisotropy constant is expressed as:

$$K_{sh} = \frac{1}{4}\mu_0 M_s^2 (1 - 3\mathcal{N}) \quad [\,\mathrm{J \cdot m^{-3}}\,]$$

It is possible to check that the anisotropy constant is effectively zero for a sphere ($\mathcal{N} = 1/3$) while for NWs in the direction parallel to the nanowire axis one obtains $K_{sh} = \frac{1}{4}\mu_0 M_s^2$ and in the direction perpendicular to the axis $K_{sh} = -\frac{1}{8}\mu_0 M_s^2$. Due to the strong demagnetising factor $(1/2)$ in the direction perpendicular to the wire, this direction is called the hard axis while the direction along the NW axis, with $\mathcal{N} = 0$ is called the easy axis. These values of $\mathcal{N}$ are values in case of an infinite nanowire. The $M_s$ of Co and Ni are 1400 emu$\cdot$ cm$^{-3}$ and 485 emu$\cdot$ cm$^{-3}$ respectively; the $M_s$ of their alloys are located in between these boundaries, and can be found via the Slater Pauling curve given in figure 1.6. The resulting shape anisotropy constants are 616 kJ$\cdot$ m$^{-3}$ for the Co and 75 kJ$\cdot$ m$^{-3}$ for the Ni, in the direction parallel to the wire axis.

Shape anisotropy is only fully effective in samples which are so small that they do not break up into domains. In a multidomain state, each domain creates its own demagnetising field, and is subject to the stray field of the other domains [10].

**Crystal anisotropy** This type of anisotropy arises due to the crystallinity and crystal phase structure of the material. There are two distinct sources of magnetocrystalline anisotropy. [10]

- single-ion contribution
- two-ion contribution

The first contribution is due to electrostatic interaction of the orbitals containing the magnetic electrons with the potential created at the atomic site by the rest of the crystal. The second contribution reflects the anisotropy of the dipole-dipole interaction or can come from anisotropic exchange.

Depending on the direction of the applied field, and corrected for the demagnetising field, the magnetisation curves of single crystals of Fe, Ni and Co are different, as shown in figure 1.13. For iron, the cube edges $< 100 >$ are easy directions and the cube diagonals $< 111 >$ are hard directions while for Cobalt $< 100 >$ edges are hard direction.

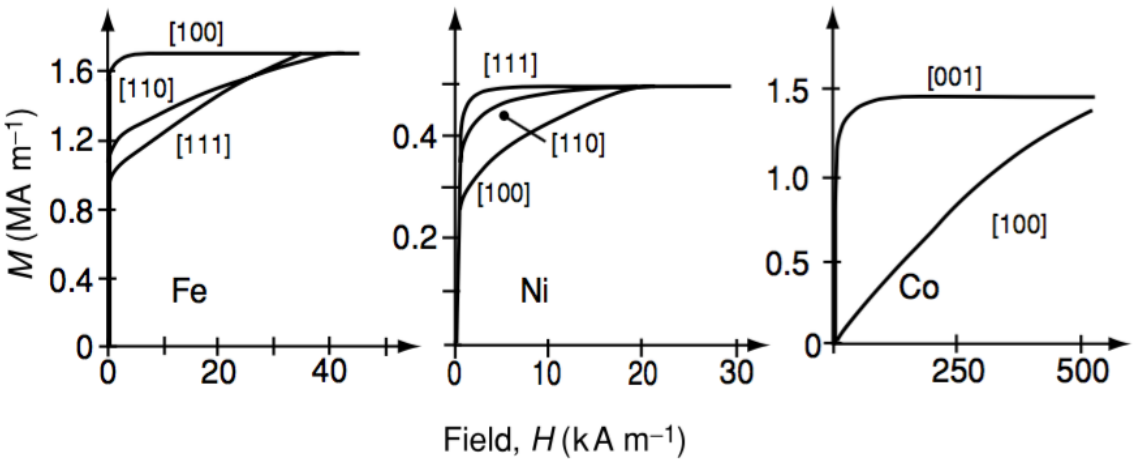


FIGURE 1.13: Magnetisation of single crystals of iron, cobalt and nickel. [10]

Table 1.6 compares the shape and crystal anisotropies for thin films and NWs made of bcc-Fe, fcc-Ni and hcp-Co. One can notice that for Fe and Ni, the shape anisotropy is much larger than the crystal anisotropy. The magnetisation is then in the direction of the thin layer (or of the nanowire axis). In the case of Co, the situation is different, the two anisotropies have the same scale and so compete each other.

| Type of anisotropy [ J · m$^{-3}$ ] | bcc-Fe | fcc-Ni | hcp-Co |
|---|---|---|---|
| Crystal | $5 \cdot 10^4$ | $5 \cdot 10^3$ | $5 \cdot 10^5$ |
| Shape (film) | $\sim 10^6$ | $\sim 10^5$ | $\sim 10^6$ |
| Shape ($\infty$ nanowire) | $9 \cdot 10^5$ | - | $6 \cdot 10^5$ |

TABLE 1.6: Comparison between shape and crystal anisotropy for a film of FM material. [37]

**Surface anisotropy** In the case of surface anisotropy, the magnetisation at a surface/interface is often perpendicular to the interface, which is the exact opposite to shape anisotropy. Due to the presence of an interface, the orbital motion of electrons is affected by the introduced symmetry breaking. Due to broken symmetry at interfaces, the anisotropy energy contains terms with lower order in the direction cosines than in the infinite crystal [10]. Reorientation phase transition may be caused by:

- temperature changes;
- change of the thickness of the magnetic layer;
- change of the thickness of the non-magnetic layer.

In the case of some monodomain samples, a hysteresis loop can also be observed. The origin of this behaviour is the competition between anisotropy and Zeeman energy. Both tends to align their magnetic moment with a different direction as shown on figure 1.14. The total energy is then the

sum of the anisotropy energy $E_A$ and the Zeeman energy $E_Z$:

$$E = E_A + E_Z = K\sin^2\theta - HM_s\cos(\theta - \phi) \quad [\,\mathrm{J \cdot m^{-3}}\,]$$

with $\theta$ the angle between the direction of M and the anisotropy axis, $\phi$ the angle between the anisotropy axis and the applied field and $K$ an anisotropy constant. The moment will select a direction such that the total energy $E_A + E_Z$ is minimised. The orientation of the magnetic moment might occur smoothly (rotation) or suddenly (switching). Depending on the way the magnetic moment will reorient, the hysteresis loop will be different. A strong squareness will be observed for a sudden switch.

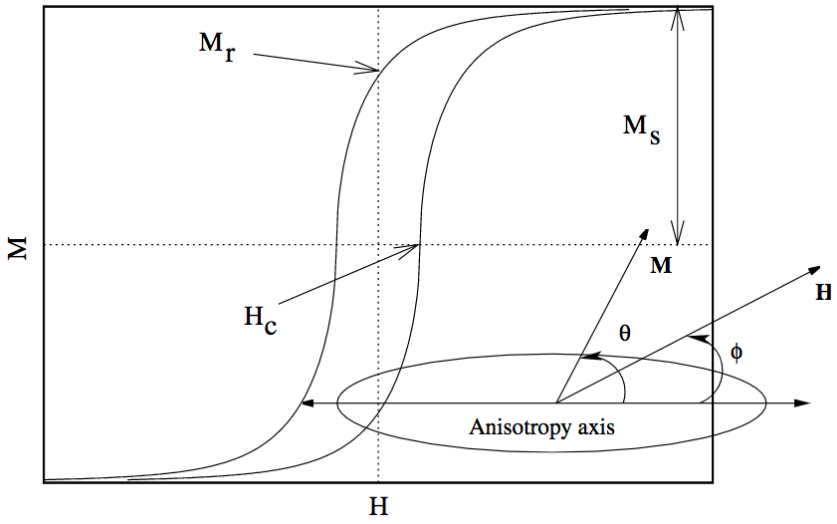


FIGURE 1.14: Single domain hysteresis loop obtained for an arbitrary angle $\phi$ between the applied magnetic field and the anisotropy axis. An ellipsoidal grain is illustrated with a horizontal anisotropy axis. $\theta$ it the angle between the anisotropy axis and the magnetisation. [45]

### 1.1.2 Electric and magneto-electric properties

In this section, some reminders about electric properties of materials are first given. Then, the change of electric properties and the new effects arising when a magnetic field is applied on a material, are explained.

#### Electric properties

In the absence of collisions, the Fermi sphere moves in **k** space at a uniform rate by a constant applied electric field (see figure 1.15). Because of collisions of electrons with impurities, lattice imperfections, and phonons, the displaced sphere may be maintained in a steady state in an electric field. If the collision time is $\tau$, the displacement of the Fermi sphere in the steady state is given by $\delta k = -eEt/\hbar$ with $t = \tau$. The increment velocity is [30]:

$$v = \frac{\hbar\delta k}{m} = \frac{-eE}{m} \quad [\,\mathrm{m \cdot s^{-1}}\,]$$

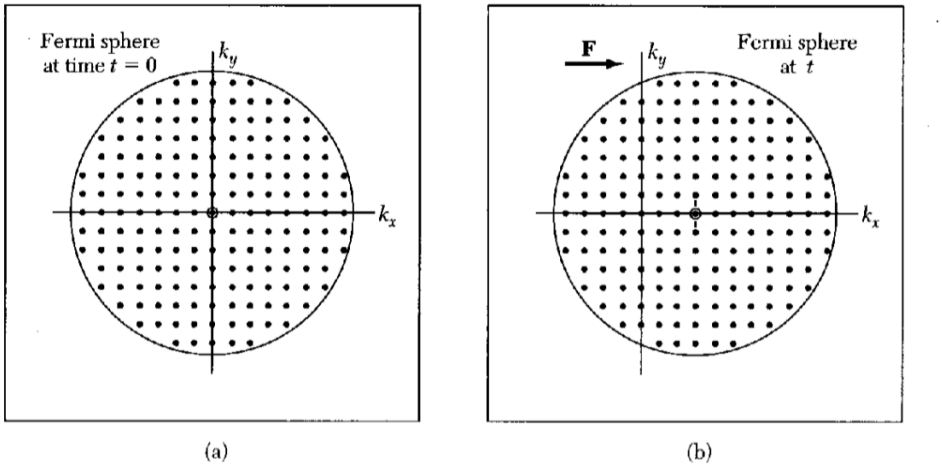


FIGURE 1.15: (a) The Fermi sphere encloses the occupied electron orbitals in **k** space in the ground state of the electron gas. (b) Under the influence of a constant force **F** acting on a time interval $t$, every orbital has its $k$ vector increased. The whole sphere is displaced by $\delta k$ resulting in an increase of the energy of the system. [30]

The electric current density is given by Ohm's law:

$$j = nqv = \frac{nq^2\tau}{m_e} \cdot E \quad [\ \mathrm{A{\cdot}m^{-2}}\ ]$$

where $E$ is a constant electric field and $n$ is the number of electrons of charge $q = -e$ per unit volume.

The electrical conductivity $\sigma$ is defined by $j = \sigma E$. The following law can thus be deduced:

$$\sigma = \frac{ne^2\tau}{m_e} [\ (\Omega{\cdot}\ \mathrm{m})^{-1}\ ]$$

The electrical resistivity is defined as the reciprocal of the conductivity so that $\rho = \frac{m}{ne^2\tau}$. Values of electrical conductivity and resistivity of pure bulk metals used in these work are given in table 1.7.

| | Co | Ni | Cu |
|---|---|---|---|
| Resistivity $[10^{-6}\ \Omega cm]$ | 5,8 | 7 | 1,7 |

TABLE 1.7: Electrical conductivity and resistivity of some metals at $295K$. [30]

The electrical current in ferromagnets is carried by $4s$ electrons, which are more mobile. The unpaired electrons ($3d$) are assumed to be localized on the lattice points. The resistivity of a ferromagnetic metal is given by [26]:

$$\rho = \rho_r + \rho_L + \rho_M \quad [\ \Omega{\cdot}\ \mathrm{m}\ ]$$

where $\rho_r$ is the residual resistivity, $\rho_L$ is the resistivity caused by electron-phonon interaction (lattice), and $\rho_M$ results from electron-spin scattering. Matthiessen's rule is based on the empirical observation that $\rho_r$ is independent of temperature and, when the concentration of defects is small, $\rho_L$ is approximately independent of the number of defects.

The resistivity can vary with the temperature. The residual resistivity ratio (RRR) is defined

as the ratio of resistance at 293K to the resistance at low temperature, ideally 0K.

$$RRR = \frac{\rho_{300K}}{\rho_{0K}} \quad [-]$$

At low temperature ($T \leq 15$ K), the spin-disorder in spin orientation gives rise to the scattering of conduction electrons through the $s-d$ interaction and accordingly contributes to the anomalous part of the resistivity described following law: $\rho_M = BT^2$, where $B$ is a constant [29]. Above 15K, $\rho_M$ has a complicated temperature dependence. For $15K < T < 100K$, the temperature dependence arises mainly from the lattice contribution $\rho_L$, when compared to $\rho_M$. However at high temperatures ($T > 150K$), $\rho_M$ becomes significant again.

**Magnetoelectric effects**

Magnetoelectric effects are exploited in the field of $Spintronics$, which deals with using the spin degree of freedom of a charge carrier to store, encode, access, process and/or transmit information. Lots of research was made investigating how spin-polarised electric currents can be injected into ferromagnetic/paramagnetic multilayers. This finally led to the discovery of giant magnetoresistances (see next subsection). In this part, the concept of spin polarised current is first described, followed by the concept of magnetoresistance.

**Spin polarised current** Due to exchange splitting directly at the Fermi edge in 3d ferromagnetic transition metals, there are more spins in one direction (majority spins) in the d-band available for scattering than in the other direction (minority spins). This leads to Mott's two-fluid Model where the $s-d$ scattering is:

- The prominent scattering mechanism ($\rho_{s-d} >> \rho_{s-s}$)
- Spin conserving (there is no spin-flip during the scattering process)

Spin-up and spin-down s-electrons will face different $s-d$ scattering probabilities due to the imbalance of the d-majority and d-minority spins, as was shown on figure 1.5. Indeed, due to the band-splitting, the spin-down electrons have more empty states to scatter to than the spin-up electrons. Therefore the spin-up and spin-down electrons propagate with different scattering times $\tau_\uparrow$ and $\tau_\downarrow$. The conductivities in the two directions can be defined as:

$$\sigma_\uparrow = \frac{n_\uparrow e^2 \tau_\uparrow}{m_e} \quad ; \quad \sigma_\downarrow = \frac{n_\downarrow e^2 \tau_\downarrow}{m_e} \quad [\ (\Omega \cdot \mathrm{m})^{-1}\ ] \tag{1.5}$$

The current can be represented as two individual and non interacting currents, with their own conductivities and resistivities as illustrated in figure 1.16.

The total current is $j = j_\uparrow + j_\downarrow$. The injection efficiency can then be defined as [21]:

$$\Gamma = \frac{j_\uparrow - j_\downarrow}{j_\uparrow + j_\downarrow} \quad [\ -\ ]$$

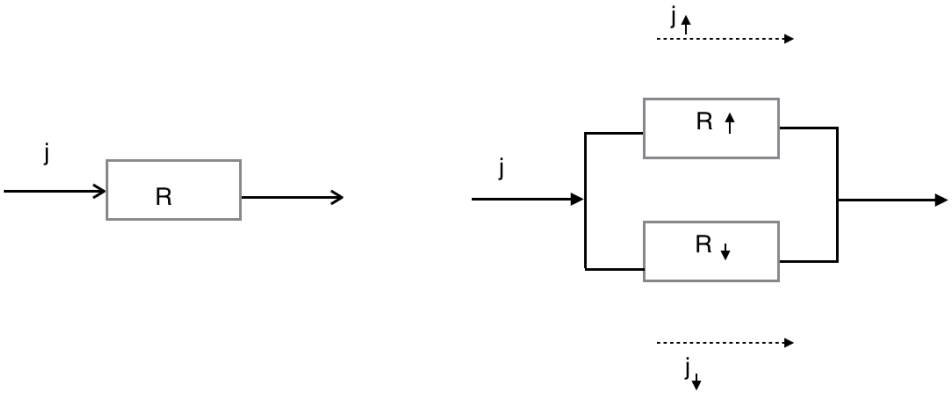


FIGURE 1.16: Illustration of current represented as two individual and non interacting currents.

All spintronic effects in classical ferromagnetic metals are results of the polarisation of currents due to spin-dependent scattering (giant magnetoresistance, GMR) or of strongly different DOS at the Fermi edge (tunnelling magnetoresistance, TMR).

When a sample is placed in a magnetic field, its electrical transport properties are modified, giving rise to magnetoresistance properties (MR). Three intrinsic magnetoresistive effects are described: negative, positive, and anisotropic magnetoresistance.

**Negative Magnetoresistance** In ferromagnetic materials below the Curie Temperature, the resistance can be smaller than expected when compared to non-magnetic materials because of the exchange splitting of the d-band. Figure 1.17 shows that above $T_C$, both types of metals show the same behaviour. Below $T_C$, Ni shows a reduced resistance. The number of "scattering partners" in the ordered configuration decreases and the result is a reduced resistivity [21].

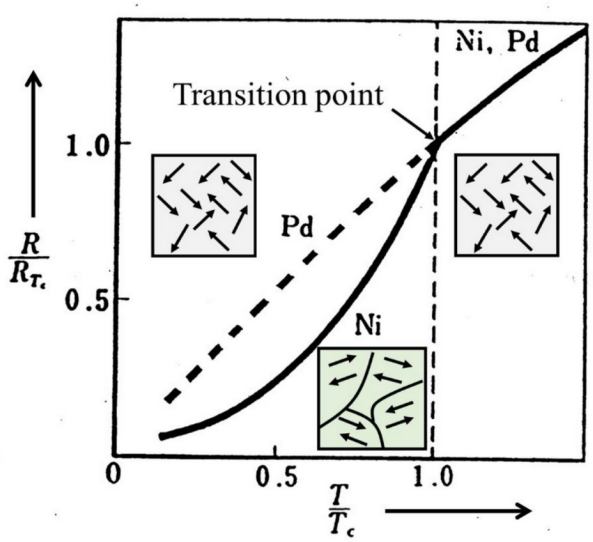


FIGURE 1.17: Normalized resistance of a ferromagnetic material (Ni) and a non-ferromagnetic material (Pd) versus temperature. [41]

**Positive Magnetoresistance** This effect can be explained when looking at the motion of the Fermi sphere in a uniform magnetic field. A Lorentz force appears:

$$F = -e(v \times B) \quad [\,\mathrm{N}\,]$$

This force pushes the electrons towards one or the other edges of the wire depending on the direction of the velocity. Due to the Lorentz force, electrons' mean free path will decrease because of their now more circular trajectories. As a consequence, the probability of scattering will increase and will result in larger resistance when a magnetic field is applied. Magnetoresistance is defined as:

$$MR = \frac{R(0) - R(B)}{R(0)} \cdot 100 \quad [\,\%\,]$$

where $R(B)$ is the resistance of the sample when magnetic field $B$ is applied, while $R(0)$ is the resistance of the sample without magnetic field applied.

**Anisotropic Magnetoresistance (AMR)** AMR is the change of electrical resistance due to the variation of the magnetisation vector's projection on the electrical current direction. This effect arises whenever the magnetisations of the ferromagnets are not collinear with the direction of the current flow. The reason for this phenomenon is spin-orbit coupling (SOC). This phenomenon causes an aspherical charge distribution within the ferromagnetic layer as illustrated in figure 1.18.

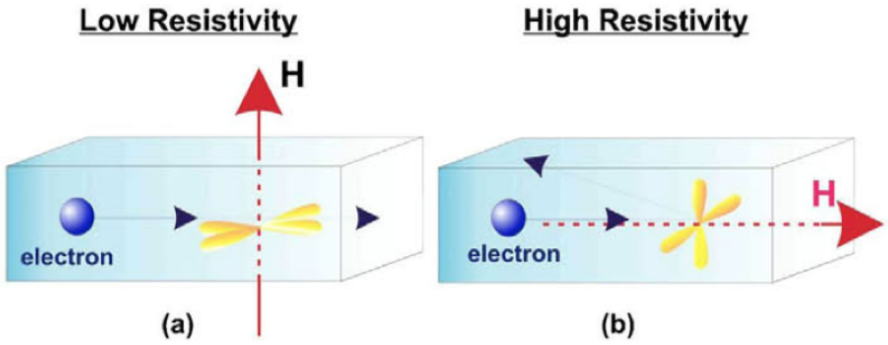


FIGURE 1.18: Spin-orbit coupling causing AMR effect. The scattering depends on the distribution of the electronic clouds in the material which is related to the magnetisation. [13]

The alignment is dependent on the orientation of the magnetic moments controlled by $H_{ext}$. Due to its aspherical shape, the scattering cross-section of the charge distribution varies with the alignment of $M$. Therefore, for different orientations of the magnetisation, the magnitude at which the conducting electrons are scattered within the ferromagnetic layer and hence its resistivity changes [33]. The complex behaviour of the AMR between $B = 0$ and $B = B_{sat}$ (with $B_{sat}$ the field at which magnetisation saturation is achieved) is due to rearrangement of the magnetic domains. AMR is defined as:

$$AMR = \frac{\rho_{\parallel} - \rho_{\perp}}{\rho_{av}} \cdot 100 \quad [\%]$$

where $\rho_{av} = \frac{1}{3}\rho_{\parallel} + \frac{2}{3}\rho_{\perp}$ [31].

Figure 1.19 depicts the behaviour of ferromagnets in which the resistivity for a charge current $J$ parallel to the magnetisation differs by several percentages to that of the one perpendicular to the magnetisation. The difference between $\rho_{\parallel}$ and $\rho_{\perp}$ increases with increasing field until a saturation value $H_s$ at which all elementary magnetic moments of the ferromagnet are aligned parallel to

$H_{ext}$. Upon further increase of the external field, both resistivities increase equally. Table 1.8 shows values of AMR and $\rho_{av}$ at different temperatures.

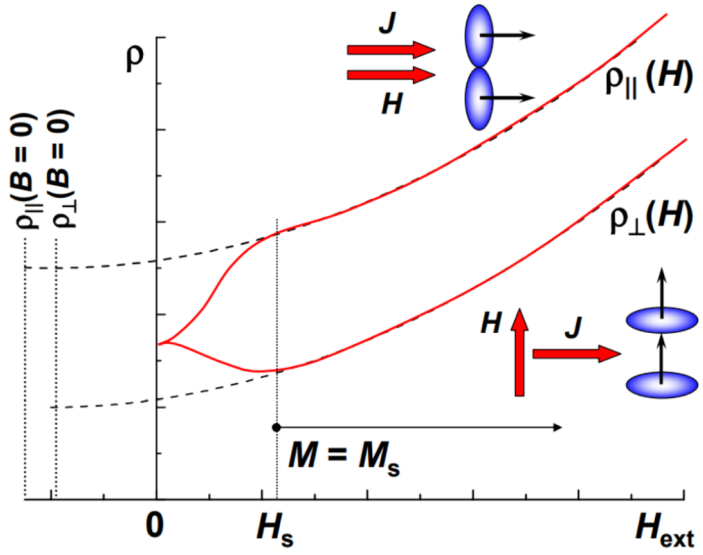


FIGURE 1.19: Resistivity as a function of applied field, $H_{ext}$. The resistivity obtained when the saturated magnetisation and the current flow are parallel is higher than the resistivity obtained in the perpendicular configuration. [20]

| Alloy | Temperature [ K ] | AMR [ % ] | $\rho_{av}$ |
|---|---|---|---|
| Fe | 300 | 0.2 | 9.8 |
| | 77 | 0.3 | 0.64 |
| Co | 300 | 1.9 | 13 |
| Ni | 300 | 2.02 | 7.8 |
| | 77 | 3.25 | 0.69 |

TABLE 1.8: Values of AMR and $\rho_{av}$ for bulk Fe, Ni and Co. [31]

### 1.1.3 Giant Magnetoresistance

Unlike the AMR effect, the giant magnetoresistance (GMR) effect is a pure quantum mechanical effect, and it is mostly observed in samples made of successive layers of FM material such as Co, Fe, Ni (and alloys) and non-magnetic (NM) metals such as Cu, Ag, Au. The GMR in multilayered structures comes from the reorientation of the single domain magnetic layers. The particularity of GMR is a large change in resistance caused by a small externally applied magnetic field. It differs from the conventional MR which is due to the effect of magnetic fields acting directly on the conduction electrons or on the scattering impurities. Usually the GMR effect is several orders of magnitude larger than the AMR effect. [41]

Figure 1.20 shows a typical curve of GMR effect. First, under a positive field, the magnetisations of the layers are aligned and electrons with spin parallel to the magnetisation are weakly scattered. Resistivity decreases. Then, under zero field, the magnetisations of the magnetic layers are randomly oriented producing a higher scattering rate. The resistivity increases. Finally, under negative field, the magnetisations of the magnetic layers are again aligned and the resistivity decreases.

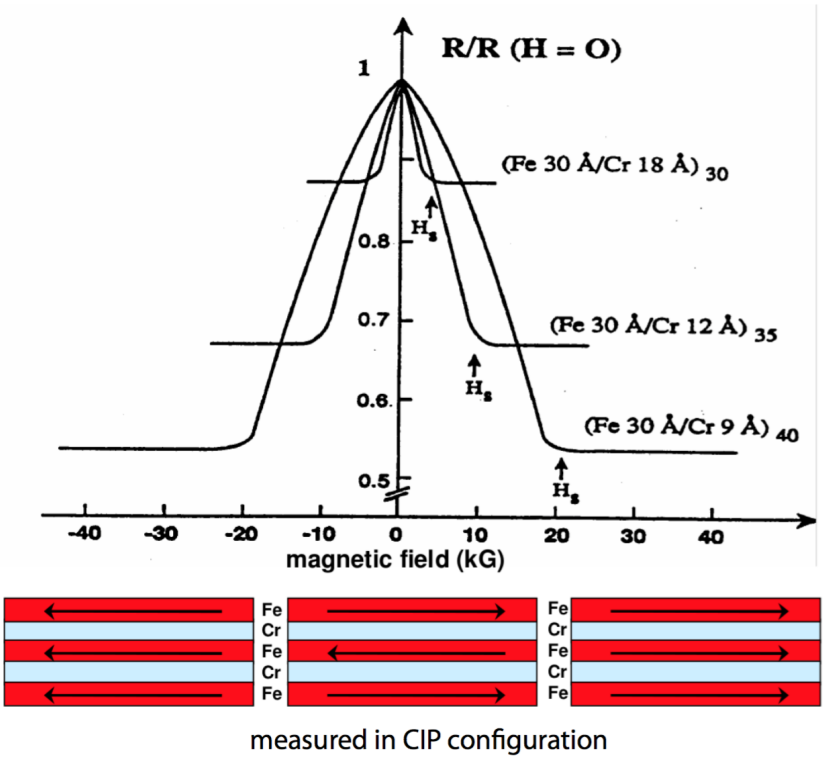


FIGURE 1.20: GMR of three Fe/Cr superlattices at 4.2K prepared by molecular beam epitaxy. [2]

The GMR effect can be used in different configurations as illustrated in figure 1.21: current in plane (CIP), the current flows in the plane of the layer, or current perpendicular to plane (CPP), the current flows perpendicular to the layers. In the case of the NWs studied in this thesis, the structure has a CPP configuration. In this configuration, it is quite obvious that electrons cross all the layers, but in CIP configuration, due to different scattering processes, electrons will cross all layers too. In appendix A.8 an illustration of this process is given.

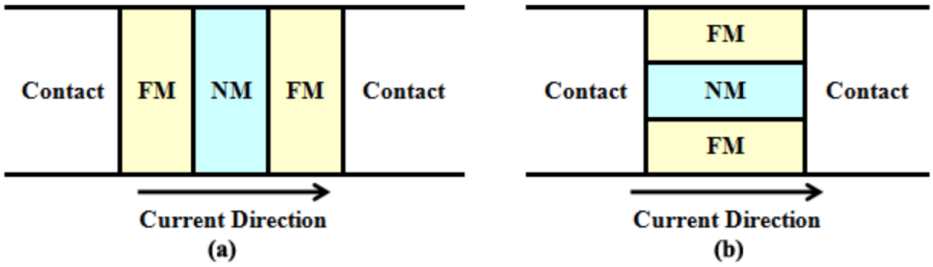


FIGURE 1.21: (a) Current perpendicular to plane CPP. (b) Current in plane CIP. [23]

In CIP geometry, GMR is due to classical size effect and quasi-exponentially decreases with the thickness of the paramagnetic layer. For CPP geometry, the total resistivity of the system may be calculated like the sum of the weighted resistivities in series for each spin channel, if one does not take into account spin-flip processes and spin-dependent potential barriers between layers. Due to the different scaling length in the two geometries – the electron mean free path in CIP and the spin diffusion length in the CPP – one observes larger CPP-GMR than CIP-GMR. Indeed, spin diffusion length has a size between 5 $nm$ up to 100 $\mu$m while the electron mean free path has a size between 1 $nm$ and 10 $nm$ [36].

From Mott's two current model, a resistor model can be achieved. When a ferromagnetic material has a spin independent resistance $R_f$ then the spin dependent resistances can be defined as:

$$R_{f,\uparrow} = \frac{2}{1+\beta} R_f \quad ; \quad R_{f_\downarrow} = \frac{2}{1-\beta} R_f \quad \text{with} \quad \beta = \frac{\sigma_\uparrow - \sigma_\downarrow}{\sigma_\uparrow + \sigma_\downarrow}$$

where $\beta$ is the conductivity spin polarisation coefficient in the magnet and, $\sigma_\uparrow$ and $\sigma_\downarrow$ are defined in equation (1.5). The absolute value of $\beta$ is between 0.3 and 0.8 [36]. If the non-magnetic spacing layer has a spin independent resistance $R_n$ then:

$$R_{n,\uparrow} = R_{n,\downarrow} = 2R_n$$

Figure 1.22 illustrates Mott's two current model. Scattering is strong for electrons with spin antiparallel to the magnetisation direction and is weak for electrons with spin parallel to the magnetisation direction. The overall resistance in the parallel ($R_P$) and antiparallel configurations ($R_{AP}$) of the device can be expressed as:

$$\frac{1}{R_P} = \frac{1}{2R_{f,\uparrow} + 2R_n} + \frac{1}{2R_{f,\downarrow} + 2R_n} = \frac{2R_{f,\uparrow} + 2R_{f,\downarrow} + 4R_n}{(2R_{f,\uparrow} + 2R_n)(2R_{f,\downarrow} + 2R_n)}$$

$$\frac{1}{R_{AP}} = \frac{1}{R_{f,\uparrow} + R_{n,\uparrow} + R_{f,\downarrow}} + \frac{1}{R_{f,\downarrow} + R_{n,\downarrow} + R_{f,\uparrow}} = \frac{2}{R_{f,\uparrow} + 2R_n + R_{f,\downarrow}}$$

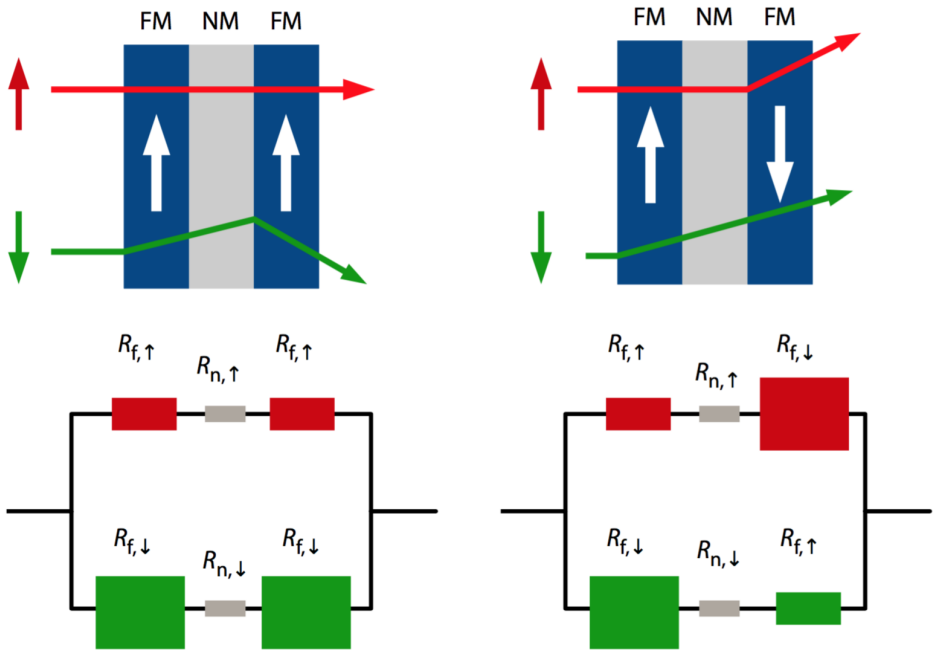


FIGURE 1.22: Resistor Model of a FM/NM/FM contact. [21]

The spin injection efficiency is defined as:

$$\alpha = \beta \cdot \frac{R_f}{R_n} \cdot \frac{2}{2\frac{R_f}{R_n} + (1-\beta^2)} \quad [\,-\,]$$

If $\beta = 1$, i.e. only majority spins (up-spins) are present in the ferromagnet, then $R_{f,\downarrow} \to \infty$ indicating that the resistance encountered by the (absent) minority spins (down-spins) is infinity. This

would give a perfect spin polarisation in the initial current, and as a result a perfect spin injection efficiency, $\alpha = 1$.

After some developments (see A.3.1), one obtains:

$$\text{GMR} = \frac{R_{AP} - R_P}{R_P} \cdot 100 \approx \frac{\beta^2}{1-\beta^2} \cdot 100 \quad [\,\%\,] \quad \text{if} \quad R_n << R_f$$

The resistor model explains qualitatively the working principle of a spin valve or GMR device by using Mott's two-current model, but it fails to explain the enhancement of GMR ratio by additional layers in the device structure.

Several models have been extended for GMR measurements to the case where the current is perpendicular to the plane, the so-called CPP geometry. The experimental results have been obtained in a two-current scheme with volume and interface resistances in series for each spin direction. The CPP-MR results were also explained by using the concept of "spin-coupled interface resistance" to describe the electron transport through an interface between ferromagnetic and nonmagnetic metals.

If the current is spin polarised in the ferromagnet, there will be spin accumulation at the edges of the interface with the nonmagnetic metal. The spin accumulation gives rise to an extra potential drop $\Delta V_I$, proportional to the current density $J$, $\Delta V_I = J r_{SI}$, where $r_{SI}$ is the "spin-coupled interface resistance". In particular cases, the successive interfaces of these spin-coupled interface resistance are additive [47].

Data can often be quantitatively understood with a semi-classical two current model with spin-diffusion lengths of the ferromagnetic layer and non-magnetic layer, $l_{sf}^F$ and $l_{sf}^{NM}$ respectively, as characteristic lengths in the CPP-MR. When the layer thicknesses are much shorter than the spin diffusion lengths, $t_F << l_{sf}^F$ and $t_N << l_{sf}^N$, the assumption of additive interface resistances is incorrect. The spin accumulation induced by successive interfaces interferes and partly balances the additive behaviour. In this case, the 2CSR model works well. On the opposite, when the magnetic layers are larger than the spin diffusion length ($t_F >> l_{sf}^F$) and the non magnetic layers are smaller than the spin diffusion length ($t_N << l_{sf}^N$), the VF model predicts that for multilayered NWs, the GMR results are inversely proportional to the magnetic layer thickness. The VF model is expressed as [17]:

$$GMR = \frac{R_{AP} - R_P}{R_P} \cdot 100 = \frac{2p\beta^2 l_{sf}^F}{1-\beta^2} \frac{\mathbf{1}}{\mathbf{t_F}} \cdot 100 \quad [\,\%\,] \tag{1.6}$$

with $p$ the faction of consecutive magnetic layers having antiparallel magnetisation ($p = 1$ for perfect anti-parallelism, $p = 0$ for perfect parallelism and $p = 0.5$ for random alignment). Appendix A.3.2 gives more information about the 2CSR and VF models. A comparison is also given between the electron mean free path ($\lambda$) and the spin diffusion length in Cu ($\lambda_{sf}$), which show that in general $\lambda_{sf}$=10$\lambda$. Deviations to the expression obtained at the limit are expected either in samples with thick layers (with smaller MR) or when impurities are introduced to enhance the spin-orbit effects and reduce $l_{sf}$. This show us that Cu is a good choice as spacer. Indeed, this is related due to the fact that all the 3d states are situated below the Fermi level, and not available for scattering processes. Cu shows thus high conductivity.

**Temperature dependence** In the CPP-GMR geometry, different effects contribute to the variation of the GMR with temperature [17]:

- Inelastic scattering processes by phonons or magnons (including interface phonons and magnons) add up to elastic scattering processes by imperfections. This effect will change $\beta$ and $\gamma$, resulting in a reduced GMR ratio.
- Electron-magnon scattering with spin-flip transfers momentum between the spin $\uparrow$ and spin $\downarrow$ currents. This results in a spin-mixing effect, reducing the GMR.
- The global scattering rate increases with increasing temperature and so the SDL is shortened. As a consequence, the variation of the GMR with thickness is more pronounced.

At relatively high temperatures, the onset of electron-magnon collisions should bring a third channel for the spin relaxation: spin transfer from light conduction electrons to heavy $d$ electrons and then spin-lattice relaxation via spin-orbit interactions. Furthermore, it will induce exchange between the two spin channels, leading to a reduced effective value of the resistivity asymmetry between the two spin channels. The resulting effect on the spin accumulation process is difficult to predict accurately but this should affect significantly the temperature dependence of the MR.

**From CPP to CIP configuration** When GMR was first discovered, the CIP configuration was used. Very thin layers were made, to observe the effect, and to allow the electron to go through the different layers. In the case of CoCu/Cu samples, ferromagnetic or antiferromagnetic coupling of the magnetic layer occured. This phenomenon is called "oscillating exchange coupling" or "exchange anisotropy" [10]. It is observed for very thin layers of about $\sim 1\ nm$. The coupling vanishes above a critical non ferromagnetic spacing and oscillates with the thickness of the spacer, as shown in figure 1.23 and 1.24. However, later when the CPP configuration was possible thanks to the electrodeposition technique (see next section), the layer could be made larger because the current crossed all the layers. In this thesis, much larger Cu layer were fabricated ($t_{Cu} > 5nm$). This phenomenon is thus not observed, but there are still interactions between the layers (such as dipolar coupling) which are dependent on the spacer thickness.

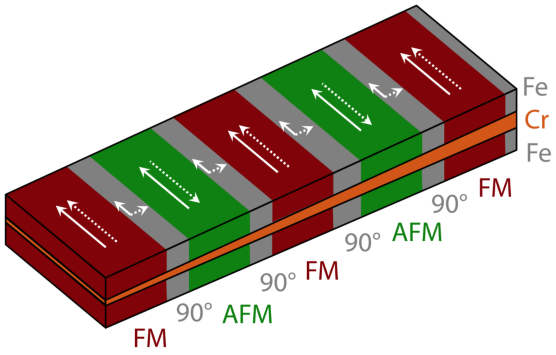


FIGURE 1.23: Oscillating exchange coupling. [21]

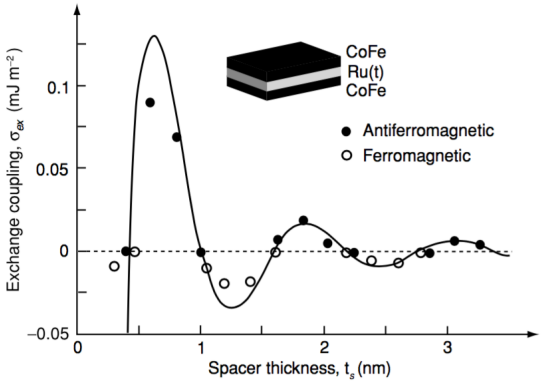


FIGURE 1.24: Evolution of exchange coupling with Cu layer thickness. [10]

## 1.2 Ferromagnetic nanowire network

In this master thesis, crossed networks of NWs are studied. This configuration allows several advantages including mechanical stability and self-supporting structure after chemical dissolution of the polymer membrane. Moreover, magnetotransport measurements are easier to carry out thanks to the high nanowire electrical connectivity. In this section, the fabrication process to create the CNWs is described. The different steps to build homogeneous and multilayered NWs are also specified. Then, because of the reduced size with respect to bulk materials, the magnetic and

magnetotransport properties are changing. To understand these changes, properties of single NWs are explained first. Then, those of parallel NW arrays are pointed out, and finally those of crossed NW networks.

### 1.2.1 Fabrication process

The nanowires are created by electrodeposition into pores of a membrane. The fabrication process described below allows to get different types of morphology: homogeneous nanowires, nanocables, nanotubes and multilayered nanowires as seen in figure 1.25. The porous polymer membrane acts as template for the synthesis of nanostructures of the desired materials. Because the pores within the membranes are cylindrical and of similar diameter, monodisperse nanocylinders of the desired material are obtained. Depending on the chemistry of the pore wall and material, these nanocylinders may be either hollow or solid. Different angle distributions are possible.

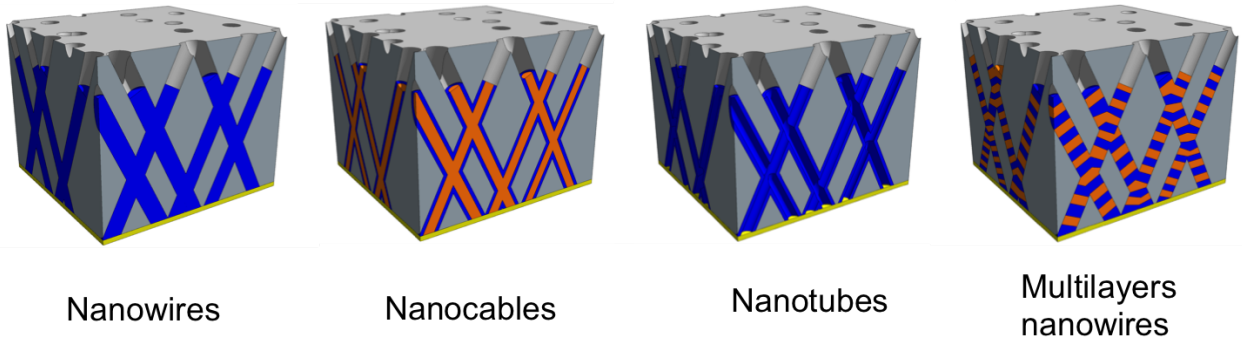


FIGURE 1.25: Different types of morphology when doing electrodeposition in track-etched membranes.

**Track-etched membranes**

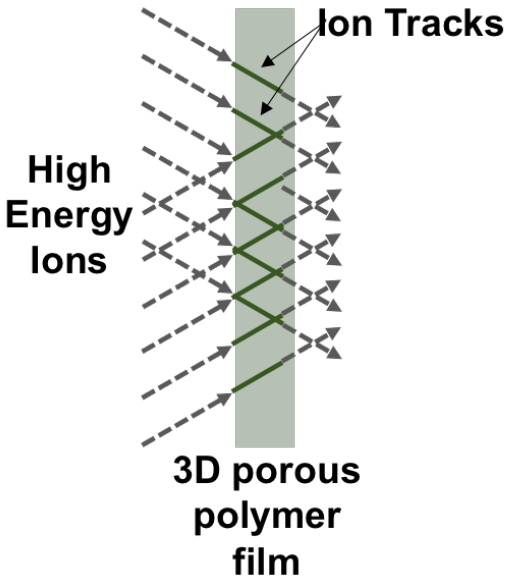


FIGURE 1.26: Sequential ion bombardment with inclination angle with respect to the normal. [8]

Templates can be prepared thanks to nuclear track etched technology. A non-porous sheet is entailed by bombardment of heavy ions of high-energy accelerated in a cyclotron. The PC template is subjected to two irradiation steps over a wide angular range with respect to the normal of the PC surface as shown in figure 1.26. This allows to form a complex 3D nanochannel network. The nuclear fission fragments create damage tracks in the material. The next step is a chemical etching into pores with a diameter depending on the etching time. The resulting membranes contain randomly distributed cylindrical pores of a diameter laying between a few nm to a few hundreds of nm. The sheet has a thickness in the range of 6 to 50 $\mu m$ [24] and the resulting porosity can vary between different values but stays below $40\%$. In this thesis, the membranes were prepared from polycarbonate. Other materials such as PET[a], PF[b] or anodic alumina can also be used.

[a] Polyethylene terephthalate
[b] Phenol formaldehyde resins

The main advantages of such membranes are their versatility, chemical, mechanical, and thermal stability and their smooth and flat surface. Moreover, various sizes of nanowires diameters and different types of porosity are possible. However, the main limitation of this kind of membrane is the lack of a well-defined spatial pore arrangement.

**Electrodeposition**

This technique is an easy and elegant method. It provides an alternative to more complicated methods such as beam epitaxy and microlithography for the synthesis of the desired materials within the pores of a nanoporous membrane. This method allows control of the material composition (pure metals and alloys), but control of the length of the nanowire by varying the amount of deposited metal is also possible. The ability to control the length or aspect ratio of the metal NWs can be an important point because the magnetic properties of nanometals are dependent on aspect ratio [22]. The electrodeposition of metals consists of an electrochemical process by which metallic ions from an electrolyte are reduced to form a solid deposit in the cathode of an electrochemical cell, according to the equation:

$$M^{n+} + n^{e-} \longleftrightarrow M \tag{1.7}$$

This reversible electrochemical reaction is characterised by an equilibrium potential $E^{eq}$, which is dependent on the activities of ions $a_{M^{n+}}$ and metallic ions $a_M$, according to the Nernst equation:

$$E^{eq} = E^0 + \frac{RT}{nF} ln \frac{a_{M^{n+}}}{a_M} \quad [\,\mathrm{V}\,]$$

where $R$ is the ideal gas constant, $F$ the Faraday constant, and $E^0$ is the normal electrode potential. Values of $E^0$ for the metals of interest are given in table 1.9. As the metal need to be deposited in the pores of the template, one needs to favour the $\longrightarrow$ direction in equation (1.7). As a consequence, a potential lower than $E_0$ must be applied.

| Metal/ion couple | $E^0$ (V) |
|---|---|
| Copper/$Cu^{2+}$ | 0.34 |
| Nickel/$Ni^{2+}$ | -0.26 |
| Cobalt/$Co^{2+}$ | -0.28 |
| Iron/$Fe^{2+}$ | -0.44 |

TABLE 1.9: Normal electrode potentials.

The mass $m$ of the material deposited during the electroplating process is related to the cathodic current $I(t)$ that flows through the electrochemical cell, according to Faraday's law:

$$m = \frac{M_M}{nF} \int_0^t I(t')dt' \quad [\,\mathrm{g}\,]$$

where $M_M$ is the molar mass of the metal M and $t$ the duration of the process.

To be able to accomplish an electrochemical deposition of a material within the pore of the PC template, one needs to coat one face of the membrane with a metal film (sputtering or thermal evaporation) and use this metal film as a cathode for electroplating.

Figure 1.27 presents the different steps of the electrodeposition process. First, a certain template is selected and fixed on the Teflon cell (figure 1.27(a)). The electrolyte is placed in the cell. The counter electrode and reference electrode are placed in the electrolytic bath (figure 1.27(b)). The metallic deposit acts as the cathodic electrode and is coated during the electrodeposition process.

The electrodes constitute good electronic conductors, are resistant to corrosion and are all separated by the electrolyte. The potential of the cathodic electrode, measured against the reference electrode, is kept constant by using a potentiostat; the cathodic current density is measured simultaneously to monitor the process. Figure 1.27(c) illustrates the cell during the electrodeposition process showing the growing nanowires.

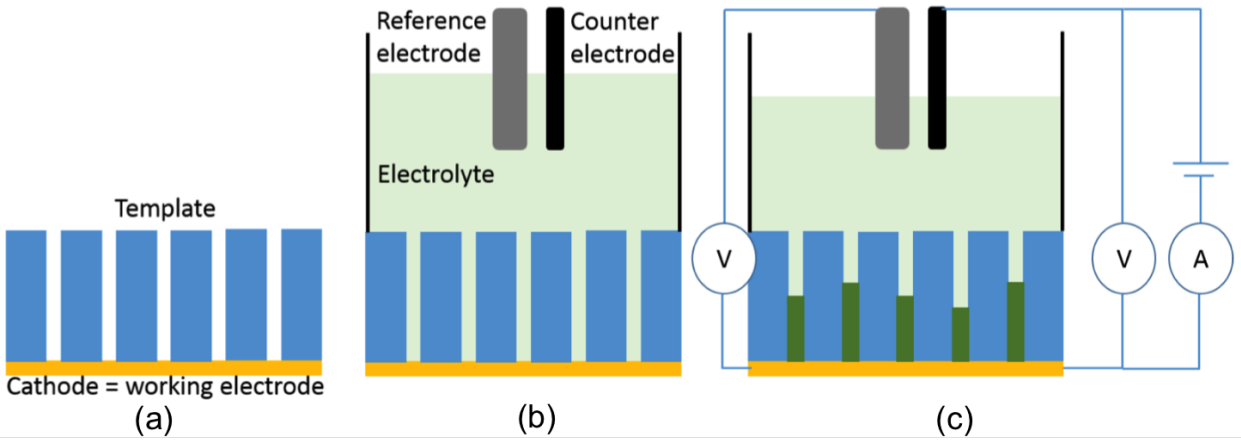


FIGURE 1.27: Schematics of the electrodeposition process. (a) PC-template with the Au or Cu cathode. (b) Template placed in the cell with the electrolyte inside. The counter electrode and the reference electrode are shown. (c) Growing NWs during electrodeposition process. [6]

Metallic alloy electroplating requires the co-deposition of two or more metals from a single electrolyte. Therefore, adequate proportions of ions of metals to be alloyed have to be present in the electrolyte, and the electrochemical reduction potentials of the ions have to be close enough to each other to guarantee the simultaneous deposition of the desired metals. The creation of multilayered NWs is possible if one considers two material with sufficiently different $E_0$. For example, to create multilayered NWs composed of material A with $E_0$ higher than the $E_0$ of material B, a very low concentration of material A is inserted to form the electrolyte. At higher potential, only this material A will be deposited while when the deposition is done at lower potential, materials A and B will be deposited. As the concentration of material B is much higher than material A, a uniform layer of material B will be created. By alternating the time of deposition and the voltage (as shown in figure 1.28), the multilayered NWs can be fabricated from a single bath.

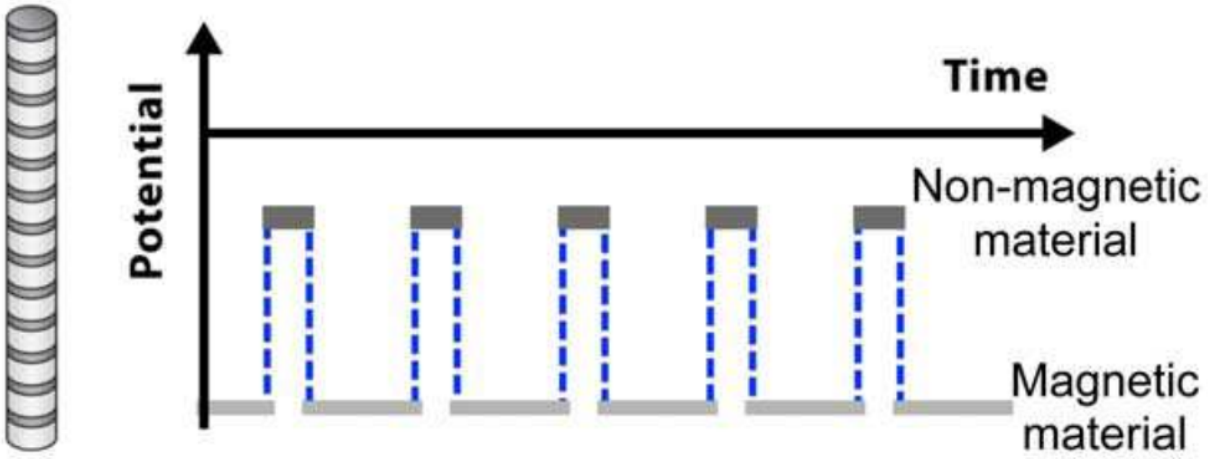


FIGURE 1.28: Programmed electrical parameters for the electrodeposition, with alternating potential. The grey lines represent the deposition of the different materials. [39]

In addition of selecting which material will be deposited, the deposition potential can also influence the structure of the deposited material. For example, the crystallographic structure of the CoCu layers can be controlled by deposition parameters such as the deposition potential or the pH of the electrolyte. Figure 1.29 shows the dependence of the Co magnetic layer on these parameters; how an fcc structure with no magnetocrystalline anisotropy can be obtained, or an hcp structure in which the orientation of the c-acis can be fixed either parallel or perpendicular to the wire axis, introducing an important magnetocrystalline anisotropy contribution.

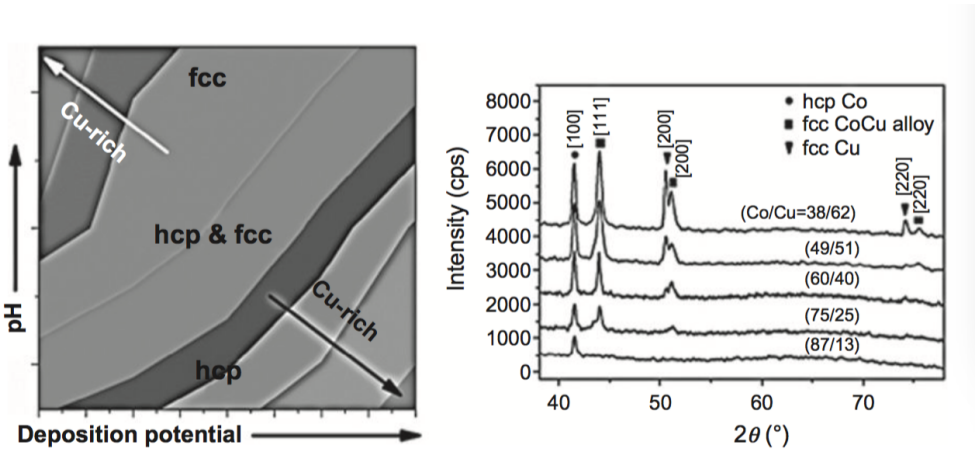


FIGURE 1.29: (Left) Qualitative dependence of the composition and crystalline structure of the electrodeposited cobalt (Co)- copper (Cu) nanowires on the pH and deposition potential. (Right) X-ray diffraction patterns measured on Co-Cu nanowire arrays for different Co-Cu ratios. [10]

### 1.2.2 Single nanowires

When comparing the bulk magnetic properties of Ni and Co to their nano-magnetic properties, various changes appear. For example, single nanowires present much enhanced coercivities in the range of the kOe; for nanowires arrays of Co and Ni, coercivities in the range of 150 to 690 Oe are observed; bulk Ni and Co possess values of a few Oe. This is expected because larger wire diameters facilitate the formation of multi-domains, hence degrading the coercivity. Results suggest that coercivity can be further increased for NWs with a diameter less than 50 nm [49], [40].

### Shape anisotropy

Due to the shape anisotropy, the magnetic properties will be different if the field is applied along the wire axis (easy axis) or perpendicular to the wire axis (hard axis). Figure 1.30 shows two different hysteresis loops. In the first image, the field is applied in the easy direction while on the second image the field is applied in the hard direction. There is no hysteresis in the perpendicular direction of a single wire. An important external magnetic field is needed to align the magnetic moment perpendicular to the wire axis because of the high shape anisotropy. In addition, when the field is removed, the magnetic moments goes directly back to the direction parallel to the axis.

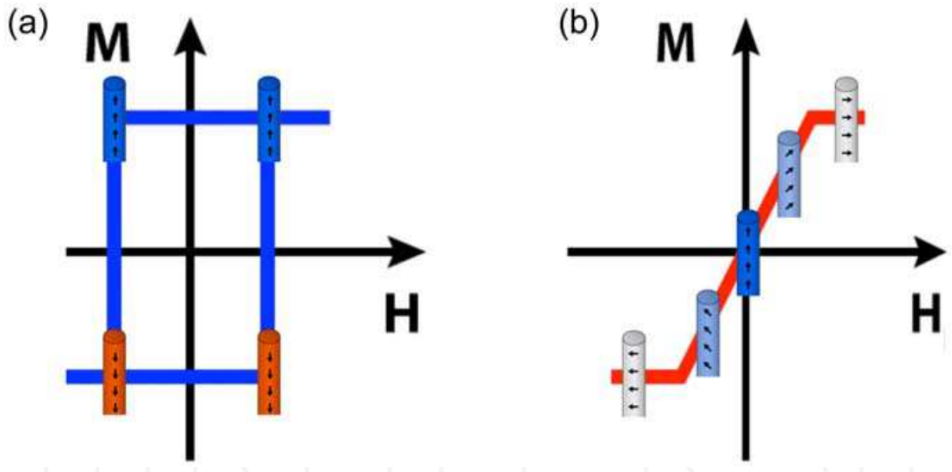


FIGURE 1.30: Hysteron based on the theoretical behaviour of an individual nanowire, depending on the applied field direction. (a) Axially applied field: easy axis hysteron. (b) Transversely applied field: hard axis hysteron. [39]

### Magnetocrystalline anisotropy

In NWs, usually the shape anisotropy dominates the magnetocrystalline anisotropy. For fcc structures, adopted in NiCo alloys, the magnetocrystalline anisotropy is negligible. However, in some case the crystallographic structure can influence the effective anisotropy. For example, Cobalt can adopt an fcc or an hcp structure; depending on the type of structure, the magnetisation will preferentially adopt a certain direction. The crystallographic structure of Co can be modified by changing the electrolytic bath's acidity. Figure 1.31 shows diffraction patterns of Co CNWs deposited at different pH. The results show that different crystallographic structures are obtained when the pH is modified. At pH 2, no favourable structural texture appears. When the pH increases (pH 3.6 and pH 5), the hcp Co easy axis is mostly oriented perpendicular to the NW axis. At pH 6, the easy axis reorients along the NW axis. Figure 1.31 shows also that the grain size is changing with the pH. Lower pH presents higher grain sizes than higher pH.

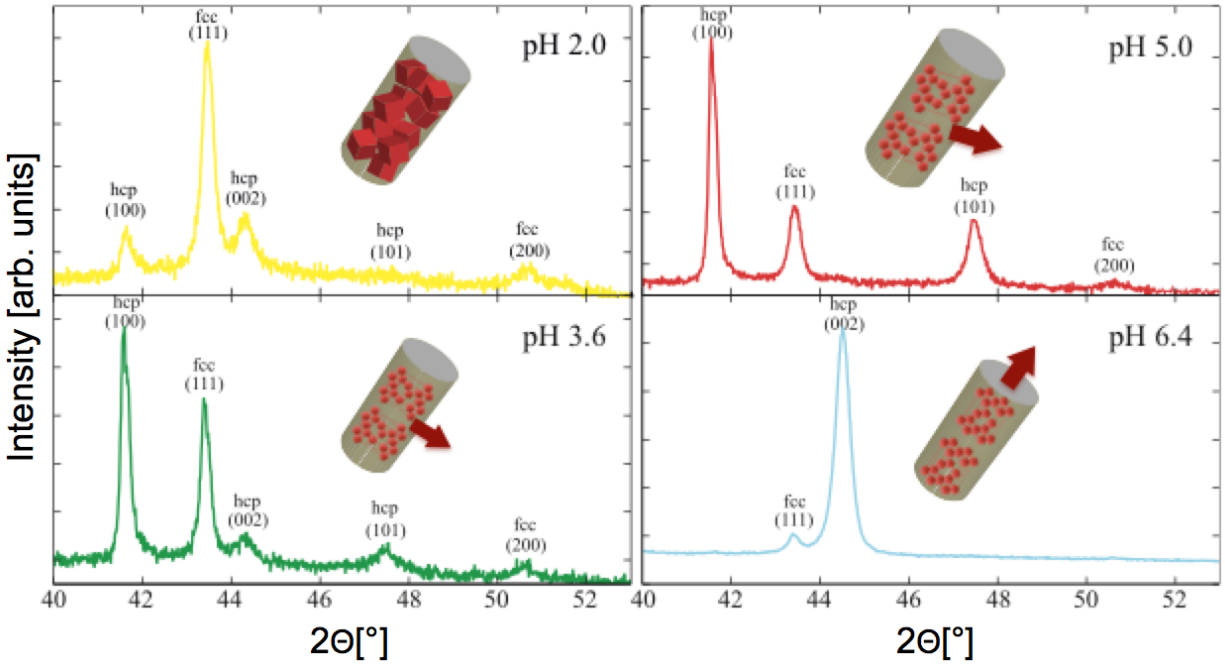


FIGURE 1.31: X-ray diffraction pattern of Co CNWs samples for electrolytic bath solution of different pH. [8]

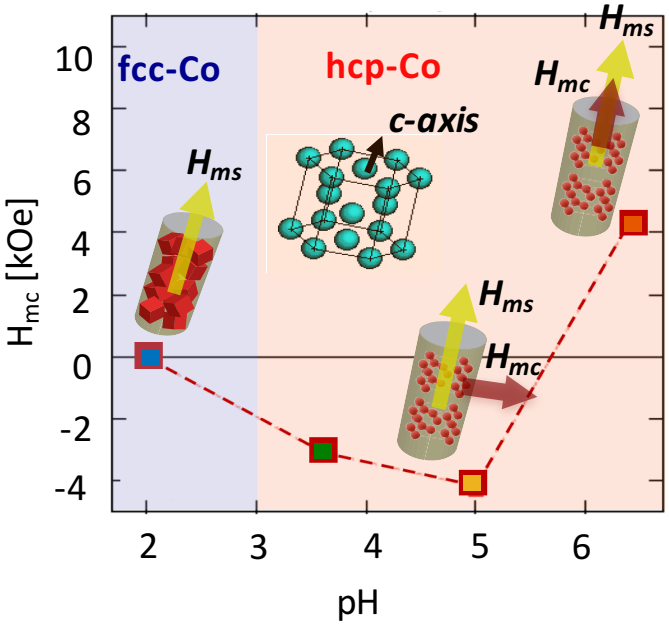


FIGURE 1.32: Magnetocrystalline anisotropy as a function of pH. [8]

Figure 1.32 summarises the change of crystalline structure with the pH (from fcc to hcp). The image also shows the variation in $H_{mc}$. There is a significant decrease in the saturation field of Co CNWs grown at pH values of 3.6 and 5 compared to the pH2 sample, and then an important increase when going to pH6.4. At pH2, the dominant energy contribution is magnetostatic (MS) anisotropy. Then, a competition between MS and magnetocrystalline (MC) anisotropy is present in the case of pH3.6 and pH5; while for pH6.4 the two anisotropies are added to each other.

**Dipolar interaction in multilayered NW**

When constructing multilayered NWs, dipolar interaction appears between the different ferromagnetic layers. This effect arises as a result of the creation of a larger number of interfaces with dipoles as shown in figure 1.33. Subfields $H_n$ are created, which are forming a total demagnetising field along the axial direction. As the number of layers increases, the number of interface also, their

effect on the total magnetostatic energy central element can be described considering the fields generated from the pair interaction among sequentially ordered interfaces [12].

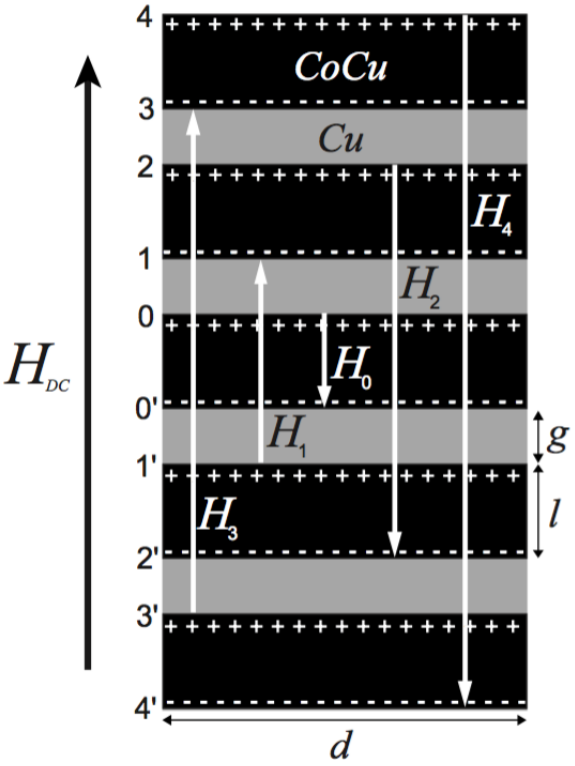


FIGURE 1.33: Dipolar coupling inside a multilayered nanowire of diameter $d$. The Co thickness is $l$ and the Cu thickness is $g$. The demagnetising field are the $H_n$ and appear as result of the polarisation of the magnetic layers under biasing by magnetic field $H_{DC}$ [12].

**Change in resistance**

The reduction in size of samples can lead to both qualitative and quantitative changes in comparison to electrical transport in wires of much larger dimensions. The size reduction leads to a reduction of the magnetic contribution to electrical resistivity [26]. The decrease can be related to an increase in relative surface to volume ratio. As more surface atoms have missing bonds, vibrational amplitudes increase with low frequencies and hence the Curie temperature decreases. This implies that the magnetisation and hence the interaction strength is reduced upon size reduction. A mechanism is suggested for this reduction in case of NWs, in which the contribution of the disordered spins at the surface becomes increasingly important. These disordered surface spins may not support long wavelength propagating spinwaves that are needed for the temperature dependent resistivity of the type that gives $\rho_M$ (the resistivity coming from electron-spin scattering).

An increase of the residual resistivity as the diameter decreases is often observed due to increased surface scattering. The RRR of a single nanowire of $\varnothing 50$ nm ($\sim 2.3$) is much less than that of a bulk wire of $\varnothing 50$ $\mu$m ($\sim 312$). Figure 1.34 illustrates both of these effects, plotting the temperature vs the resistivity.

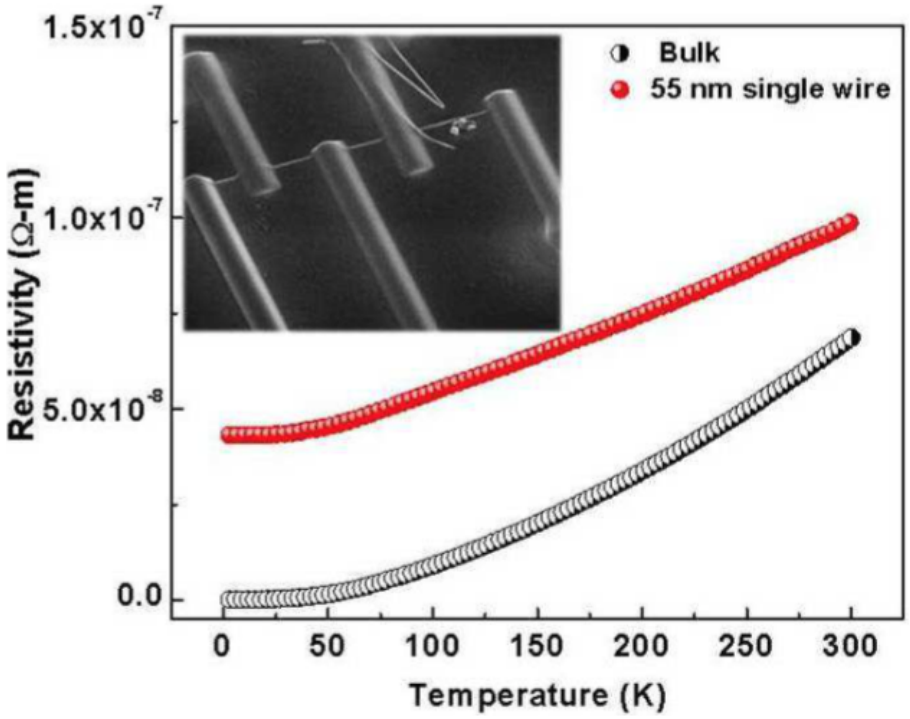


FIGURE 1.34: Comparison between bulk and nanowire resistivity. [26]

### 1.2.3 Parallel nanowire arrays

The magnetic and magnetotransport properties will vary if one considers only one nanowire vs a 3D array of nanowires. Indeed, the behaviour of a group can not simply be reduced to the sum of the individual behaviours: there are interactions between the wires. Depending on the distance that separates the nanowires, more or less dipolar interactions must be taken into account, and as a consequence more or less anisotropy will be present. Also, when looking at properties of multilayers, an additional interaction emerges: dipolar interaction between the layers.

#### Changes in magnetic properties

**Dipolar interaction between nanowires** In the case of a low porosity template, the wires are more independent and show a behaviour closer to the one of a single nanowire. On the opposite, when the porosity increases, interactions appear. When increasing the membrane porosity, the effective uniaxial anisotropy $H_{EF}$ is reduced. This effect results from the dipolar coupling between the wires. Figure 1.35 shows this effect. In the low porosity sample (a), the easy magnetisation axis can easily be distinguished from the hard magnetisation axis while on the second figure (b), the two magnetisation axes are almost indistinguishable. Figure (a) corresponds to a hysteresis loop of a highly anisotropic system (low saturation field and high remanence in parallel direction; high saturation field and low remanence in perpendicular direction). Figure (b) corresponds to the behaviour of an isotropic system with identical cycles. The final shape of the hysteresis loop is thus a combination of both: the diameter of the NWs and the porosity of the membrane. The aspect ratio (depending on the diameter of the NWs) defines the importance of the shape anisotropy while the porosity defines the importance of the dipolar coupling. Small diameter and low porosity will produce a squared hysteresis loop while large diameter and high porosity will produce a more isotropic hysteresis loop.

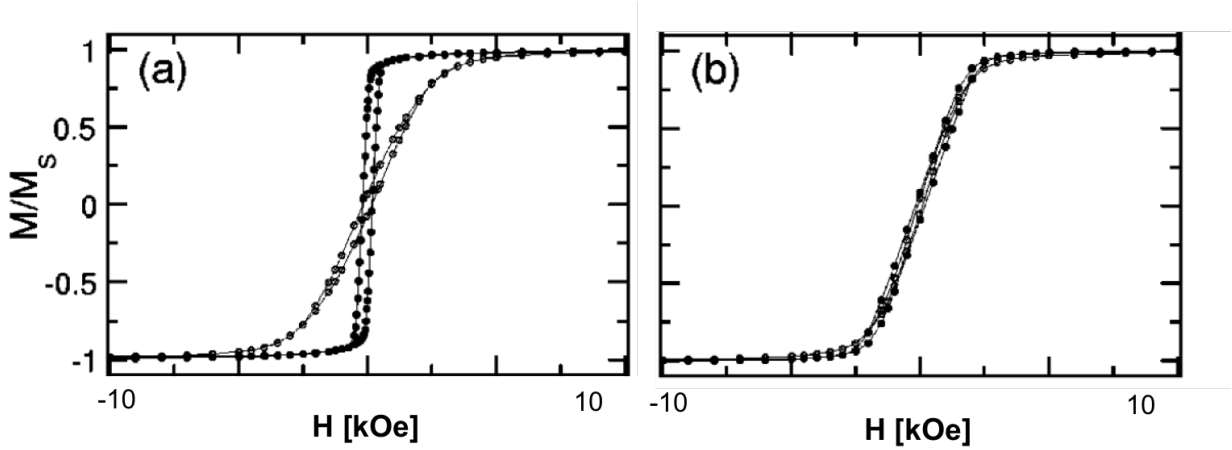


FIGURE 1.35: Normalised hysteresis loop in direction parallel to NW axis (filled circles) and in direction perpendicular to NW axis (empty circles). (a) NW diameter 56 nm and porosity of 4%. (b) NW diameter of 250 nm and porosity of 35-38 % [15].

The effect of the dipolar coupling can be taken into account by including an additional uniaxial anisotropy field, $H_U > 0$ which favours an easy axis perpendicular to the wires.

$$H_{EF} = 2\pi M_S - H_U = 2\pi M_S(1 - 3P) \quad [\,\mathrm{A \cdot m^{-1}}\,]$$

with $P$ the nominal porosity of the sample, defined as the product of the pore density and the pore surface [15]. It has been shown that $H_U$ increases almost linearly with increasing porosity. This linear dependence of the dipolar coupling on the porosity can be derived using a mean field approach. Upon decreasing the wire separations, the wires start to interact via their dipolar stray fields which adds to the restoring torque of the individual wires and changes the resonance frequency [15].

As also multilayered NWs are considered, the interaction between the layers must be added to the interaction between the wires. When the $t_F >> t_N$, the dipolar field can be expressed as a dipolar field created by an array of HCNWs and thus coming from the interaction between the NWs, as shown on figure 1.36(a). Otherwise, $H_{eff}$ must be weighted by a new factor; and finally contains two part: one corresponding to the effective magnetostatic field of a single infinitely long wire which interacts with the wires inside the array; and a new term which takes into account the additional magnetostatic interaction between the layers. When the dipolar coupling between the layers is important, then the hysteresis loop become isotropic as shown on figure 1.36(b).

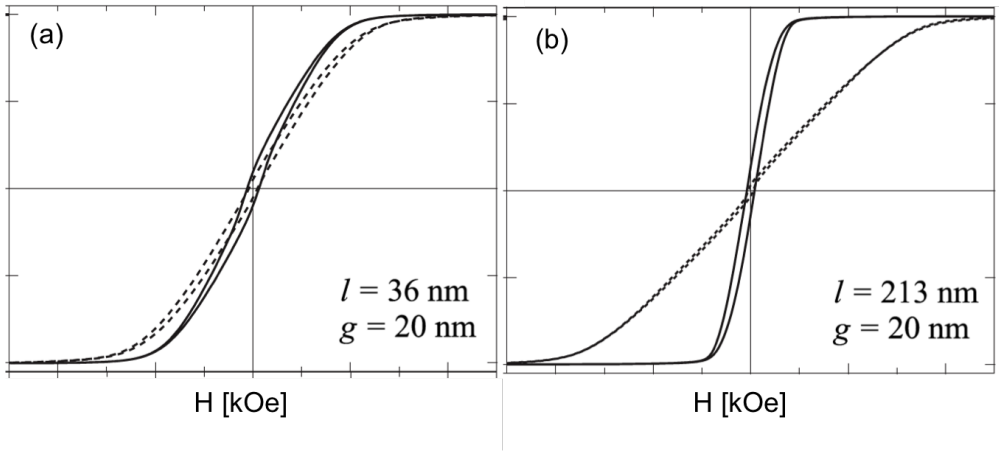


FIGURE 1.36: Hysteresis loop with applied field $H_{\parallel}$ and $H_{\perp}$. $l$ stands for the ferromagnetic layer thickness and $g$ for the non-magnetic layer thickness. The two loops are obtained from samples with the same porosity [12].

**Comparison between single NWs and parallel NW arrays** As a consequence of this new interaction, the hysteresis loop obtained from single nanowire will be different than the one from a parallel NW array. Figure 1.37 shows this difference. In the case of a single NW, the hysteresis loop for the parallel direction is square in shape showing the bistable behaviour of this wire, where the magnetisation reverses in a single jump (illustrated in figure 1.37(B)). In contrast, in the case of an array of NW, the hysteresis loop measured along the parallel direction is less abrupt (as illustrated in figure 1.37(A)).

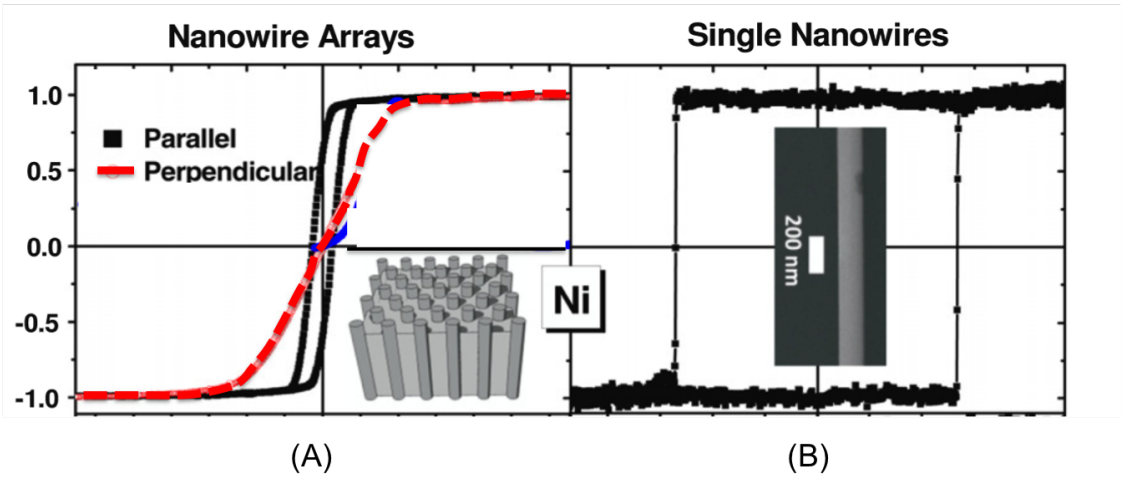


FIGURE 1.37: Comparison between the hysteresis loop of a nanowire array (left) and single nanowire (right). [48]

The squareness is always more visible, and the coercive field higher, for a single nanowire than for a NW array. Indeed, other interactions need to be taken into account for a NW array such as the demagnetising field originating from the magnetostatic coupling among NWs in the array. As a consequence, changes in coercivities are observed. Figure 1.38 illustrates this variation. However, the nanowire arrays show still relatively high coercivity values, ranging from 400 Oe for pure Ni to about 200 Oe for $Co_{0.5}Ni_{0.5}$ .

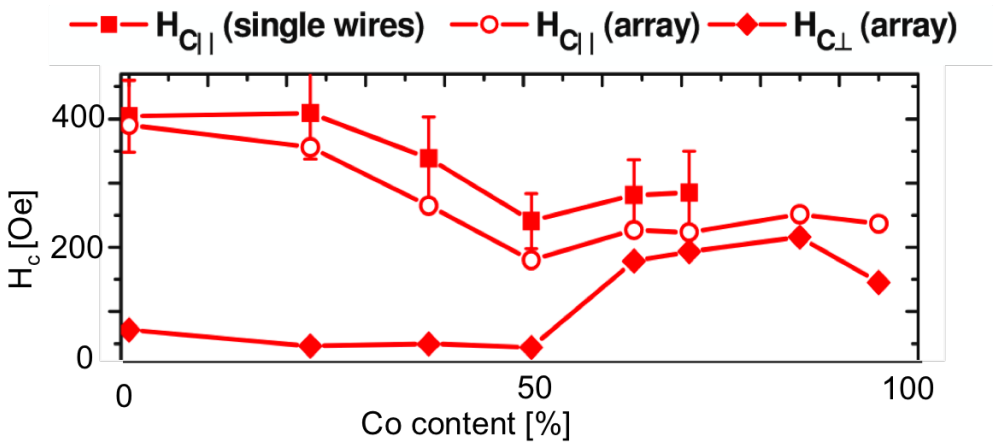


FIGURE 1.38: Coercive field as a function of cobalt content in case of a single nanowire and of a nanowire array [39].

Homogeneous NWs present higher shape anisotropy then multilayered NWs. Indeed, additional interactions between the layers arise in the case of multilayers and will compete with the shape anisotropy. As a consequence, the shape anisotropy can be controlled as a function of the ferromagnetic layer thickness which will define the aspect ratio and the non-magnetic layer thickness. At high aspect ratio (large magnetic layer), the magnetisation prefers to align parallel to the axis of the multilayered plane, or towards the length of needle-shaped nanoparticles, dots or wires. On the contrary, at low aspect ratio, cylindrical disks are obtained, which favours an easy magnetisation direction perpendicular to the cylinder axis. Similar effects will be seen when the non-magnetic layer increases: there will be a decrease of the easy axis in the OOP direction because of a decreased coupling between the successive layers; the system will be comparable to successive independent disks.

### Changes in magnetotransport properties

**Anisotropy magnetoresistance** AMR measurement constitutes a way to investigate magnetic-transport properties of NWs. AMR leads to changes in the resistivity when the angle between the direction of the magnetisation and the current is modified. As the current goes along the axis of the NWs, the high resistance state corresponds to the situation where the current is parallel to the magnetisation ($\rho_{||}$) and the low resistance state when the current is perpendicular to the magnetisation ($\rho_{\perp}$).

Figure 1.39 shows AMR curves of Ni and Co arrays. For the Ni arrays, almost no variation of resistance appears when an external field is applied parallel to the wires. This shows us that the wires keep their magnetisation along the axis of the wire throughout the reversal process. When the field is applied perpendicular to the axis of the wires, the resistance decreases; the external field forces the magnetic moments to lay perpendicular to the current, allowing higher conductivity. In contrast, for the Co array, the resistance decreases when the field is applied perpendicular to the current, while the effect is reversed when the field is parallel to the current. This effect shows the coexistence of transversally and axially magnetised domains in the zero field state. Indeed, as explained before, Co NWs can present magnetocrystalline anisotropy, which will favour an easy axis perpendicular to the wire direction. This effect will add to magnetostatic effects. On the contrary, the shape of the GMR curve is predominantly dictated by the MS effect for the Ni. One can observe the same effect on thinner diameter Co NW array. [17].

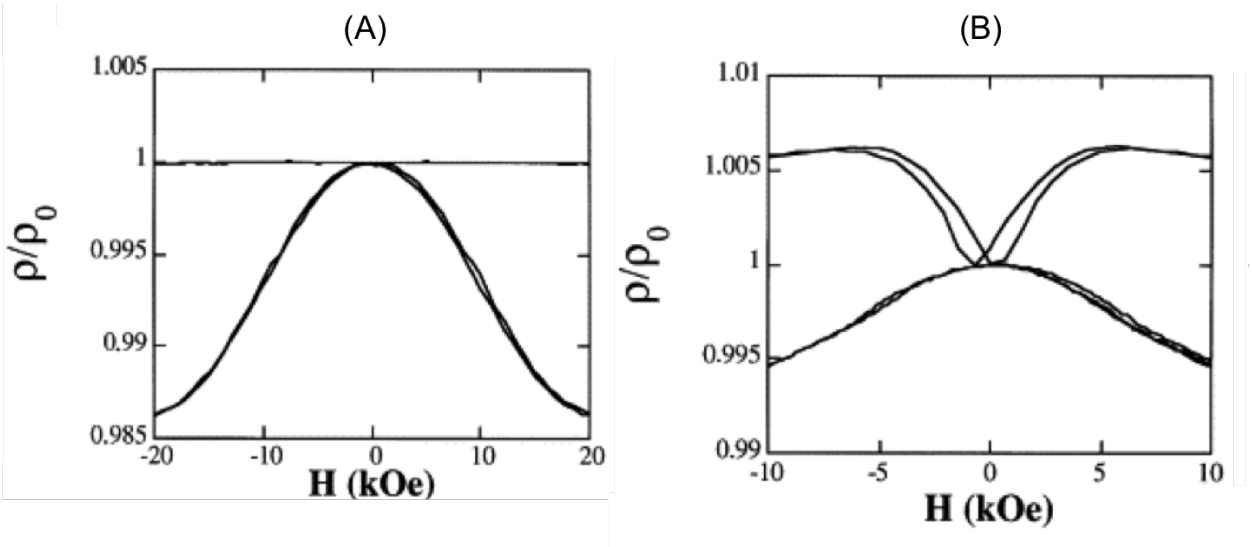


FIGURE 1.39: AMR curves obtained for arrays of (A) Ni nanowires and (B) Co nanowires. Both nanowires arrays have nanowires with $\varnothing = 90nm$. Applied field perpendicular (bottom curve) and parallel (top curve) to the nanowires axis [17].

**GMR** GMR is only observed in multilayered NWs. In the case of CPP-GMR for nanowire array, impressive results of GMR have been measured. Figure 1.40 shows the GMR curve of a NiCoCu/Cu sample growth by electrodeposition in nanoporous aluminum oxide membranes. The curves show the very large values obtained for a field direction perpendicular to the axis of the wire [16]: 55% at room temperature and 115% at 77K. The CPP-GMR measured for this NiCoCu/Cu nanowire is 2.5 times greater than similar nanowires electrodeposited in PC templates. The difference in results between the two templates could be related to the fact that reactants diffuse more easily along the pores in the aluminum oxide membranes.

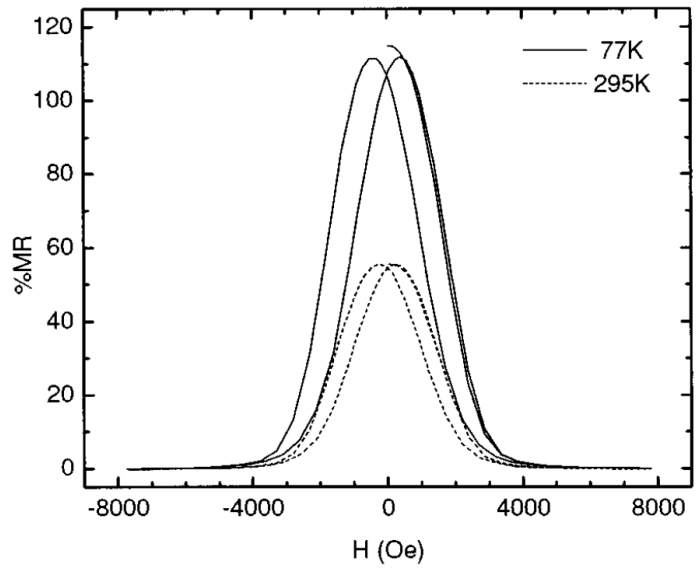


FIGURE 1.40: Current perpendicular to plane GMR for a multilayered nanowire with applied field perpendicular to the NW axis direction. [16]

### 1.2.4 Crossed nanowire networks

When speaking about CNWs, parallel and perpendicular directions are not relevant anymore but IP and OOP direction are better suited. Indeed, the wires are not all aligned in the same way, so it is easier to speak about the direction of the template. Figure 1.41 shows how the template is placed in the magnetic field with the related wires directions. If the angle between bombardment and the normal is not too large, the direction IP is close to the perpendicular direction (for parallel nanowires) and the direction OOP is close to the parallel direction.

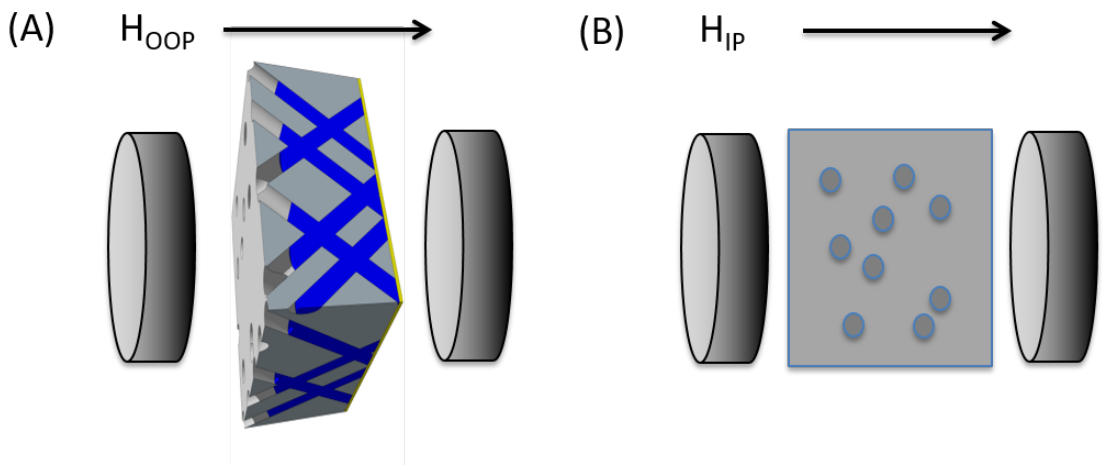


FIGURE 1.41: (A) OOP (B) IP. The grey cylinders represent magnets.

Some notations are defined to avoid mixing concepts. $\parallel$ and $\perp$ are indices referring to an element parallel or perpendicular respectively to one nanowire. For example, $H_{\parallel}$ and $H_{\perp}$ are the applied magnetic field parallel and perpendicular to a NW; $\rho_{\parallel}$ and $\rho_{\perp}$ are resistivity measured parallel and perpendicular to one NW. The indices OOP and IP refer to the whole array of CNWs. Figure 1.42 shows these different notations. The angle $\alpha$ is defined as the angle between a NW and the OOP direction. This angle can vary between the different NWs. Finally, the notations $H_{IP,\parallel I}$ and $H_{IP,\perp I}$ are referring to a magnetic field applied to the sample in the IP direction with a current going either parallel or perpendicular to this field direction.

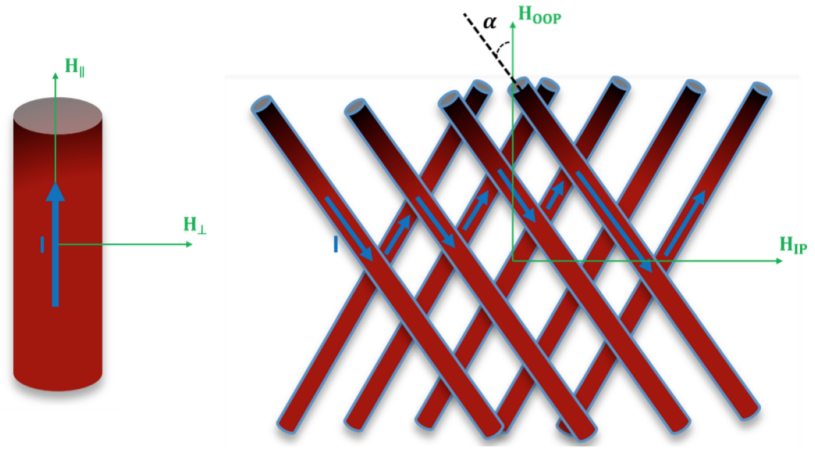


FIGURE 1.42: Notation for parallel and perpendicular elements to one nanowire and IP and OOP directions for a whole array of CNWs.

Figure 1.43(a) and (b) illustrates how multilayers can be superimposed. Two models are possible: one with a filling (and thus interface between layers) that are parallel to the cathode; another with the interfaces between the layers that are perpendicular to the nanowire wall. In both models, the layers are well defined. This is the most important feature to observe GMR effect. One supposes that the filling must be something in between the two simplified illustrations. The crossing zone presents a zone where the types of interactions are not known. Because the architecture and the width of the crossing zone are unclear, the transport and magnetic phenomena are difficult to model in this zone. However, this region is to avoid in order to get better transport results, as it brings an additional resistance to the GMR. This is why low porosity samples are preferred to high porosity ones. Figure 1.43(c) shows homogeneous crossed NWs. Out of the crossing zone, the NWs present monodomain architectures. Previous studies showed that below a certain diameter, NWs are only made of monodomain materials. Crossing zones form intersections between monodomain material of different NWs. The phenomenon arising at this position of the wires is not known; the creation of domain walls is possible and as a consequence could have an impact on the hysteresis loop.

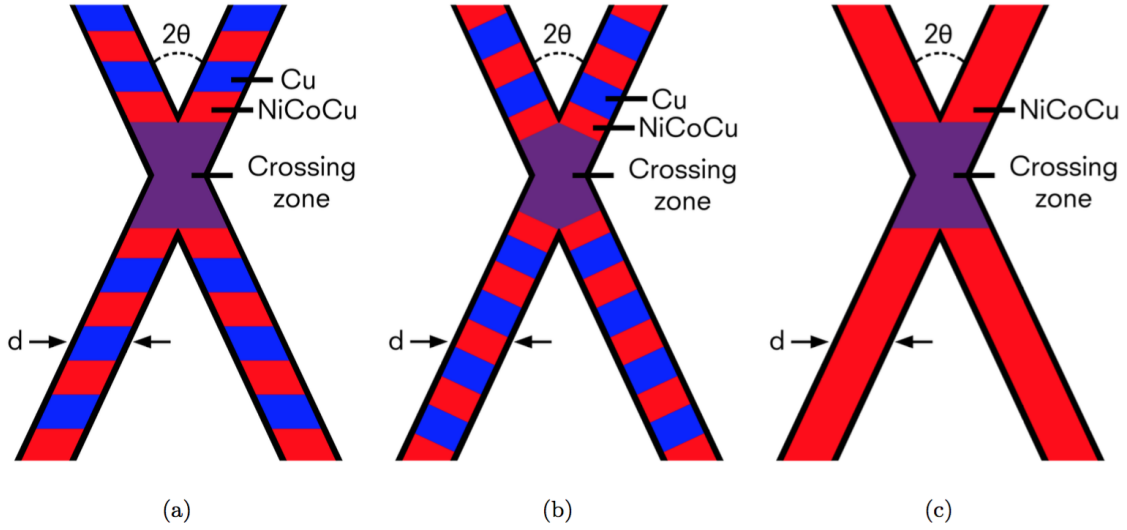


FIGURE 1.43: Schematic illustration of cross-section of two nanowires. (a) and (b) are possible configurations of multilayers inside the crossed nanowires (c) shows homogeneous NWs. [44]

### Changes in magnetic properties

In general, hysteresis loops in CNWs show less marked squareness resulting from their non-parallel orientation and the presence of interconnections. Figure 1.44 presents two hysteresis loops one made of parallel NWs (a) and another of crossed NWs (b). A significant reduction of anisotropy is observed in the second figure, showing a more isotropic behaviour. This is a consequence that the applied field lays at a certain angle with respect to the NWs axes. In the OOP direction, the NWs axis are oriented $\pm\alpha$ from the field direction (angle between the NW axis and the normal to the PC membrane); while in the IP direction $\pm(90° - \alpha)$. The shape anisotropy will be reduced because the observed demagnetising fields in the IP and OOP direction are situated at angles in between parallel and perpendicular directions observed in parallel NWs. As illustrated in figure 1.44, the saturation magnetisation in the IP direction is faster attained for crossed NWs than parallel NWs. On the opposite, the saturation magnetisation in the OOP direction is attained at higher field values for crossed NWs than parallel NWs. These effects indicates an increase of the demagnetising field in the OOP direction and a decrease of the demagnetising field in the IP direction [1].

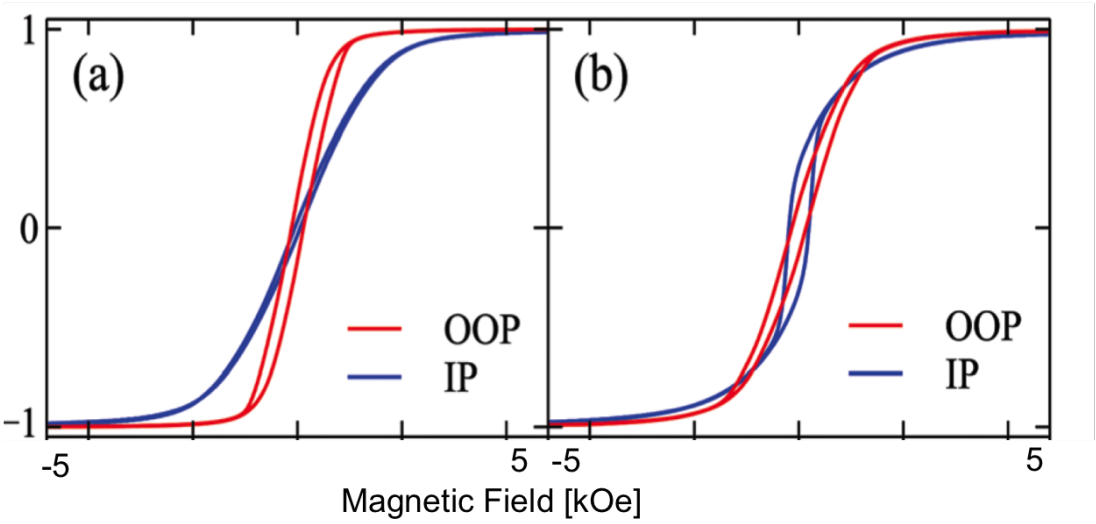


FIGURE 1.44: Comparison between hysteresis loops of (a) a parallel array of NW and (b) a crossed network of NW. [1]

### Changes in magnetotransport properties

**AMR** AMR curves of CNWs present different shapes than parallel NW array. As the magnetic field for the OOP and IP directions lays somewhere in between the $\parallel$ and $\perp$ direction, the change in resistance will not be exactly the same: the anisotropy angles are different. Figure 1.45 shows a MR curve of an HCNW. The maximum resistance corresponds to the zero applied magnetic field. Then when the magnetic field inceases, the resistance decreases. The measurement in the IP direction show a larger decrease of resistance than the OOP direction. When applying a magnetic field, the resistance will show a larger decrease in the IP direction as the magnetic field lays almost perpendicular to the current. The resistance measurements correspond to the average magnetoresistive value resulting from the contributions of all the NWs with different orientations with respect to the applied field directions. Therefore, the resistance states at saturation $\rho_{IP,sat}$ and $\rho_{OOP,sat}$ in both IP and OOP directions reach values which are intermediate between $\rho_{\parallel}$ and $\rho_{\perp}$ (see figure 1.45).

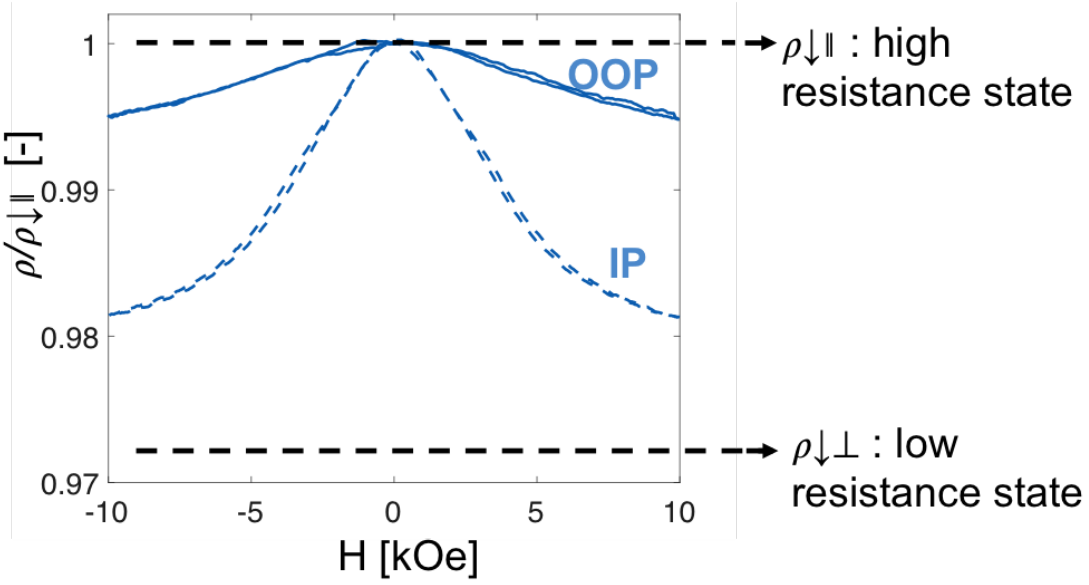


FIGURE 1.45: GMR for a parallel nanowire network. [8]

**GMR** The previous thesis, that investigated a template with reduced porosity, led to the discovery of IP GMR of 80% at 20K. The same sample at RT gave IP GMR of about 40%, showing the strong impact of temperature on the NiCo alloy. Moreover, the reduced amount of crossing zones influences a lot the GMR results, as the maximum value for 20% porosity was around 15% IP GMR. Figure 1.46 shows this impressive results. The maximum resistance is attained close to zero-field, and show the moment at which the spins have a perfect antiferromagnetic (or totally random) configuration. When the applied field increases, the magnetic moment become all parallel allowing higher conductivity. A small gap between the IP and OOP curves is observed. The upper-bound of GMR results are given by the IP-GMR measurement.

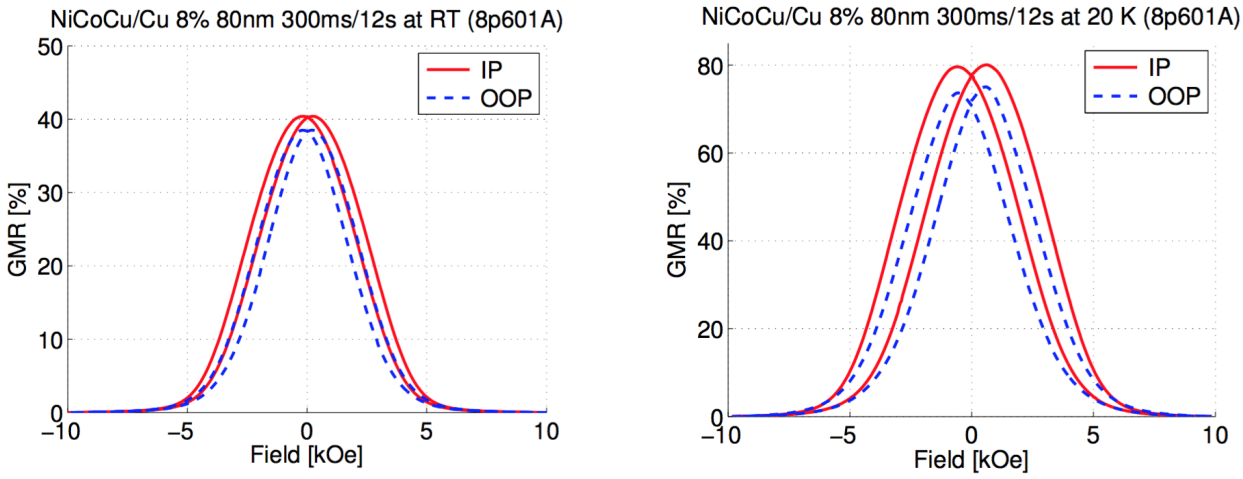


(a) T∼ 300K

(b) T∼ $20K$

FIGURE 1.46: GMR curves of a NiCo/Cu sample made on a 80nm 8% template.

**Δ MR** As observed in the previous figure, GMR curves often present a difference between the IP-GMR results and OOP-GMR results. This is because an effect due to the AMR is present when

doing GMR measurements. This effect of AMR on the GMR curves is called $\Delta MR$ and is shown on figure 1.47.

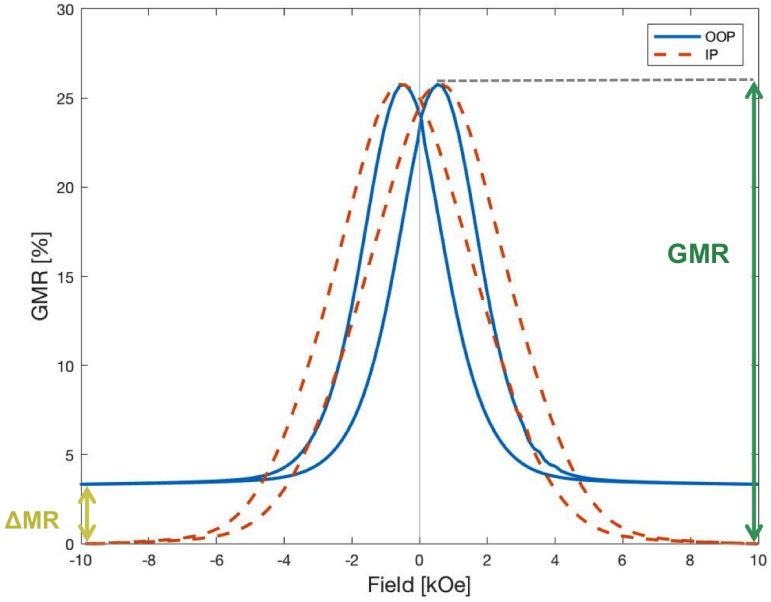


FIGURE 1.47: Illustration of the ΔMR on a GMR curve.

The GMR is calculated by doing the difference between the resistance in perfect antiparallel alignment ($R_{max}$) and the resistance in perfect parallel alignment, all divided by the resistance in perfect parallel alignment. If only GMR effect was present, the resistance at saturation would be the same in the IP and OOP direction. However, as shown before, the resistance at saturation in the IP direction ($R_{IP}$) is often lower; presenting higher GMR results. As consequence the GMR is defined as:

$$GMR = \frac{R_{max} - R_{IP}}{R_{IP}} \cdot 100 \quad [\,\%\,]$$

To verify that the measured effect is principally coming from the GMR, and not an artefact mixing two effects, the magnitude of the AMR should be evaluated. This is done by calculating ΔMR. This value is independent of the GMR effect; only depends on the magnetisation at saturation in both direction, $R_{IP}$ and $R_{OOP}$ :

$$\Delta MR = \frac{R_{OOP} - R_{IP}}{R_{OOP}} \cdot 100 \quad [\,\%\,]$$

To be sure, the GMR measurement makes sense, $GMR >> \Delta MR$ must be verified.

# Chapter 2

# Synthesis and characterisation of interconnected multilayer nanowire networks

In this chapter, the template-assisted electro-deposition technique used in this work is described. More information about the different electrolytes that were used is provided. Finally, the last part of this chapter discusses the different characterisation techniques necessary to analyse the results.

## 2.1 Synthesis of a 3D network

**Template**

Track etched polycarbonate (PC) membranes with crossed nanochannels were used as nanoporous host material for the growth of multilayered nanowires. The process to obtain the track etched membranes has been described in section 1.2.1. The templates that were used were subjected to a first irradiation step over a wide angular range from $-25°$ to $+25°$ with respect to the normal axis of the PC surface, illustrated in figure 2.1(a). Next, as shown in figure 2.1(b), for the second irradiation step, the film was rotated in the plane by $90°$ and re-exposed to the same angular variable irradiation flux to form finally a complex 3D nanochannel network. The standard angle deviation of the template is estimated to be around $5°$ and the diameter dispersion around $5\%$. A gold (Au) or copper (Cu) film serving as cathode is evaporated on one side of the membrane. The templates have a thickness of 22 $\mu m$ and are supplied by the company $it4ip$, located in Louvain-la-Neuve.

The types of templates that were used in these thesis are:

- A "low porosity template" made of a gold cathode, and a PC membrane with pores of 80 nm diameter and a volumetric porosity of $3\%$ of nanowires (left template in figure 2.2).
- A "high porosity template" made of a copper cathode, and a PC membrane with pores of 40 nm diameter and a volumetric porosity of $20\%$ (right template in figure 2.2).

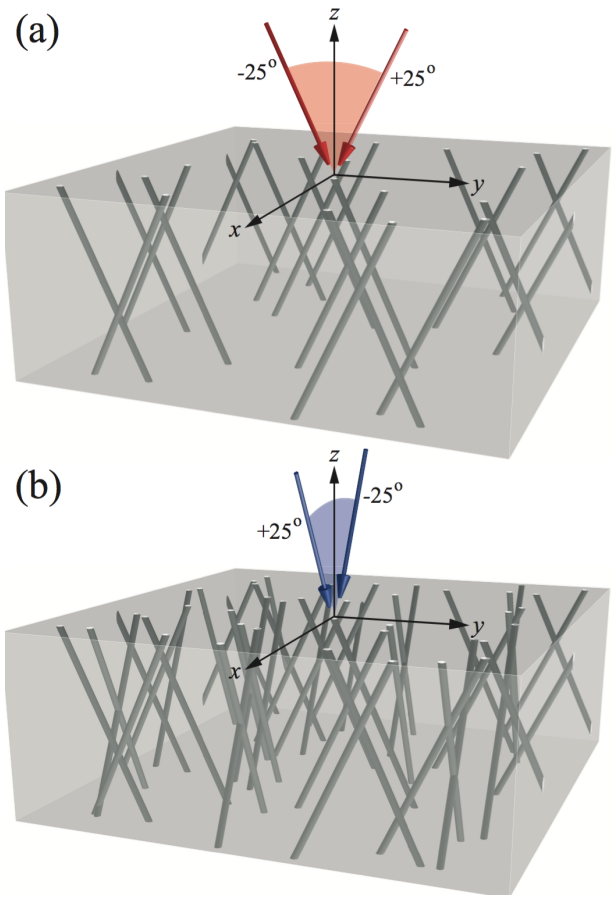


FIGURE 2.1: Schematics of the track etching process (a) for the first irradiation step under an angular range of $\pm 25°$ relative to the out-of-plane direction and (b) for the second irradiation step after in-plane PC membrane rotation by $90°$ and again under the same angular range relative to the OOP direction.

FIGURE 2.2: Left template made of gold cathode. Right template made of Copper cathode. The template is cut in circle shape of 7 mm diameter.

The metallic cathode thickness must be large enough to completely cover the nanopores, but should be thin enough to be easily removed locally. A 150 nm thick cathode is sufficient for a 40 nm pore diameter template. To improve the adhesion of the cathode on the template, which is required for the electrodeposition, a 10 nm Cr layer is placed between the cathode and the template. Depending

on the number of measurements needed, the templates are cut in rectangles of 2 cm $\times$ 0.5 cm or in small circles of 7 mm of diameter.

**Electrodeposition**

The membrane sample is placed in a home-made Teflon cell. The electrodeposition is performed at room temperature (RT). Ferromagnetic Co and Ni nanowires are electrodeposited in nanoporous membranes with diameter of 40 and 80 nm using a boric acid bath. Electrodeposited NiCoCu/Cu and CoCu/Cu multilayered nanowires are made from a single bath using a pulsed electrodeposition technique. The noble element (Cu) is kept in dilute concentration so that the rate of reduction of Cu is slow and limited by diffusion. The counter electrode used is made of Platinum (Pt) and the reference electrode is a Silver/Silver chloride (Ag/AgCl) electrode. The adjustable parameters for the electrodeposition are the applied potential and the deposition time.

Different electrolytes were used during these thesis. The electrolytes are prepared from solid metal sulphate hydroxides diluted in water to obtain a sulphate bath with the following components: $H_3BO_3$, $NiSO_4 \cdot 6H_2O$, $CoSO_4 \cdot 7H_2O$ and $CuSO_4 \cdot 5H_2O$. The role of the first component, $H_3BO_3$, is to increase the solubility. Table 2.1 gives a summary of the different compositions of electrolytes that were used. First, based on the previous work [44], an electrolyte with $2.3M$ of Ni was fabricated. This solution was too concentrated and the results were not good. Indeed, as the electrolytes were close to saturation in terms of Ni concentration, they were not completely stable. The solution presented precipitates, blocking pores inside the template. This prevented a good and homogeneous deposition over the entire sample area. Moreover, precipitation changes the relative concentrations, which is inadequate for the credibility of the results. For this reason, the concentration was decreased to 1M of Ni, 0.2M of Co and 0.0075M of Cu in a second step. Based on the previous research [44], the desired composition inside the ferromagnetic layers was a ratio of $50\% - 50\%$ of Ni-Co. This is why as a third step, measurements were made by Scanning Electron Microscopy (SEM) on electrolytes with slight variation in Co concentration to verify the composition.

Then, to explore the case of $25\%$ Ni and $75\%$ Co, a new electrolyte of composition NiCoCu 1M-0.4M-7.5mM was developed. We can notice that each time, the Ni concentration is larger than the Co concentration. This is linked to the fact that the difference in the deposition rates of the two metals needs to be balanced out. Indeed, Ni deposits at more negative potential than Co, as showed in table 1.9. Finally, an electrolyte without Ni was developed, creating multilayers with only CoCu/Cu. Two types of electrolytes were made for this composition, one with pH4 and one with pH2.

In table 2.1, labels are given for the different electrolytes to simplify the notation. The first electrolyte is labelled Sol_NiCo_2.3MNi_0.4MCo_0.15MCu and is composed of 2.3M Ni, 0.4M Co and 0.15M Cu. Then, in the following electrolytes, the Ni and Cu concentrations are kept constant at 1M and 0.0075M respectively, so only the Co concentration is specified in the label. For the two last electrolytes, no Ni is present, while the concentrations of Co and Cu are still 1M and 0.0075M. These last electrolytes only differ with the pH, which is hence specified in the label.

| Label | Ni [M] | Co [M] | Cu [M] | pH |
|---|---|---|---|---|
| Sol_NiCoCu_2.3MNi_0.4MCo_15mMCu | 2.3 | 0.4 | 0.015 | 2 |
| Sol_NiCoCu_0.2M | 1 | 0.2 | 0.0075 | 2 |
| Sol_NiCoCu_0.18M | 1 | 0.18 | 0.0075 | 2 |
| Sol_NiCoCu_0.17M | 1 | 0.17 | 0.0075 | 2 |
| Sol_NiCoCu_0.15M | 1 | 0.15 | 0.0075 | 2 |
| Sol_NiCoCu_1.5MNi_0.26MCo_15mMCu | 1.5 | 0.26 | 0.015 | 2 |
| Sol_NiCoCu_0.4M | 1 | 0.4 | 0.0075 | 2 |
| Sol_CoCu_pH2 | 0 | 1 | 0.0075 | 2 |
| Sol_CoCu_pH4 | 0 | 1 | 0.0075 | 4 |

TABLE 2.1: Composition of the different electrolytes that were used.

The pH of the electrolytes is tuned by adding $H_2SO_4$ in order to bring the solution to a pH between 2 and 2.1. This pH favours an fcc crystal structure for the NiCo ferromagnetic layers.

**Pulse potentials**

The pulse potentials $V_F$ and $V_N$ were chosen based on earlier studies and on the results of the previous thesis [44]. The NiCoCu layer deposition time gives good results at -1V, the CoCu layer at -0.95V while the Cu layer gives the best results at -0.4V. This choice is crucial because when the Cu potential is too low, a risk of dissolution arises and when the Cu potential is too high, Ni and Co could deposit in the non-magnetic layer; on the opposite, a low potential for the NiCo is not good because less NiCo would deposit in the magnetic layer with respect to Cu; a high potential would favour impurities inside the magnetic layer.

Because all three metals are deposited at -1V (in the case of NiCoCu) and at -0.95V (in the case of CoCu), the Cu concentration needs to be kept very low to reduce the deposition of Cu in the magnetic layer. This process allows to limit the Cu concentration inside the magnetic layer to only a few percent. Due to this very low concentration, the deposition rate of Cu at -0.4V is very slow and the pulses require a longer deposition time. The choice of the deposition potential is crucial as not only the type of material will be determined but also structural phase can depend on the pH as described in 1.2.1.

**Deposition time**

The deposition time allows the sample to become more or less magnetically isotropic, resulting in a certain thickness. To optimise the deposition time, a systematic approach was used, by changing one parameter at a time. First, the deposition time of the magnetic layer was optimised, then the one of the Cu layer. This process was repeated for each new electrolyte. Each deposition was performed by cycles of pulses of $V_F$ and $V_N$, where each cycle deposited one bilayer consisting of a Cu layer followed by a NiCoCu or CoCu layer. On average, 600 bilayers were made per nanowires. By using varying deposition times, samples of different layer thicknesses were obtained and analysed.

The electrodepositions are performed under time and pulse potential control. The computer calculates the deposition current. The deposition could not be made under control of the deposited charge, as has been done in earlier studies. Since the deposition currents for the NiCoCu and Cu are of different orders of magnitude, and the scale can not adapt itself between the two orders of magnitude, the current measured by the machine is around 4mA for the ferromagnetic layer while the measured Cu current is slightly negative. This can of course not be correct. Indeed, it would result in dissolution of the metal inside the pores. However, the GMR effect of these

samples proved that the Cu layer must have been deposited; it can be conclude that the values of the measured deposition currents can not be trusted.

**Measurement of the layer thickness**

When the wires emerge from the surface (overfilling), a sudden increase of the plating current appears. These phenomena can be used to determine the layer thickness. By taking the time at which the current starts to increase ($t_{ov}$), and knowing the deposition time of each bilayer composed of a ferromagnetic layer and a non-magnetic layer ($t_f + t_{nm}$), the number of bilayers is given by:

$$n_{bl} = \frac{t_{ov}}{t_f + t_{nm}}$$

The membrane thickness is 20 $\mu m$ but one needs to take into account the slope of the nanowires which is 25°. As a result, the total length of one nanowire is $22\ \mu m/\cos(25°) = 24.27\ \mu m$. Finally, dividing the length of one nanowire by the number of cycles gives the average thickness of one bilayer:

$$t_{bl} = \frac{24.27\ \mu m}{n_{bl}}$$

On average, the objective is to have a bilayer thickness ranging from 15 to 20 $nm$.

## 2.2 Composition and morphology characterisation - SEM

Using SEM, the average chemical composition of our samples can be determined. Moreover, SEM images allows to visualise the nanowires and their structure. Image 2.3 and 2.4 illustrate nanowires fabricate in a template with a porosity of 20%. The larger density is clearly visible when it is compared with the images below: figure 2.5 and 2.6. Indeed this two last images present nanowires with a porosity of 3%. On the image 2.5, the larger diameter of the nanowires can be observed. Due to the lower density of the 3% porosity template, the wires crosses each other less often and as a consequence are less "sefl-sustainable". This effect can be seen on the image 2.6: the wires seem to fall on each others.

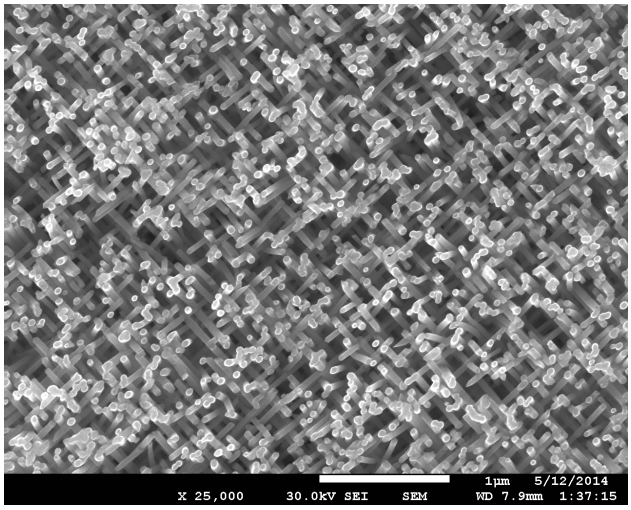


FIGURE 2.3: SEM 40 nm 20 %.

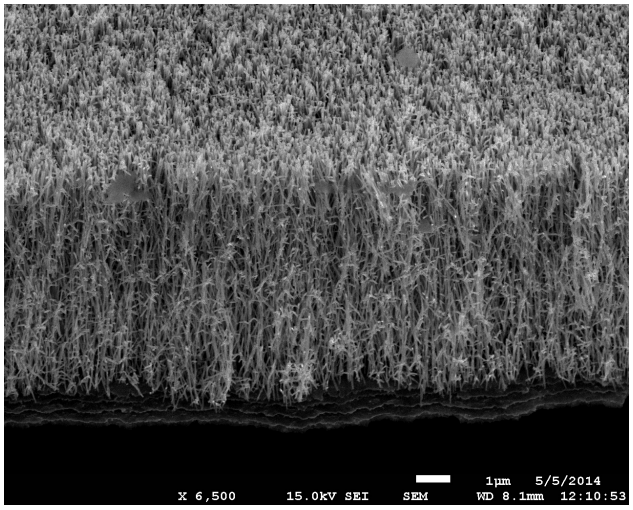


FIGURE 2.4: SEM 40 nm 20 %

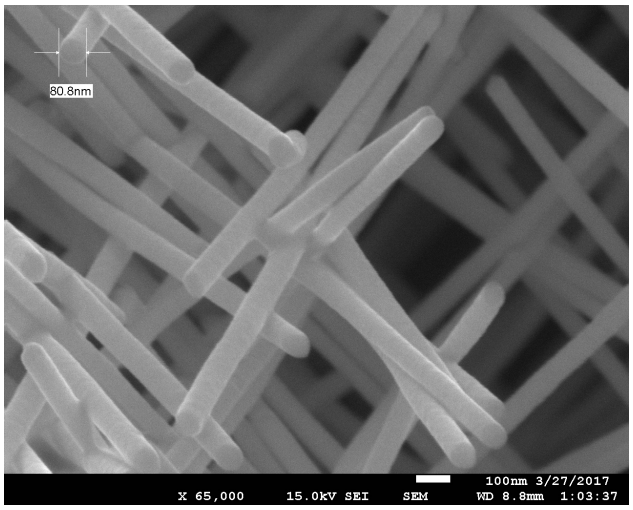


FIGURE 2.5: SEM 80 nm 3 %.

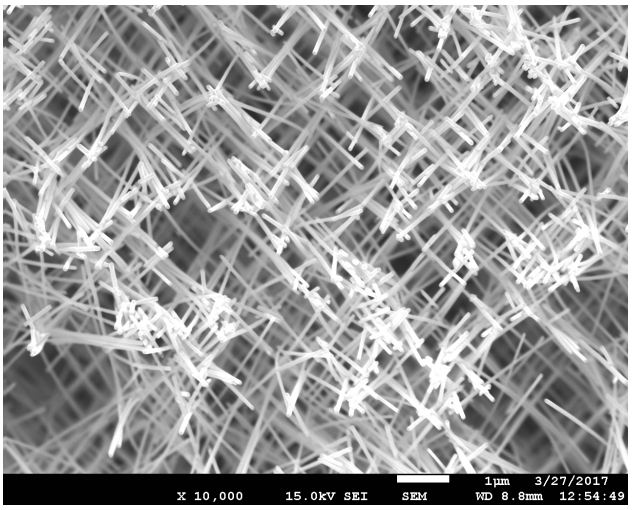


FIGURE 2.6: SEM 80 nm 3 %

The used machine is a field-emission scanning electron microscope (FE-SEM): a JEOL FEG SEM 7600F equipped with an energy-dispersive X-ray (EDX) spectroscopy analysis system, having a resolution $< 129$ eV. The machine is represented in figure 2.7. The microscope is composed of a series of lenses within a vacuum chamber. These lenses direct the electrons towards the specimen in order to maximize the efficiency. The vacuum chamber is necessary to avoid electrons interaction with particles.

FIGURE 2.7: Image of JEOL FEG SEM.

When a specimen is hit with the incident electron beam, it emits X-rays and three kinds of electrons: primary backscattered electrons, secondary electrons and Auger electrons. A schematic of the process is given in figure 2.8. An electron recorder picks up the rebounding electrons and records their imprint. This information is translated onto as screen which allows 3D images to be represented clearly [46].

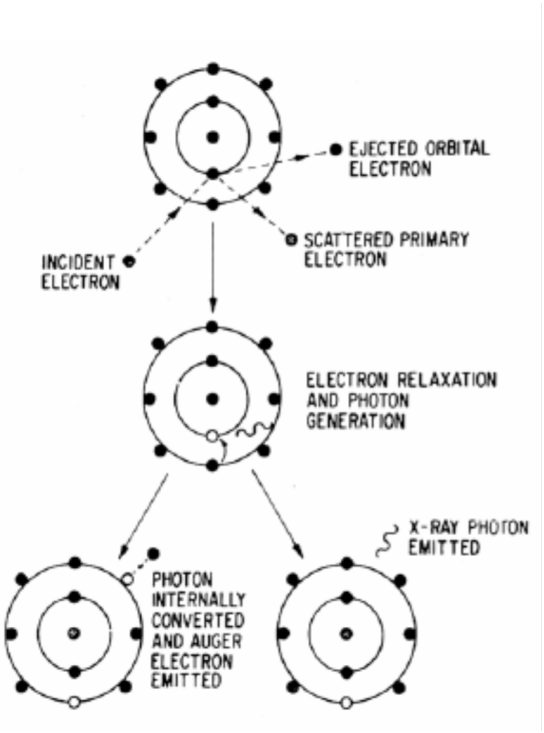


FIGURE 2.8: Incident electron targeting electron shell forming Auger electron or X-ray. [25]

To obtain a localized chemical analysis, EDX analyses the X-ray spectrum emitted by the sample bombarded by the incident electron beam. An image of X-ray spectrum is showed in figure 2.9. All elements between atomic numbers 4 (Be) and 92 (U) are in principle detectable. Quantitative analysis (determination each element's concentration) entails measuring line intensities for each element in the sample. This was done using the integrated Analysis Station software according to a two-step analysis. First, the subtraction of the bremsstrahlung; second, the quantification of the area under each atomic peak is done with the ZAF method. The crystalline material may be identified by its diffraction spectrum, by comparing the diffraction angles corresponding to peaks in the spectrum and their relative intensities with a diffraction standard (for example, the JCPDS file).

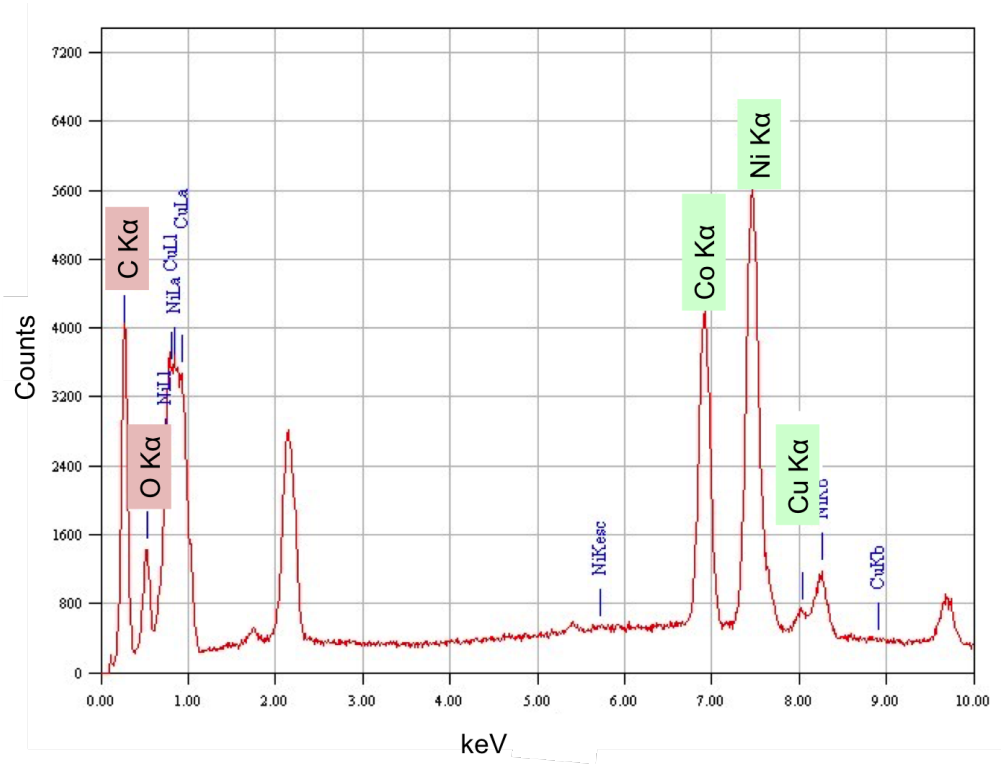


FIGURE 2.9: X-ray spectrum for a sample of HCNWs made of Sol_NiCoCu_0.2M.

Classically, a simple comparison of the intensities with respect to a reference sample of known composition would give as first approximation ($*$ and $st$ indicate sample and standard, respectively):

$$\frac{C^*}{C_{st}} = \frac{I^*}{I_{st}}$$

The ZAF method takes into account that the intensity of the peaks related to one element can be modified due to the presence of another element in the sample. Three corrections are made: atomic number correction ($Z^*$), absorption correction ($A^*$) and fluorescence correction ($F^*$).

$$\frac{C^*}{C_{st}} = \frac{F^*}{F_{st}} \frac{I^*}{I_{st}} \quad \text{with} \quad F^* = FZ^* \cdot FA^* \cdot FF*$$

The atomic number correction accounts for the modification of the effective incident beam 'activating' the emission of photons with characteristic energies due to elastic and inelastic scattering of the incident electron beam. The absorption correction considers the fact that part of the created photons are absorbed along their path to the surface. Finally, some emissions occur not due to the incident electrons but due to the fluorescence activated by X-rays emitted by the matrix; this is the fluorescence correction.

The FE-SEM measurements were performed with electrons accelerated to 15 keV with a working distance of 7-8 mm. The EDX measurements were carried out with a chemical spectrum acquisition time of 100 seconds with a probe current of 1nA, at different spots on each sample to reveal possible heterogeneities in the composition of the sample. Figure 2.10 illustrates the electron-matter interaction volume. One can see that the Auger electrons are coming from 1 nm deep out of the surface, the secondary electrons from 5 to 50 nm deep, the backscattered electrons from 300 nm and the X-ray from approximately 1 $\mu m$. This means that the resolution will depend on the type of signal analysed.

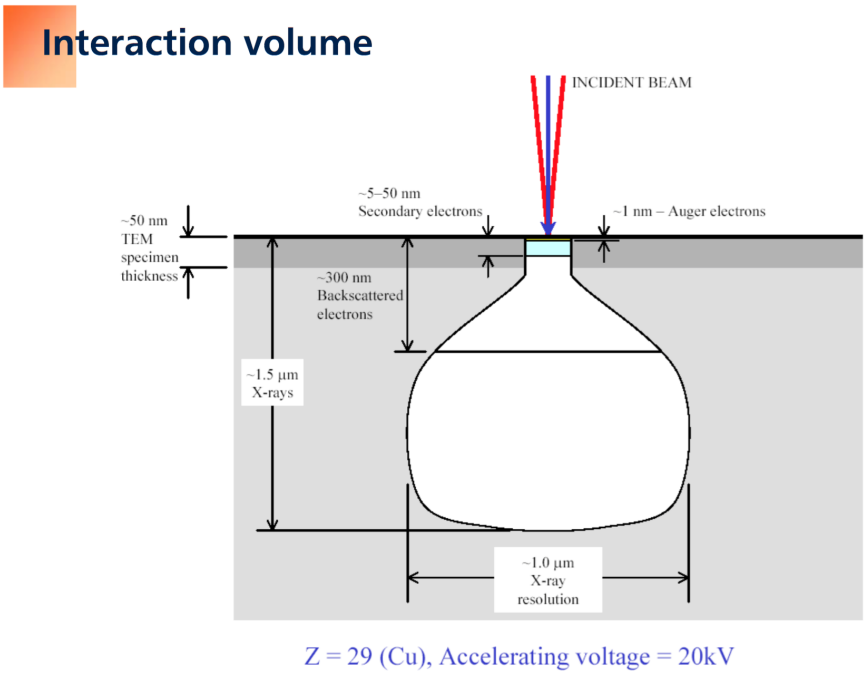


FIGURE 2.10: Interaction volume. [25]

In the SEM, homogeneous nanowires were analysed to estimate the average composition of the magnetic layer. The $K_\alpha$ peak in figure 2.9 is the emission line that results from the transitions of an electron from a $2p$ orbital of the second or 'L' shell to the innermost 'K' shell; the $K_\beta$ peak results from the transition of an electron from a $3p$ orbital or 'M' shell to the 'K' shell. The fractions of Nickel and Cobalt are evaluated based on their $K_\alpha$ peaks. As can be seen in figure 2.9, other elements may appear on the spectra, usually Carbon, Oxygen, Copper or etchant solution residues. Carbon and oxygen are residues of the polycarbonate sample but can also come from organic contamination from dirt of our fingers, for example. There are always some traces of C, O and H in the samples because they are not totally clean. The element H is not visible on the spectrum, because its atomic number is 1; it is therefore included in the background. As explained previously, only elements with large enough atomic numbers (4→92) are visible. Also, the $K_\beta$ peak of Co is located spectrally near the $K_\alpha$ peak of Ni. As a consequence, the deconvolution of the peaks is not very accurate and the atomic fraction of Ni may be overestimated. This effect becomes more pronounced as the amount of Co increases.

### Sample preparation for SEM

The process will only work if the sample is properly prepared. First, the template must be removed. Indeed, in non-conducting samples, a charging effect occurs if the electrons remain on the sample. As a consequence, the sample becomes electrically charged. To avoid this effect, all the non-conductive material need to be removed, including the polycarbonate template. To remove the cathode, $KI_2$ is used and to remove the PC membrane the sample is put in a dichloromethane bath. Due to the fact that the sample is an interconnected nanowire network, it is self-supporting and can be moved easily. The sample is then carefully removed from the bath and bonded on a piece of Si-glass sample holder using to an adhesive carbon fibre film.

## 2.3 Magnetic characterisation - AGM

The magnetic measurements were made on a MicroMag 2900 alternating gradient field magnetometer (AGFM) from Princeton Measurement Corporation. A picture of the machine is given in figure 2.11. This instrument is a powerful alternating gradient magnetometer system used to measure the magnetic properties of various materials. The system offers an extremely high sensitivity (10 nemu rms) and fast measurements (10 ms per point). Because of its high sensitivity, the AGM system is particularly useful for research involving materials with very low magnetic moments. The instrument accommodates solid and ultra thin film samples with a sample holder embedded within transducer probes. The system includes two polyimide probes: one parallel for the 'in-plane' measurements, and another perpendicular for the 'out-of-plane' measurements.

FIGURE 2.11: MicroMag™ 2900 Series AGM System.

First, the instrument was calibrated using a spherical Fe sample with a known saturation magnetisation of 76.2 memu and a well-known hysteresis curve. Then, a small piece of the sample was cut and placed on a glass support plate on the sample holder and loaded between the two magnets on the instrument (figure 2.12(1)). The sample is magnetised by a uniform field created by the electromagnets. This causes the sample to generate its own magnetic field (figure 2.12(2)). Gradient coils produce an alternating excitation field on the sample (figure 2.12(3)). The interaction between the sample's own field and the excitation field displaces the sample alternatively left and right proportionally to its magnetic moment. This resulting deflection of the cantilever rod is measured by the piezoelectric sensor attached to the sample holder in the form of an AC voltage (figure 2.12(3)). By operating at or near the mechanical resonance frequency of the cantilever, the output signal is greatly amplified. The measurement is recorded and the data is stored for later analysis [38].The measurement is done at room temperature. The maximum applied field is $|H_{max}| = 14\ kOe$.

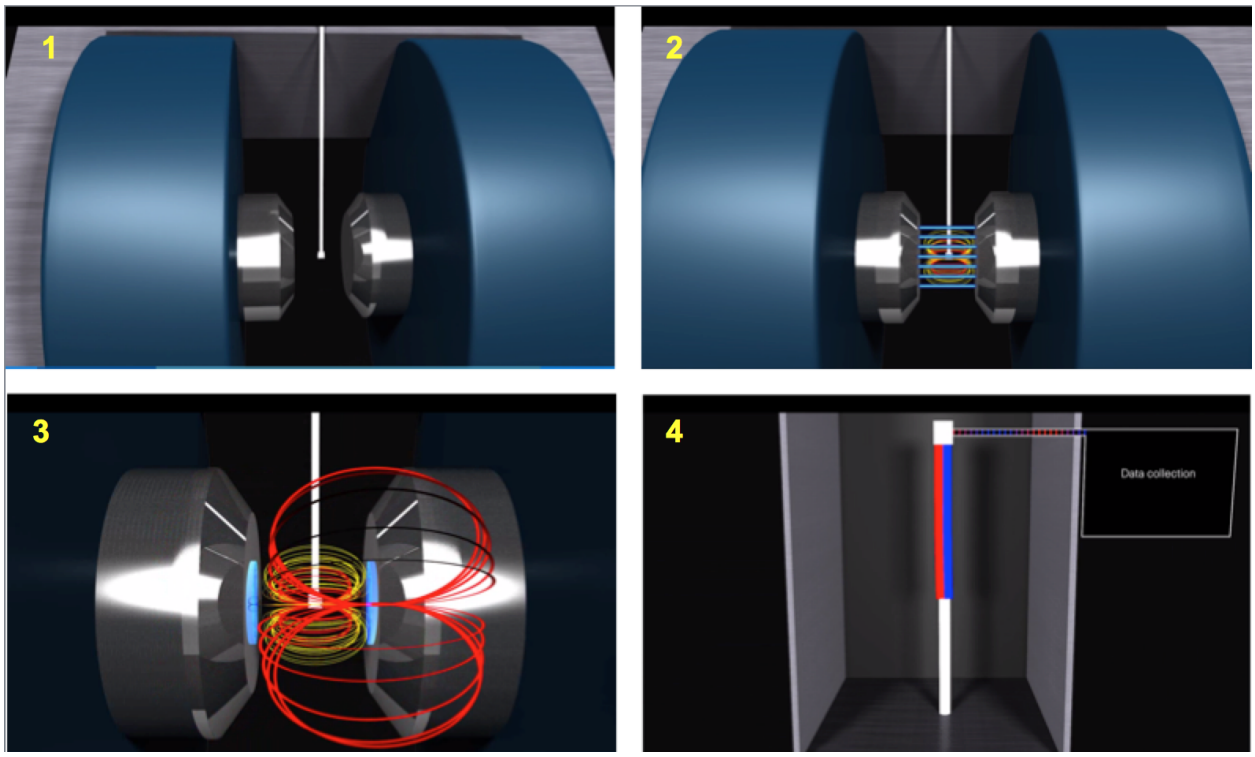


FIGURE 2.12: Working principle of the AGM. [**_pmc_2018**]

For each measurement, the static magnetic field was changed from zero to $+H_{max}$, then from $+H_{max}$ to $-H_{max}$, and finally from $-H_{max}$ to $+H_{max}$. The increment used step to obtain the hysteresis loop, was 50 Oe for the calibration and 30 Oe for the samples. From the resulting curves, the remanent magnetisation and saturation magnetisation can be obtained if the maximum applied field is sufficient to saturate the magnetisation. To compare all the samples, the curves were normalised by $M_S$ which is taken as the magnetisation at 14 kOe applied field, $M_{H=14\ kOe}$ because the magnetic moment depends on the sample size, which may vary between samples. The coercive field and the remanent magnetization are provided, as well as the general shape of the hysteresis curve in IP and OOP direction. Neither the cathode nor the PC-template were removed for the measurements. Their paramagnetic and diamagnetic contributions are considered small compared to the ferromagnetic contributions and are removed thanks to an adjustment done by the MicroMag software.

The AGM results, which graphically represent the magnetisation reversal, are interpreted for qualitative conclusions. Physically meaningful hypotheses can be made, such as: teh intensity and spatial distribution of the interaction field at saturation, the coercivity distribution of individual nanowires, a quantitative evaluation of the overall magnetic anisotropy or insight about the magnetisation reversal mechanism.

The force along $x$ and $y$ resulting from the interaction of the gradient coils and the magnetic moment of the sample $m_x$ is

$$F_x = m_x \frac{dh_x}{dx} \quad \text{and} \quad F_y = m_x \frac{dh_x}{dy}$$

In these two cases, the magnetic moment is controled by changing $H_x$. The configuration can be seen in figure 2.13.

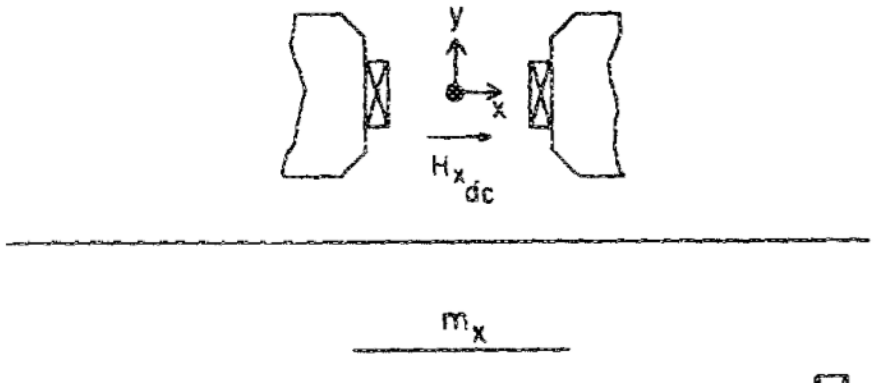


FIGURE 2.13: Gradient coil arrangement. The direction of the applied field and the magnetic moment $H_X$ is visible as well as the x and y directions. [18]

## 2.4 Magnetotransport characterisation - AMR and GMR

To characterise the magnetotransport properties of the samples, electrical measurements under a varying magnetic field are made. The apparatus used were an electromagnet to create the magnetic field (Model 643 electromagnet from Lake Shore) and a probe to support the sample (Lake Shore Hall probe); they were connected to an amplifier to control the current through the sample (7265 DSP Lock-in amplifier from Signal Recovery), a multimetre to measure the drop of voltage across the sample (Keithley 2000 Multimeter) and a computer that gives the resistance of the sample as a function the applied field.

The schematic of the circuit is represented in figure 2.14. The current is injected from the cathode of one of the unetched edges of the sample, goes through the 3D CNWs and, then, goes out at the other unetched edge of the sample. The sample is placed in a metallic holder, at the end of a cane that allows to rotate the sample within the magnetic field. An alternating current is used to increase the signal/noise ratio and remove the effects produced by $\delta B/\delta t$. This current is injected using an alternating voltage supply and a resistance, $R_{int}$. The input power was kept below 0.1 $\mu$W to avoid self-heating.

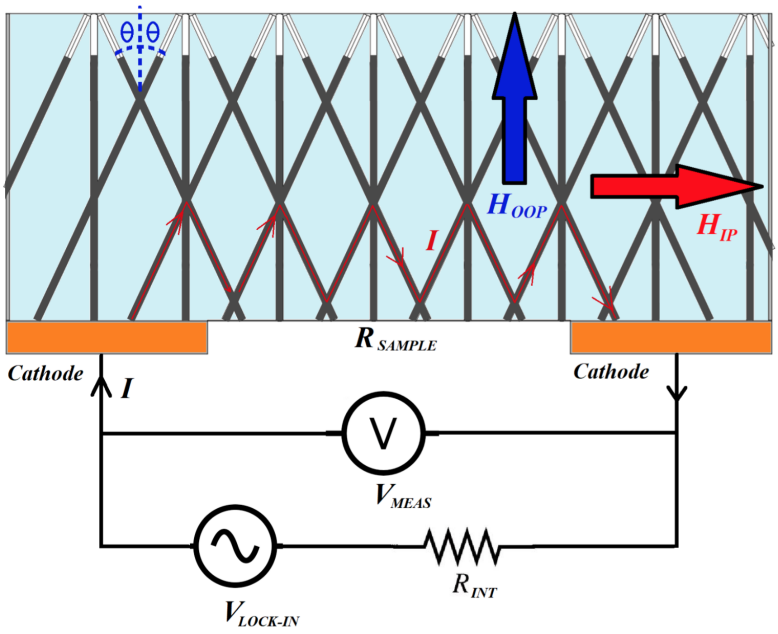


FIGURE 2.14: Circuit for the magnetotransport measurements. The direction of the applied field **H** in the IP and OOP configuration are indicated by arrows. The alternating current **I** is injected in the lock-in through the remaining cathodes, and a potential current path through the sample is depicted by red arrows. A voltmeter is connected in parallel to measure the potential drop, V, across the sample corresponding to $R_{sample}$. The internal resistance corresponds to $R_{int}$. [44]

Different factors contribute to the resistance of the crossed nanowires array. One has to distinguish the global resistance of the sample from every local contribution. In figure 2.15, the resistances that appear when measuring the GMR of our sample are illustrated.

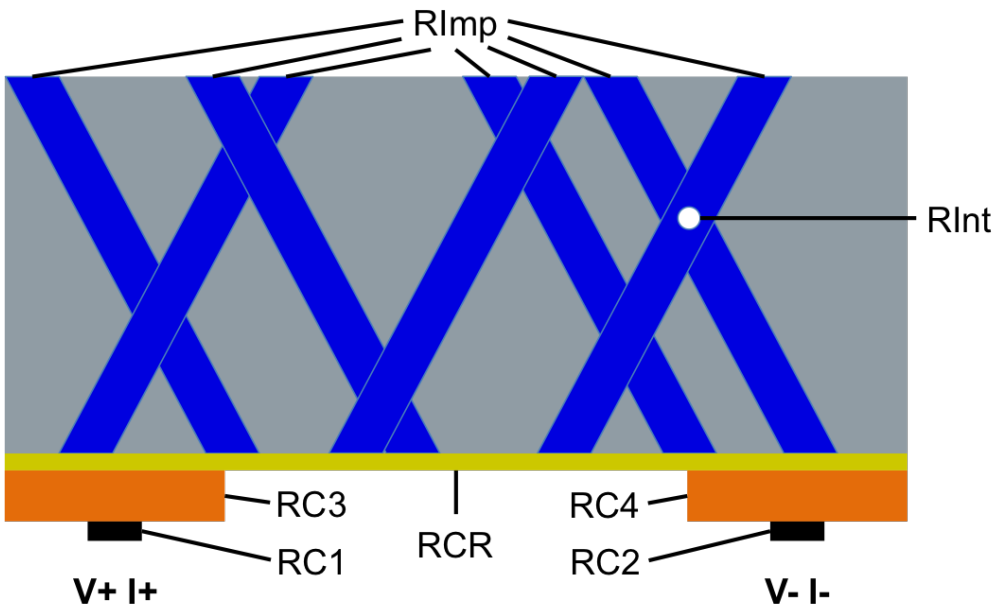


FIGURE 2.15: Different resistances appear when measuring GMR: a resistance due to impurities ($R_{Imp}$), the wires intersection ($R_{Int}$), the residual cathode ($R_{CR}$), the contact between the Cu wires and the cathode ($R_{C1}$ and $R_{C2}$) and the contact between the cathode and the nanowires ($R_{C3}$ and $R_{C4}$).

The resistances that appear in series ($R_1$) and in parallel ($R_2$) can be defined as:

$$R_1 = \overbrace{R_{C1} + R_{C2} + R_{C3} + R_{C4} + R_{Imp} + R_{Int}}^{R_C} + R_{GMR} \quad ; \quad R_2 = R_{CR}$$

The total conductance is then:

$$C_{tot} = \overbrace{\frac{1}{R_1} + \frac{1}{R_2}}^{1/R_{tot}}$$

To be able to measure the GMR properly, this condition must be fulfill:

$$\begin{cases} R_{CR} >> R_{GMR} \\ R_C << R_{GMR} \end{cases}$$

The $R_{C1,2,3,4}$ really depend on the system's manufacturing. To get better GMR results, $R_{Int}$ can be minimized by decreasing the number of intersections and, as a consequence, decreasing the porosity. Another way to improve the GMR results is to decrease the temperature; $R_{Imp}$ then decreases. The spin diffusion length increases at low temperature and the impurities do not form obstacles anymore to the spin diffusion. Both homogeneous and multilayer CNWs were analysed in the low and high porosity templates, as well as at room temperature (RT) and low temperature (LT) to get information about these different contributions to the resistance.

The measurements were carried out in the CPP geometry. Most of the measurements were made at RT and normal pressure, but some of them were also made at LT ($T \sim 15K$). The external magnetic field varied between $H = -10$ kOe and $H = +10$ kOe while measuring the resistance of the sample, with increments of 50 Oe. Inside the chamber, the sample can be rotated by 90° with respect to the applied field to achieve IP and OOP measurements. To get accurate measurements, the internal resistance of the circuit $R_{int}$ must be at least 100 times higher than the resistance of the sample $R_{sample}$.

**Sample preparation**

A mechanical mask was used for selective local removal of the Cu or Au cathode. A Plassys MP500S machine with Ar plasma working at 80W, under 5 mTorr of Argon is used to remove the cathode. The etching time depends on the type of template as shown in table 2.2. If the cathode is not sufficiently removed, the sample is etched for 2 to 5 additional minutes. The template with a gold cathode and low density of nanowire is very sensitive; as a consequence, the etching has to be done several times, by short-time periods: after 10 min of etching, one must wait 10 min before proceeding again; then, the cathode is etched two more times for 5 min, with a 5 min break in-between. If the etching is insufficient, additional etching lasting 2 to 5 min can be done. The sample was cut in a small piece of about $3 \times 6$ mm.

| Cathode | $t_{cath}$ | Cr layer | ⌀ of the pores | Porosity | Etching time |
|---|---|---|---|---|---|
| Cu | 150 nm | 10 nm | 40 nm | 20 % | 26 min |
| Au | 400 nm | 80 nm | 3 nm | 3 % | $2 \times 10$ min + $2 \times 5$ min |

TABLE 2.2: Type of template with corresponding etching time.

Usually, the samples produced by electrodeposition are big enough to obtain two pieces for magnetotransport measurements and one for the AGM. The piece of sample is then mounted on a glass plate and covered with a home-made mask composed of two thin glass plate with a $\sim 1$ mm gap that is exposed to the plasma. The final configuration (see figure 2.16) allows the current to be

directly injected to the branched CNW structure from unetched sections of the cathode thanks to the high degree of electrical connectivity of the CNWs.

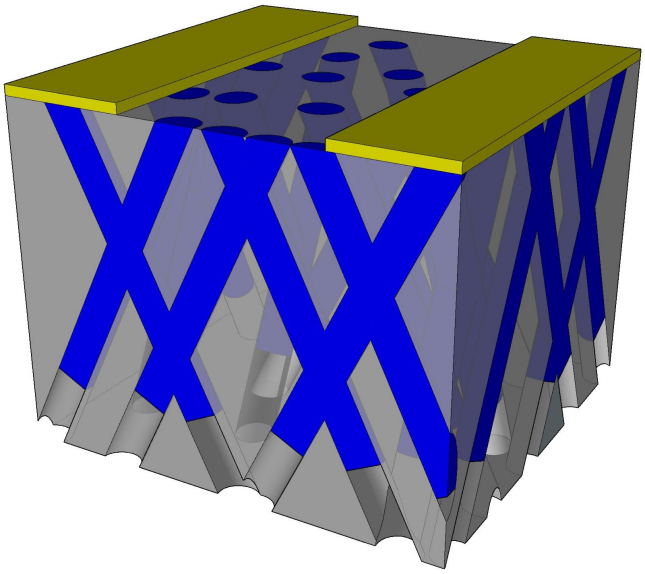

FIGURE 2.16: Sample with part of the cathode that is etched in order to inject the current through the array of nanowires.

The etched sample is then placed on a 14-node chip of $\sim$ 7 mm length, as shown in figure 2.17. Lacquer is spread on the chip to fix the sample. Two copper wires are welded between the cathode and the support to establish contact between the sample and the chip. Each of the wires is connected to two chip nodes. This configuration provides a pseudo four-point probe method setup, which allows current and voltage to be measured on the individual chip nodes.

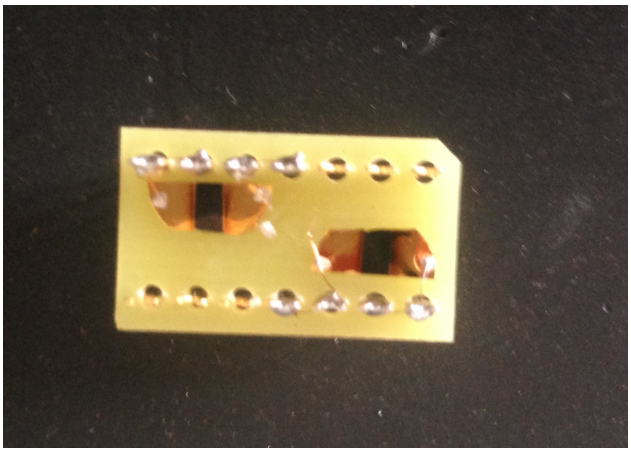

FIGURE 2.17: 14-node chip with samples on the nodes 1-2-3-4 and 11-12-13-14.

**Low temperature measurement**

Samples giving interesting GMR values were measured at low temperature. Indeed, in the LT range, the spin-mixing effects are negligible. Results suggest that the changes of CPP-MR with increasing

temperature are due mainly to increasing phonon-scattering. This results in an increase of the resistances of the magnetic and non-magnetic layers, and a decrease of the spin-diffusion length. This is explained at the end of section 1.1.3. Before each LT measurement, the sample-containing chamber is evacuated and purged with gaseous He several times to remove air and impurities. It is then filled with He to reach a pressure of $p \sim 2 - 3$ psi. The chamber is cooled to approximately 10 K using a CTI Cryogenics Helix Technology Corporation 8200 Compressor. The temperature is measured by two thermometers: one at a finger sensor inside the chamber, the other at the sample holder. The latter measures the temperature closest to the true temperature of the sample. Controlled heating of the chamber up to the intermediate temperatures is done by using a resistive heating element inside the chamber, that follows a PID temperature control monitored by the computer software.

# Chapter 3

# Results and discussion

This chapter is divided in 3 sections developing different ferromagnetic layer compositions. In order to improve the GMR effect, different parameters are optimised such as the ferromagnetic layer deposition time and the non-magnetic layer deposition time. The changes in magnetic properties with varying porosity and temperature are also observed. To proceed, one first parameter is optimised; then the best result is selected and fixed, and another parameter is optimised.

This master thesis is an "experimental" thesis, which implies imperfect results. Measurement inaccuracies (due to noise or other factors) can provide imprecisions, which can sometimes be difficult to interpret. As explained in section 2.4 (page 56), different resistances can produce misunderstandings when interpreting the GMR results.

## 3.1 $Ni_{50}Co_{50}$/Cu multilayer crossed nanowire networks

This section first provides a description of the different steps to get a ratio of about $50\%$ of Ni and $50\%$ of Co inside the ferromagnetic layer. Different electrolytes are made. One electrolyte presenting the most adapted properties is selected and optimised (ferromagnetic layer deposition time and Cu layer deposition time) on the high porosity template. The best result of this optimisation is reported on the low porosity template and measured at low temperature. The properties of the high porosity and low porosity templates are described in section 2.1 (page 45).

### 3.1.1 Optimisation of the electrolyte

First, the same electrolyte (2.3M Ni - 0.4M Co - 15mM Cu) as in the previous master thesis [44] is elaborated. The results are not satisfying as it can not produce stable and reproducible results (see section 2.1). The resulting samples present an inhomogeneous deposition. The solution is probably too concentrated, and blocks the pores as a consequence. For this reason, a less concentrated solution of 1M Ni - 0.2M Co - 7.5mM Cu is then chosen.

The objective is to have a solution which results in a magnetic layer composed of $50\%$ of Ni and $50\%$ of Co. To evaluate the composition, homogeneous NWs are made. They are brought to the SEM to check the composition. The solution 1M Ni - 0.2M Co - 7.5mM Cu gives $64\%$ of Ni and $36\%$ of Co, with a Cu content of $3\%$. The result does not show the desired balance, so other electrolytes are elaborated. Table 3.1 gives the SEM result of the different electrolytes tested to obtain a composition as close as possible of a 50-50 ratio.

An electrolyte with higher concentrations, 1.5M Ni - 0.25M Co - 15mM – still lower than the first electrolyte – is also tested. The results of the SEM are satisfying, as the measured ratio is really close to the desired one. However, the resulting samples face the same problems as the first electrolyte, showing inhomogeneous deposition. Finally, the electrolyte 1M Ni - 0.17M Co - 7.5mM

Cu is selected notwithstanding the high Cu content. Indeed, the NiCo ratio is not too far from the desired ratio and the deposition process works well with this electrolyte.

| Label | Ni [% Ni and Co] | Co [% Ni and Co] | Cu [atomic %] |
|---|---|---|---|
| Sol_NiCo_2.3MNi_0.4MCo_0.15MCu | 64 ±0.14 | 36 ±1 | 2.5±0.4 |
| Sol_NiCo_0.2 | 40 ±3.1 | 60±4.16 | 3 ±0.58 |
| Sol_NiCo_0.18 | 41±2.84 | 59 ±1.8 | 8.55 ±1.69 |
| Sol_NiCo_0.17 | 42 ±1.98 | 58 ±2.37 | 10.8 ±3.54 |
| Sol_NiCo_0.15 | 81 ±3.24 | 19 ±3.22 | 0.72 ±0.035 |
| Sol_NiCo_1.5MNi_0.26MCo_15mMCu | 44 ±1.05 | 56 ±1.24 | 33 ±0.8 |

TABLE 3.1: Result of the SEM for different electrolytes. Relative content of Ni and Co (%); Cu content (atomic %).

Multilayers are also measured at the SEM. These measurements are more difficult to elaborate because the structure of the wires is less compact due to the different layers. The composition of the multilayers shows a high increase of the Cu content. This is logical, as contrarily to the homogeneous wires, layers with only Cu are added. For the sample Sol_NiCo_2.3MNi_0.4MCo_0.15MCu, we find a Ni content of $27.5 \pm 2.5\%$, a Co content of $11 \pm 0.5\%$ and a Cu content of $62 \pm 2\%$.

First the magnetic and transport properties of HCNWs made of Sol_NiCo_0.15M, Sol_NiCo_0.17M, Sol_NiCo_0.18M and Sol_NiCo_0.2M are analysed. Figure 3.1 shows the hysteresis loop and MR curves of HCNWs for solution Sol_NiCo_0.18 in the IP and OOP direction. In figure 3.1(a), the well defined squareness of the OOP hysteresis loop can be observed. Indeed, for HCNWs, the shape anisotropy effect is more important because of its aspect ratio.

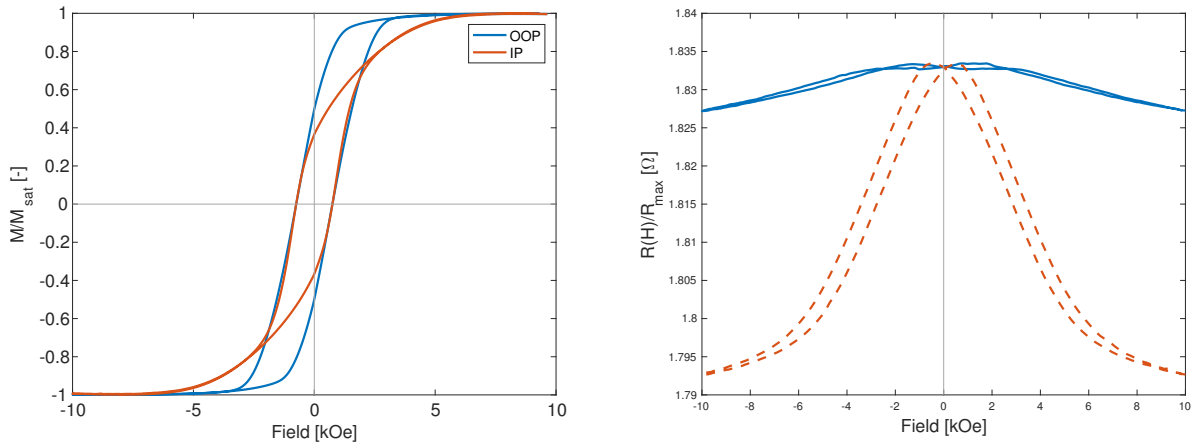


(a) Hysteresis loop

(b) MR curve

FIGURE 3.1: Measurement for HCNWs with Sol_NiCo_0.18M, 1000 s of deposition time in the high porosity template at RT.

Table 3.2 compares the properties of the hysteresis loops of the electrolytes with different Co concentration. The 0.17M shows the highest remanent magnetisation in both directions. High remanent magnetisations are expected for homogeneous NWs due to larger effects of shape anisotropy. The coercive field shows no particular trend with changing Co content.

| Co conc [M] | $(M_r/M_s)_{OOP}$ [-] | $(M_r/M_s)_{IP}$ [-] | $H_{c,OOP}$[kOe] | $H_{c,IP}$[kOe] |
|---|---|---|---|---|
| 0.15 | 0.47 | 0.38 | 0.69 | 0.69 |
| 0.17 | 0.53 | 0.52 | 0.74 | 0.78 |
| 0.18 | 0.50 | 0.37 | 0.75 | 0.75 |
| 0.2 | 0.42 | 0.29 | 0.64 | 0.65 |

TABLE 3.2: Result of $M_r/M_s$ and $H_c$ at RT in IP and OOP directions for the HCNWs with Co concentration of 0.15M, 0.17M, 0.18M, 0.2M.

For the Sol_NiCo_0.18M sample, the MR shows values around 2.2% (figure 3.1(b)). Similar results of MR are observed for Sol_NiCo_0.15M, Sol_NiCo_0.17M and Sol_NiCo_0.2M. The MR is calculated as:

$$MR = \frac{R_{max} - R_{IP}}{R_{max}} \cdot 100 \quad [\,\%\,] \tag{3.1}$$

Previous studies have shown that AMR is comparable to MR [44] in HCNWs. AMR in NiCo alloys in HCNWs has been studied before as shown on figure 3.2. In this paper, the AMR effect is around 3%. This is not too far from the AMR ratio found here.

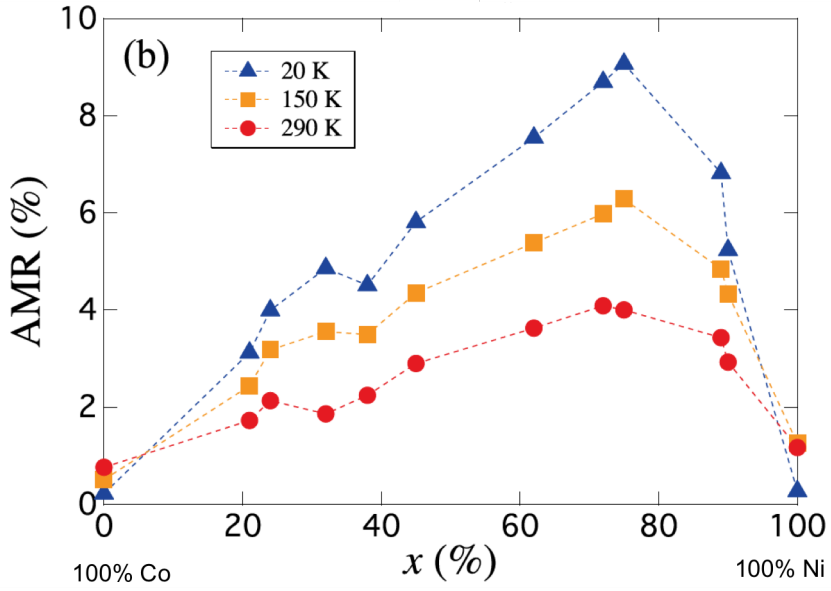


FIGURE 3.2: Variation of the AMR ratio as a function of Ni content in $Ni_xCo_{1-x}$ CNW networks with 40 nm diameter and 20% porosity. The measurements are made at different temperatures [7].

Measurement of HCNWs allows to investigate more accurately the overall resistance of the sample. When an AMR effect is present, there is a variation of the overall sample resistance due to the modification of every angle created between a local magnetisation and the corresponding local current flow direction. A net effect is observable: the electrical resistance is minimised when the direction of the current is perpendicular to the applied magnetic field. AMR is thus related to the relative orientation of the current (and hence the NWs) and the magnetisation. The resistance at a certain angle $\varphi$ between the current density and the magnetisation M is defined as (the notations are the same as the ones defined in section 1.2.4, page 39):

$$\rho(\varphi) = \rho_\perp + (\rho_\parallel - \rho_\perp)\cos^2\varphi \quad [\,\Omega\cdot\,\mathrm{m}\,]$$

When studying GMR properties of MCNWs, the saturation at magnetisation should be identical in IP and OOP directions as the structure is composed of parallel layers. However, a gap between the $GMR_{IP}$ and $GMR_{OOP}$ curves is often observed, indicating a presence of AMR. To evaluate the AMR effect in the MCNWs, a simple parameter is searched. This should be a value that depends on the OOP and IP direction but that is independent of the GMR. By finding a relation between the MR (which is closely linked to the AMR) and GMR, the effect of AMR can be approximated. The difference between $GMR_{IP}$ and $GMR_{OOP}$ can be expressed as:

$$\begin{aligned} \Delta GMR &= GMR_{IP} - GMR_{OOP} \\ &= \tfrac{R_{max}-R_{IP}}{R_{IP}} \cdot 100 - \tfrac{R_{max}-R_{OOP}}{R_{OOP}} \cdot 100 \\ &= \tfrac{R_{max}}{R_{IP}} \cdot \tfrac{R_{OOP}-R_{IP}}{R_{OOP}} \cdot 100 \\ &= (\tfrac{GMR_{IP}}{100} + 1) \cdot \Delta MR \quad [\,\%\,] \end{aligned} \tag{3.2}$$

In equation (3.2), $\Delta MR$ is a good candidate to represent the AMR effect. Indeed, when looking at the definition of the MR given in equation (3.1), $\Delta MR$ is really similar to this definition of MR. The only difference is that $R_{max}$ in equation (3.1) is replaced by $R_{OOP}$ in equation (3.2). When looking at figure 3.3(A), one can see that it is a reasonable approximation. The green arrow shows the small difference between $R_{OOP}$ and $R_{max}$ when doing MR measurements on HCNWs. In figure 3.3(B), one can see that the $R_{max}$ presents a totally different value than the $R_{max}$ in figure 3.3(A): both are describing different effects.

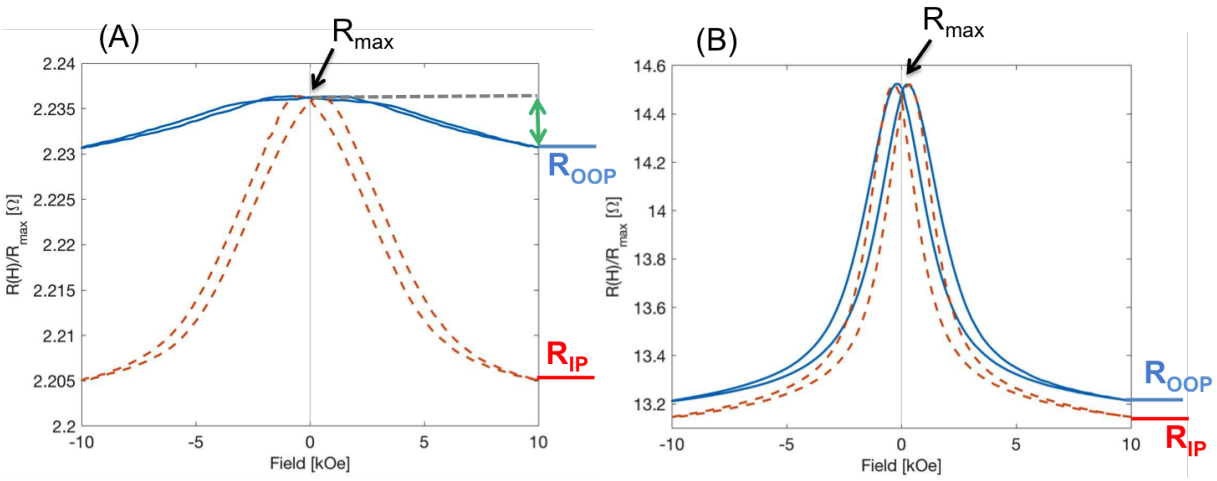


FIGURE 3.3: (A) MR curve of HCNWs and (B) GMR curve for MCNWs. Both curves are obtained with samples made from the Sol_NiCo_0.2M in the high porosity template. For the MCNWs, the NiCo layer deposition time is 500 ms and Cu layer deposition time 16 s.

After studying the HCNWs, MCNWs made of the same electrolytes[1] are analysed and optimised. Figure 3.4 shows the hysteresis loop in the OOP direction and the GMR curves in the IP direction. The deposition time is 600 ms for the NiCoCu layer and 16 s for the Cu layer. The hysteresis loops appear to be very similar. The GMR curves shows higher results for the 0.17M and 0.18M Co.

[1]Sol_NiCo_0.15M, Sol_NiCo_0.17M, Sol_NiCo_0.18M and Sol_NiCo_0.2M

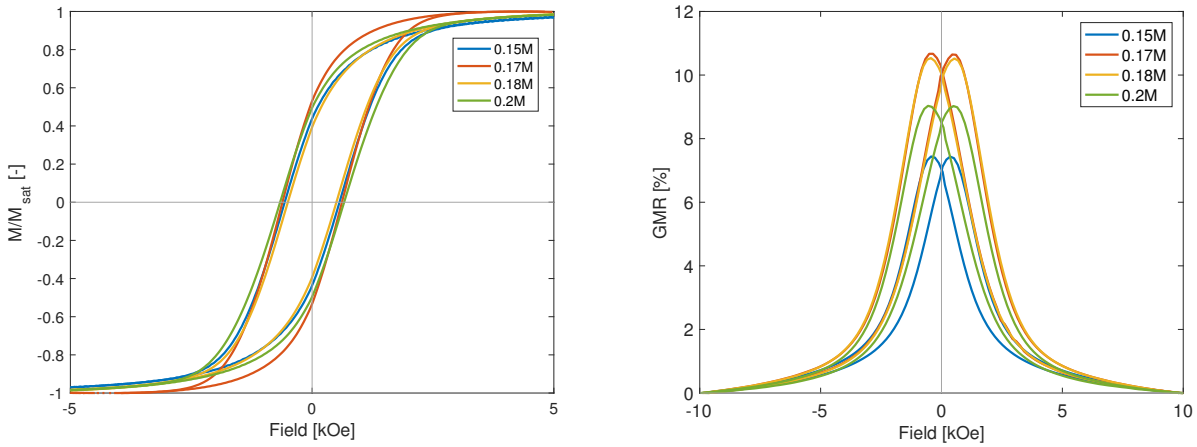


(a) OOP Hysteresis loop

(b) IP GMR

FIGURE 3.4: Results of AGM and GMR for Sol_NiCo_0.15M, Sol_NiCo_0.17M, Sol_NiCo_0.18M and Sol_NiCo_0.2M in high porosity templates at RT. The NiCo layer deposition time is 600 ms and the Cu layer deposition time 16 s.

Table 3.3 gives some magnetic and magnetotransport values obtained on MCNWs for electrolytes with a composition of 1M Ni and 7.5mM Cu and where the Co concentration is slightly modified. $\Delta MR$, reformulating equation (3.2), is defined as:

$$\Delta MR = \frac{\Delta GMR}{GMR_{IP} + 100} \cdot 100 \quad [\,\%\,]$$

| Co conc [M] | $GMR_{IP}$ [%] | $\Delta$ MR [%] | $(M_r/M_s)_{OOP}$ [-] | $H_{c,OOP}$[kOe] |
|---|---|---|---|---|
| 0.15 | 8.26 | 0.57 | 0.44 | 0.57 |
| 0.17 | 10.89 | 0.85 | 0.53 | 0.62 |
| 0.18 | 10.53 | 0.67 | 0.41 | 0.54 |
| 0.20 | 9.03 | 0.83 | 0.48 | 0.66 |

TABLE 3.3: Results of the $GMR_{IP}$, $\Delta MR$, $(M_r/M_s)_{OOP}$ and $H_{c,OOP}$ for Sol_NiCo_0.15M, Sol_NiCo_0.17M, Sol_NiCo_0.18M and Sol_NiCo_0.2M in high porosity templates at RT. The Cu-layer deposition time is 16 s and the magnetic layer deposition time 600 ms.

The evolution of the coercive field and normalised remanent magnetisation are shown in figure 3.5(a) and (b). As for the HCNWs (grey on the plot), no general trend is observed. The coercive field is almost always larger for the HCNWs then for the MCNWs, as should be expected. The electrolyte with 0.2 M Co has almost the same coercive field for HCNWs and MCNWs. The remanent magnetisations are really similar for both types of wires configurations. These results are surprising because the remanent magnetisation should be higher in HCNWs as the shape anisotropy has a higher impact in HCNWs. The gap between the OOP and IP curves is constant on both plots. The IP curves show lower coercive field and lower remanence, reflecting more isotropic behaviour.

Figure 3.5(c) illustrates the GMR results with varying Co concentration. The GMR results are in the same range for the different electrolytes. The maximum $GMR_{IP}$ appears at 0.17 M of Co and has a result very similar as 0.18 M. This is consistent, as the SEM results show very similar amounts of Ni and Co in the ferromagnetic layers for both electrolytes. The $\Delta MR$ (in figure 3.5(d)) is almost constant when the Co content increases and has values below 1%.

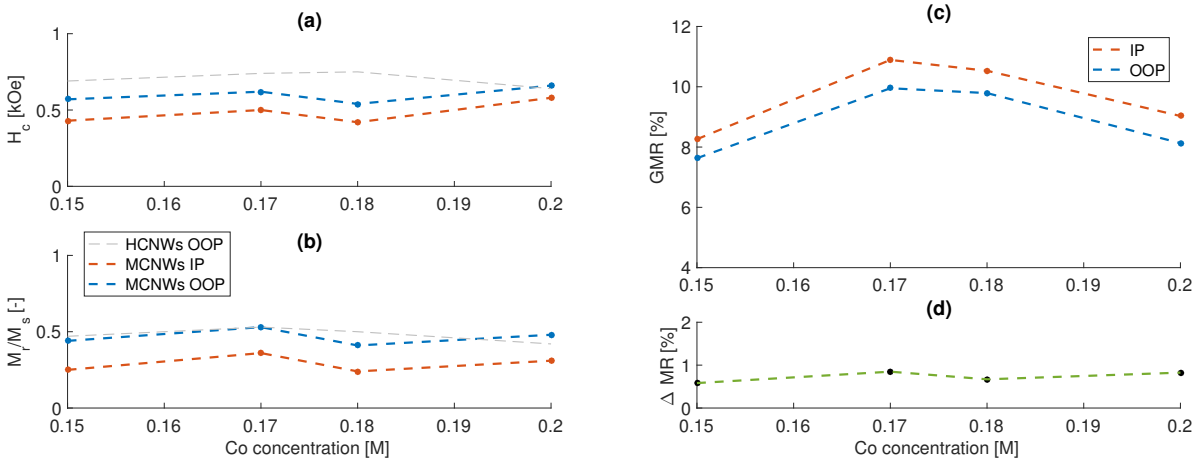


FIGURE 3.5: (a) Coercive field; (b) normalised remanent saturation; (c) GMR ; (d) ΔMR as a function of the Cobalt concentration in the high porosity template at RT. The deposition time is 16 s for the Cu layer and 600 ms for NiCo. The electrolytes have a Ni and Cu concentration of 1M and 7.5mM respectively.

Finally, after comparing the different results, the 0.17M electrolyte is chosen. Indeed, the electrolyte shows an adequate NiCo ratio and the best GMR results. The electrolyte with higher concentrations, Sol_NiCo_1.5MNi_0.26MCo_15mMCu, shows a better NiCo ratio but proper samples could not be made from this electrolyte. Trying to optimise this electrolyte would have required many samples with no reliable or reproducible results. As an objective of this master thesis is to acquire stable statistics of the GMR results for ferromagnetic layers made of NiCo alloy, this electrolyte is not a good choice. To be sure of the Sol_NiCoCu_0.17M choice, samples with different magnetic layers are fabricated for the Sol_NiCoCu_0.2M. The GMR results are not as good as for the Sol_NiCoCu_0.17M, so this solution is not further optimised.

### 3.1.2 High porosity template

#### Optimisation of the deposition time of the magnetic layer

After exploring different electrolytes, one electrolyte (Sol_NiCoCu_0.17M) is kept following the choice explained in the previous section. The deposition time of the ferromagnetic and non-magnetic layer are successively optimised. First, OOP hysteresis loops and IP GMR curves of samples with different magnetic layer deposition time, illustrated in figure 3.6, are observed and compared. The measurements are done at RT with high porosity templates and a Cu layer deposition time of 16 s. The hysteresis loops (figure 3.6(a)) are very similar to each other. The GMR curves (figure 3.6(b)) are similar in shape, with higher amplitude for a NiCo deposition time of 600 ms. Table 3.4 gives some magnetic and magnetotransport values obtained for the samples made during the magnetic layer optimisation.

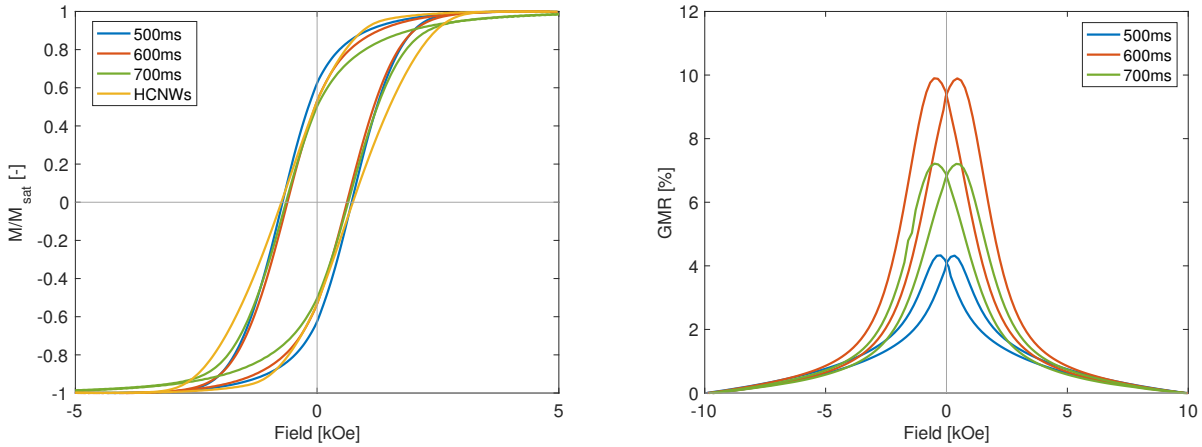


(a) OOP Hysteresis loop

(b) IP GMR

FIGURE 3.6: Results of AGM and GMR for different NiCo layer deposition times (500ms, 600 ms and 700 ms) for the Sol_NiCoCu_0.17M in high porosity templates at RT. The Cu layer deposition time is 16 s. The hysteresis loop of the HCNWs is also depicted.

| Magnetic layer [ms] | $GMR_{IP}$ [%] | $\Delta$ MR [%] | $(M_r/M_s)_{OOP}$ [-] | $H_{c,OOP}$[kOe] |
|---|---|---|---|---|
| 300 | 0.85 | 0.27 | 0.31 | 0.31 |
| 400 | 7.06 | 0.50 | 0.55 | 0.65 |
| 500 | 6.81 | 0.50 | 0.63 | 0.72 |
| 600 | 10.89 | 0.85 | 0.53 | 0.62 |
| 700 | 7.21 | 0.64 | 0.50 | 0.64 |

TABLE 3.4: Result of the $GMR_{IP}$, $\Delta MR$, $(M_r/M_s)_{OOP}$ and $H_{c,OOP}$ for different magnetic layer deposition times, for Sol_NiCoCu_0.17M in high porosity templates at RT. The Cu layer deposition time is 16 s.

Figure 3.7(a) and (b) show the coercive field and normalised remanence magnetisation as a function of magnetic layer deposition time. For 300 ms of magnetic layer deposition time a much smaller and similar coercive field in IP and OOP direction is observed. The remanent magnetisation of this sample also shows a different behaviour, because the $M_{R,IP}$ is larger than the $M_{R,OOP}$. This suggests that, because of the very thin layers, the easy-axis of magnetisation is not along the NW axis anymore, but perpendicular to it. Above 400 ms of deposition time, the coercive field and the remanence magnetisation keep a regular gap between the IP and OOP direction; they show a maximum around 500 ms and then decrease slightly. Normally, they should increase and get closer to the result of HCNWs as the magnetic layer width increases (and so the aspect ratio). The results of the HCNWs in the OOP direction are close to the MCNWs in the OOP direction above 400 ms. This is not expected, as usually the HCNWs show higher $H_c$ and $M_r$ than MCNWs. This suggests that above a certain magnetic layer thickness, the dipolar coupling between the layers does not affect the $H_c$ and $M_r$ anymore.

Figure 3.7(c) shows the GMR as a function of the magnetic layer thickness. A peak is observed at 600 ms of magnetic layer deposition time. The very low result of the 300 ms of magnetic layer deposition time suggests that the layers are really thin and maybe not well defined. The $\Delta MR$ (figure 3.7(d)) increases as the magnetic layer increases which is the expected behaviour as it become closer to the HCNWs and thus the AMR effect is more pronounced.

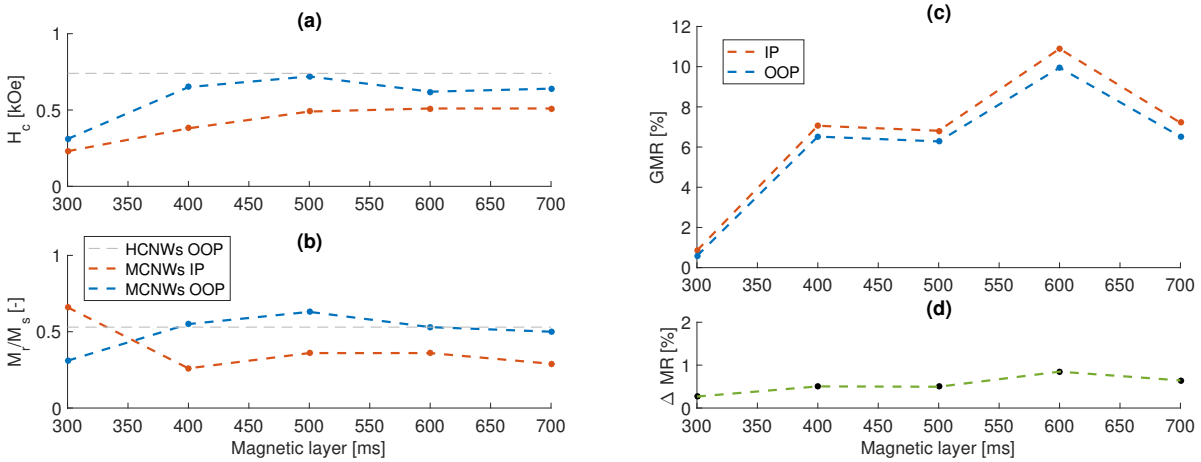


FIGURE 3.7: (a) Coercive field; (b) normalised remanent saturation; (c) GMR ; (d) ΔMR as a function of magnetic layer deposition time, for Sol_NiCo_0.17 in high porosity template at RT. Cu layer deposition time is 16 s.

When comparing the obtained values for the GMR, 600 ms seemed to be the best deposition time to get a magnetic layer thickness with the optimum GMR results. This value was hence fixed to optimise the Cu layer.

### Optimisation of the deposition time of the Cu layer

The Cu layer has been optimised by testing different values around 16 s of Cu layer deposition time, namely 12s, 14 s and 18s. The NiCo layer deposition time is fixed to 600 ms for the reason explained in the previous section. Figure 3.8(a) shows a zoom of the hysteresis loops in OOP direction between -5 kOe and 5 kOe for the 12s, 14 s and 18 s Cu layers. The three hysteresis loops are really similar. Figure 3.8(b) shows GMR curves for the same samples. For 12 s of Cu deposition time, the curves are broader. The 14 s curves show thinner peaks with better results. Table 3.5 indicates values of the magnetic and magnetotransport properties of these curves.

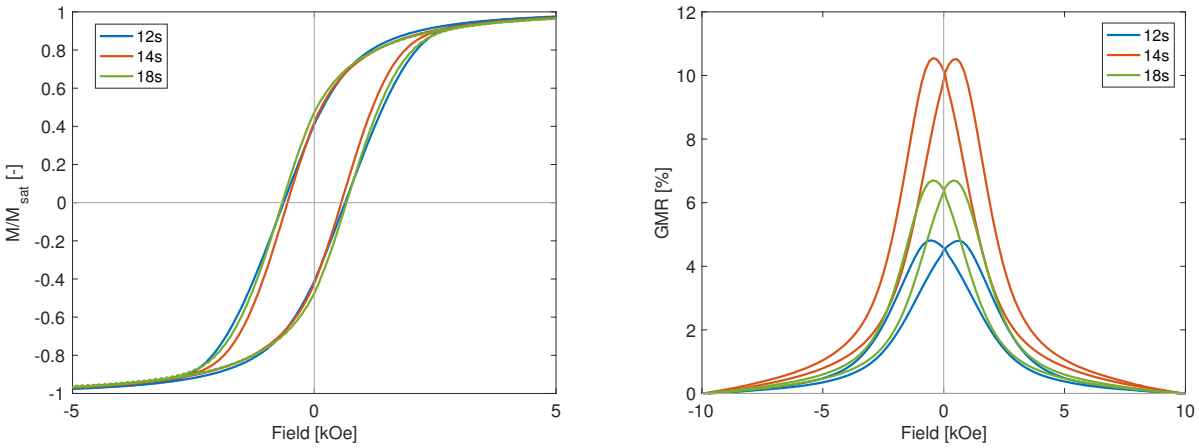


(a) OOP Hysteresis loop

(b) IP GMR

FIGURE 3.8: Result of AGM and GMR for different Cu layer deposition times (12 s, 14 s, 18 s) for the Sol_NiCoCu_0.17M in high porosity templates at RT. The NiCo layer deposition time is 600 ms.

| Cu layer [s] | $GMR_{IP}$ [%] | $\Delta$ MR [%] | $(M_r/M_s)_{OOP}$ [-] | $H_{c,OOP}$[kOe] |
|---|---|---|---|---|
| 12 | 4.81 | 0.60 | 0.41 | 0.64 |
| 14 | 10.55 | 1.15 | 0.43 | 0.56 |
| 15 | 9.93 | 0.79 | 0.44 | 0.62 |
| 16 | 10.89 | 0.85 | 0.53 | 0.62 |
| 18 | 6.70 | 0.48 | 0.48 | 0.67 |

TABLE 3.5: Result of the $GMR_{IP}$, $\Delta MR$, $(M_r/M_s)_{OOP}$ and $H_{c,OOP}$ for different Cu layer deposition time, for Sol_NiCoCu_0.17M in high porosity templates at RT. The magnetic layer deposition time is 16 s.

Figures 3.9(a) and (b) show the evolution of the coercive field and remanent magnetisation as the Cu layer's thickness increases. In both plots, the coercive field and remanent magnetisation seem not to depend on the Cu layer deposition time as the curves are almost constant. This result is not expected because when the Cu layers increase, less dipolar interaction between the layers appears. As a consequence, less anisotropy along the OOP axis, and so a decrease in $H_c$, is expected. The curve showing the HCNWS in the OOP direction is above the MCNWs in OOP which is the expected result. At 16 s, the remanent magnetisation has similar results for MCNWs and HCNWs which is strange and was already observed in the previous part.

Figure 3.9(c) shows the result of the GMR for the different Cu deposition times. First, the GMR increases when the Cu-layer increases. The low values of GMR in the beginning of the curves can be explained by the not-well defined Cu-layer due to too short deposition time. Then a plateau appears with the highest values of GMR (between 14 s and 16 s). Finally, the GMR decreases. Indeed, when the Cu layers are larger than the spin diffusion length, spin mixing arises. The electrons have more time to collide and thus spin flipping occurs, which is of course to avoid for good GMR results. Concerning the $\Delta MR$ (figure 3.9(d)), first a low value is observed but otherwise a general trend shows a decrease of $\Delta MR$ as the Cu layer increases. This is expected because the aspect ratio of ferromagnetic layers decreases.

When looking at figure 3.9(c), one can observe a plateau between 14 s and 16 s of deposition time for the Cu layer. Better GMR results are expected for thinner layers, as long as they are well defined, because the probability of spin-flipping decreases. Samples were hence realised with a Cu layer deposition time of 14 s and thinner magnetic layers (400 ms and 500 ms). The results were not satisfying, giving around 7% of GMR in the IP direction. Another combination was also tested by again reducing both layers: 300 ms and 450 ms for the magnetic layer and 12 s for the Cu-layer. This, again, gave poor results of around 4% of GMR in the IP direction. As a consequence, the conclusion was that the best time for the Cu layer is of about 14 s $\sim$ 16 s and so the optimisation made before with a fixed Cu layer deposition time of 16 s is adequate.

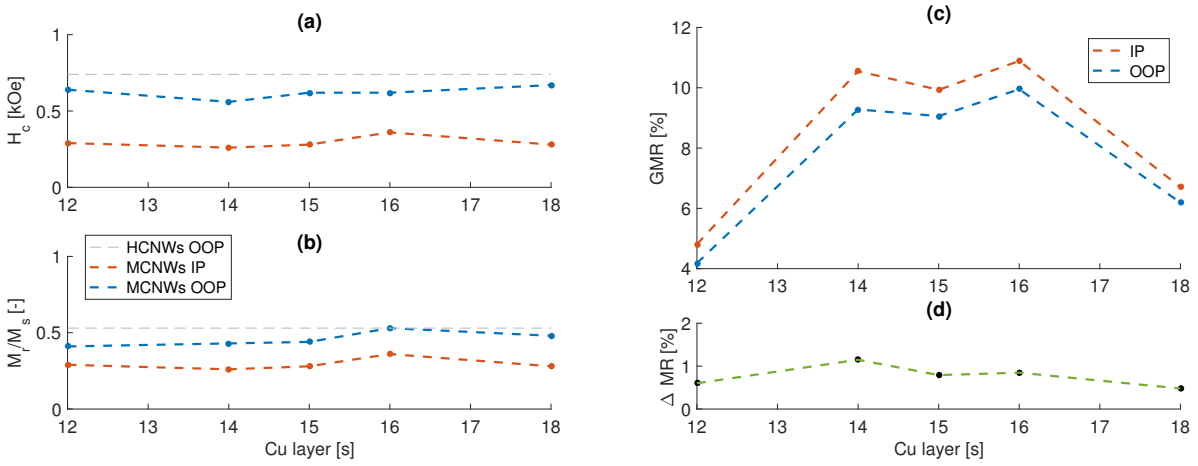


FIGURE 3.9: (a) Coercive field; (b) normalised remanent saturation; (c) GMR ; (d) ΔMR as a function of Cu layer deposition time, for Sol_NiCo_0.17 in high porosity template at RT. Magnetic layer deposition time is 600 ms.

### 3.1.3 Low porosity template

The best result for Sol_NiCo_0.17, namely NiCo/Cu 600 ms/16s, was obtained on the low porosity template. As explained in section 2.4 on page 57, the influence of the intersection can play a large role on GMR results. The intersections add a resistance in series to the GMR, which produces less good GMR results. By using templates with different porosity, the effect of the intersections with the type of alloy in the ferromagnetic layer is analysed. The diminution of temperature produces larger GMR results. The change with respect to the RT results depends on the alloy. By doing measurements at low temperature (LT), the impact of spin-flip at RT can be estimated. The result of the GMR at RT and LT for the low porosity template are shown in the following section.

#### Low temperature measurement

As expected, low porosity networks are better to get higher GMR results. As the multilayered structure is not well formed in the interconnections between nanowire segments, the reduction of packing density reduces the volume fraction of interconnections normalised by the volume fraction of NWs. Long wires with few interconnections will produce a better multilayered structure with less coupling between the NWs and as a consequence a larger GMR effect. The maximum result obtained for the high porosity template was $\sim 11\%$ while for the low porosity template, it was $\sim 36\%$.

The GMR curves made at RT are shown in figure 3.10(a) and have a value of $\text{GMR}_{IP}$ of 35.67% and $\text{GMR}_{OOP}$ of 32.53%. The LT curves show much higher results (figure 3.10(b)): 76.75% and 67.1% in $\text{GMR}_{IP}$ and $\text{GMR}_{OOP}$ respectively. The $\Delta MR$ at RT is 2.31%, and 5.46% at LT. The increase of AMR with decreasing temperature is expected as a result of smaller resistivities of the alloys [8] as shown in figure 3.2. The increase of Δ MR from high porosity template to low porosity template is probably linked to the decrease of intersections between the NWs. Moreover, on the high porosity template, the NWs diameter are smaller, which can reduce the resistivity of the Cu layers in a larger way than the ferromagnetic layers which are already more resistive. This produces a smaller 0-field resistivity and as a consequence a smaller AMR.

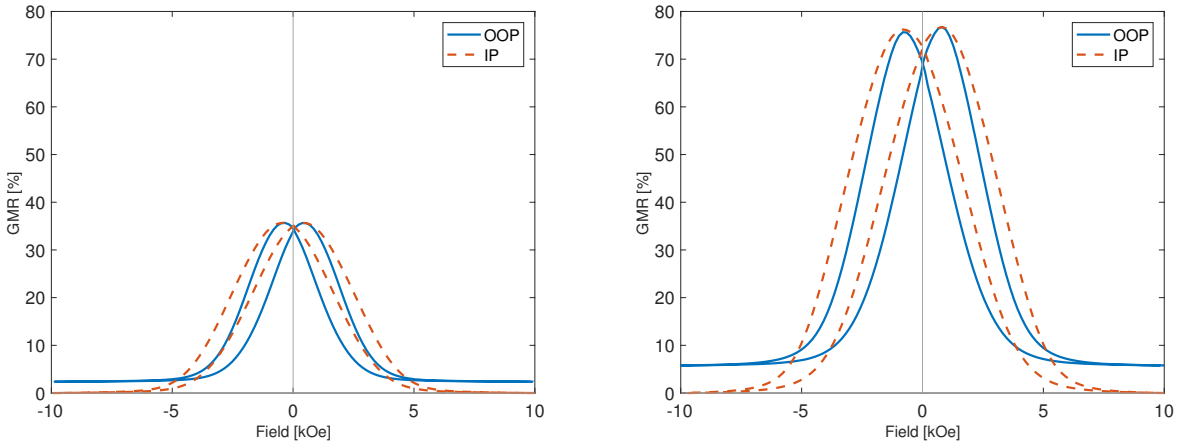


(a) T∼300K (b) T∼12K

FIGURE 3.10: GMR curves at different temperatures for the Sol_NiCoCu_0.17M in low porosity templates. The NiCo layer deposition time is 600 ms and Cu layer deposition time 16 s.

## 3.2 $Ni_{25}Co_{75}$/Cu multilayer crossed nanowire networks

After exploring $Ni_{50}Co_{50}$ ferromagnetic layers, a new ratio of NiCo is analysed, namely $Ni_{25}Co_{75}$. An appropriate electrolyte composed of 1M of Ni, 0.4M of Co and 7.5mM of Cu is rapidly found (Sol_NiCo_0.4). The SEM measures a ratio of $22 \pm 4\%$ Ni and $78 \pm 3\%$ Co, with a content of $8\% \pm 1.5$ of Cu. For this electrolyte, only the magnetic layer is optimised. Indeed, the electrolyte has the same Cu concentration as Sol_NiCoCu_0.17M, so the previously optimised result for the Cu layer can be applied to this electrolyte. The electrolyte used for this ratio shows worse results than the ones tested for the $Ni_{50}Co_{50}$ ratio. Hence, only a few samples are made with this electrolyte.

### 3.2.1 High porosity template

As in the previous section, the magnetic layer is first optimised on the high porosity template, then the best result is applied on a low porosity template.

#### Optimisation of the deposition time of the magnetic layer

Figure 3.11(a) illustrates hysteresis loops in the OOP direction for samples with a magnetic layer deposition time of 300 ms, 600 ms, 1000 ms and for HCNWs. The hysteresis loop corresponding to a 300 ms deposition time shows a more pronounced squareness, while the other loops are similar in shape. The HCNWs show the highest coercivity. Larger magnetic layers seem to be more isotropic. Figure 3.11(b) shows the IP GMR curves for the same samples. The 600 ms deposition time shows higher GMR results. All three GMR curves are quite narrow, with the same shape. The shape of the curve of the 1000 ms is slightly broader, which reveals a higher coercive field in the IP direction. Table 3.6 gives the numeric results found when doing the AGM and GMR measurements at room temperature.

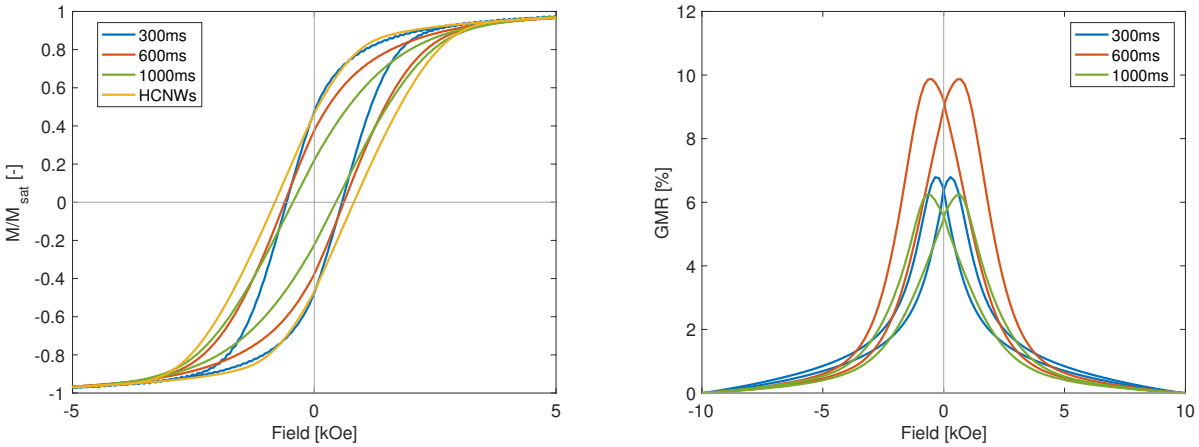


(a) OOP hysteresis loop direction

(b) IP GMR

FIGURE 3.11: Results of AGM and GMR for different NiCo layer deposition times (300 ms, 600 ms and 1000 ms) for the Sol_NiCoCu_0.4M in high porosity templates at RT. The Cu layer deposition time is 16 s. The hysteresis loop of the HCNWs is also represented.

| Magnetic layer [ms] | $GMR_{IP}$ [%] | $\Delta$ MR [%] | $(M_r/M_s)_{OOP}$ [-] | $H_{c,OOP}$[kOe] |
|---|---|---|---|---|
| 300 | 6.79 | 0.39 | 0.48 | 0.57 |
| 600 | 9.87 | 0.64 | 0.38 | 0.61 |
| 800 | 9.71 | 0.69 | 0.29 | 0.62 |
| 1000 | 6.24 | 0.49 | 0.22 | 0.44 |

TABLE 3.6: Results of the $GMR_{IP}$, $\Delta MR$, $(M_r/M_s)_{OOP}$ and $H_{c,OOP}$ for different magnetic layer deposition times, for Sol_NiCoCu_0.17M in high porosity templates at RT. The Cu layer deposition time is 16 s.

Figure 3.12(a) and (b) summarises the results obtained for the coercive field and remanent magnetisations in IP and OOP directions as a function of the NiCo layer deposition time for a fixed Cu layer deposition time of 16 s. The 600 ms and 800 ms samples present an isotropic behaviour as the coercive fields are really similar and the remanent magnetisations close to each other. The behaviour of the 1000 ms is unexpected. Indeed, the coercive field should still increase and the remanent magnetisation should be higher in the OOP direction. This was probably a defective sample. However, the remanent magnetisation in the OOP directions also shows a decrease when going from 300 ms to 800 ms, which is unexpected for reasons explained before.

Figure 3.12(c) shows the evolution tendency of the GMR with increasing magnetic layer deposition time for Sol_NiCo_0.4 and a 16 s Cu layer deposition time. A plateau is observed between 600 and 800 ms, then the GMR decreases. Compared to the 50-50 NiCo ratio, thicker magnetic layers seem to be more adapted to the 25-75 ratio. When looking at $\Delta MR$, a slight increase is observed until 800 ms, which is the expected trend. The $\Delta MR$ of the 1000 ms sample shows an unexpected decrease which corroborates the fact that this sample is probably deficient.

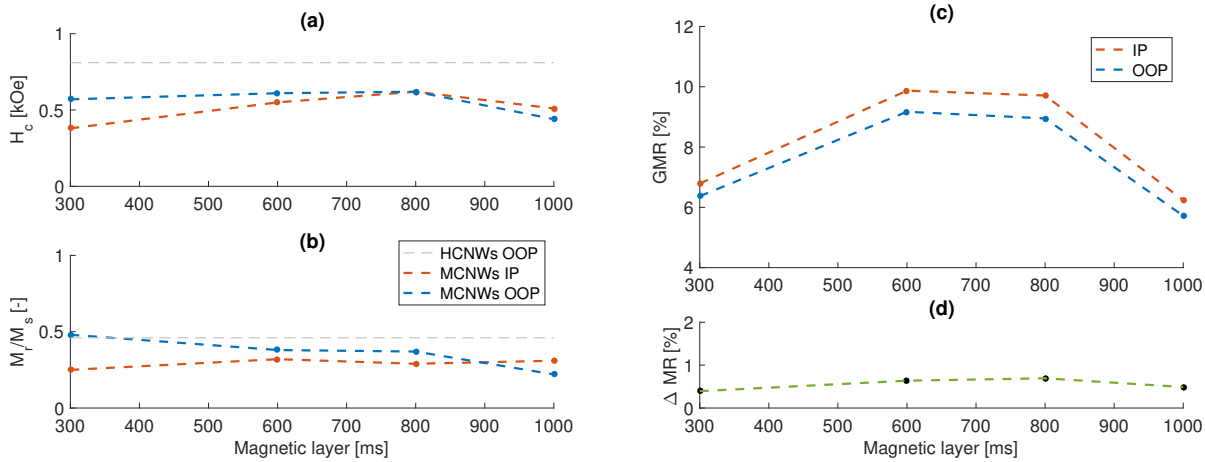


FIGURE 3.12: (a) Coercive field; (b) normalised remanent saturation; (c) GMR ; (d) ΔMR as a function of magnetic layer deposition time, for Sol_NiCo_0.4 in high porosity template at RT. The Cu layer deposition time is 16 s.

### 3.2.2 Low porosity template

The next step is to select the best parameters obtained on the high porosity template to apply them on the low porosity template. First, to better understand and be able to compare the obtained results, a HCNWs sample is made. The hysteresis loop of this sample was measured but only the OOP curve could be obtained due to problems with the machine. Then, the MR curves of HCNWs on the low porosity template was measured.

Figure 3.13 compares the OOP hysteresis loop in the high an low porosity template. The low porosity template attains the saturation magnetisation at lower field then the high porosity template but the magnetic reversal is more abrupt in the low porosity template. This behaviour is related to both, the decrease of dipolar coupling between nanowires in the low porosity template and the stronger effect of the shape anisotropy in the high porosity template with lower NWs diameter.

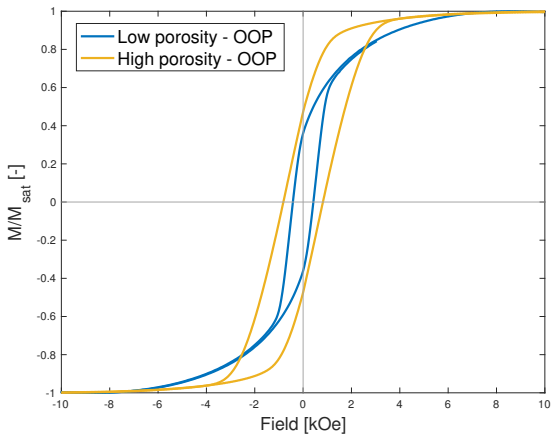


FIGURE 3.13: Comparison between OOP hysteresis loop of high and low porosity template of HCNWs with Sol_NiCo_0.4M

.

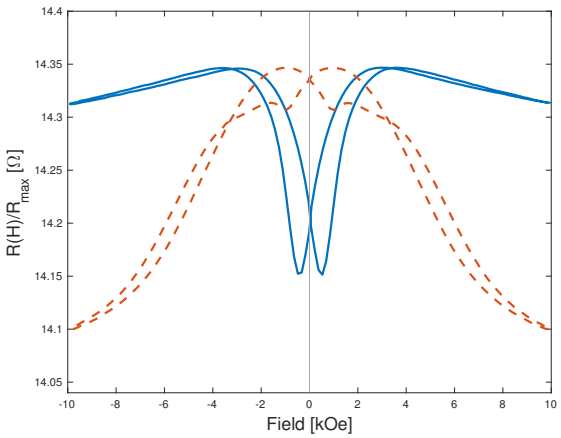


FIGURE 3.14: MR curve of HCNWs with Sol_NiCo_0.4M, 1000 s of deposition time in low porosity template at RT.

Figure 3.14 presents the MR measurement of the HCNWs made of Sol_NiCo_0.4M in the low

porosity template. The MR values is around 1.8% which is similar than the results from the literature shown on figure 3.2. Because the measurement begins at 10 kOe (and not at 0-field as common AMR curves), a large decrease of resistance is observed around zero field when the magnetisation reversal occurs. This is linked to the fact that during a short moment the magnetic moments inside the ferromagnetic layers lay perpendicular to the current. The IP curves are showing a decrease of resistance when the magnetic moment are perpendicular to the current, typical from a change in magnetisation following a rotation.

**Low temperature measurement**

For the high porosity templates, the 600 ms and 800 ms deposition times show the best results. The 600 ms one is selected to allow better comparison between the low porosity template of the Sol_NiCoCu_0.17M and Sol_NiCoCu_0.4M. The transport properties of this sample at low temperature are also observed. Figure 3.15(a) shows the GMR curves for the low porosity template at RT. The results are 30.82% for GMR$_{IP}$ and 27.4% for GMR$_{OOP}$, which is much higher than on the high porosity template (GMR$_{IP} \sim 10\%$). However, the transition from high porosity to low porosity is less marked than for the 50-50 NiCo ratio. This suggests that alloys with higher Co content are less affected by the CNWs intersections.

The low temperature measurement (figure 3.15(b)) gives 60.21% and 54.87% in IP and OOP directions, respectively. The LT measurement is the double of the RT measurement. The $\Delta MR$ is $\sim 2.61\%$ at RT and $\sim 3.3\%$ at LT. The RT $\Delta MR$, like for the Sol_NiCoCu_0.17M, is larger for the low porosity template than for the high porosity one. The $\Delta MR$ increases at LT as expected.

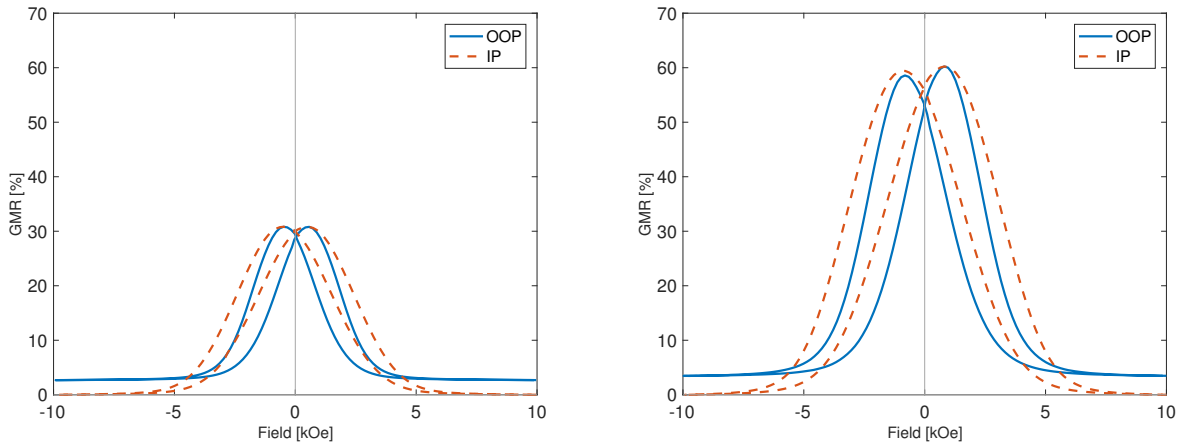


(a) T∼300K (b) T∼12K

FIGURE 3.15: GMR curves at different temperatures for the Sol_NiCoCu_0.4M in low porosity templates. The NiCo layer deposition time is 600 ms and the Cu layer deposition time is 16 s.

## 3.3 Co/Cu multilayer crossed nanowire networks

Finally, this third section explores ferromagnetic layers solely made of Cobalt. Multilayers of Cu-Co are an obvious choice since large GMR changes have been reported for this multilayer system [19]. In addition, the generally accepted equilibrium phase diagram shows virtually no solubility of Co in Cu, and $< 9\%$ of solubility of Cu in Co, below $500°$C [4].

In this section, the samples made of two types of electrolytes of the same composition, but with different pH are discussed. Figure 3.16 and figure 3.18 show HCNWs OOP hysteresis loops made

of electrolytes Sol_Co_pH2 and Sol_Co_pH4 in the high porosity and low porosity template respectively. Studies suggest that when the pH decreases, the preferential structural phase – hcp grains with their c-axis oriented perpendicular to the wires – changes gradually towards an fcc structural phase. The electrolyte obtained when preparing the solution without changing the pH, has a pH between 3.5 and 4. The Co structure obtained is expected to have its hcp c-axis perpendicular to the wires as described in section 1.2.2. The structural changes can be attributed to the influence of absorbed hydrolysis products at the cathode as well as to the evolution of hydrogen, which are known to depend on the pH [11]. In the high porosity template, the changes are not as much marked as for the low porosity template, but can still be observed. Figure 3.17, from the literature [8], allows to compare figure 3.16 as the same template is used and the same pH are compared. However the electrolytes used in this thesis contains Cu which is not the case for the image coming from the literature. This is probably linked to the fact that the differences between the pH2 and pH4 in figure 3.16 are less apparent.

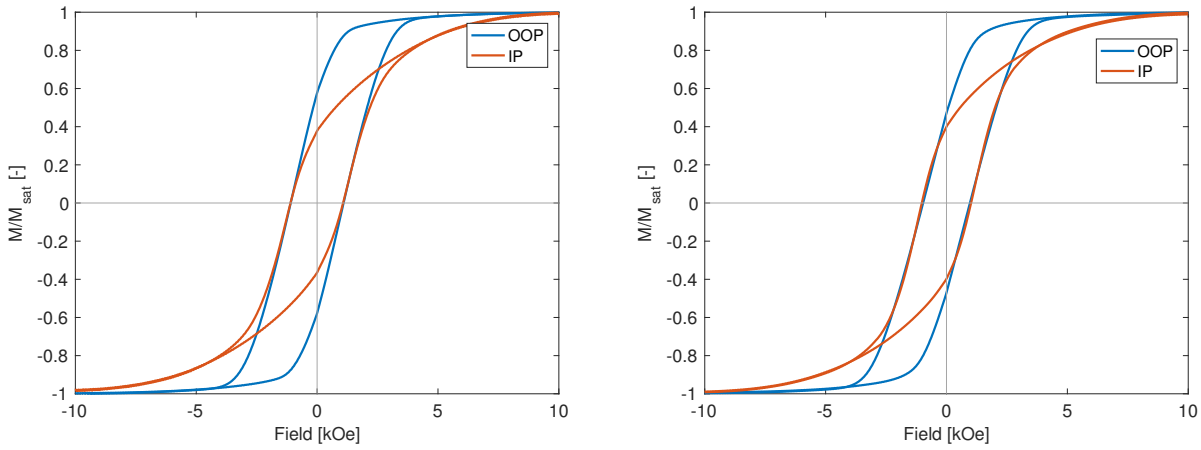


(a) pH2 (b) pH4

FIGURE 3.16: Hysteresis loop of HCNWs from Sol_CoCu_pH2 and Sol_CoCu_pH4 with different pH in high porosity templates at RT.

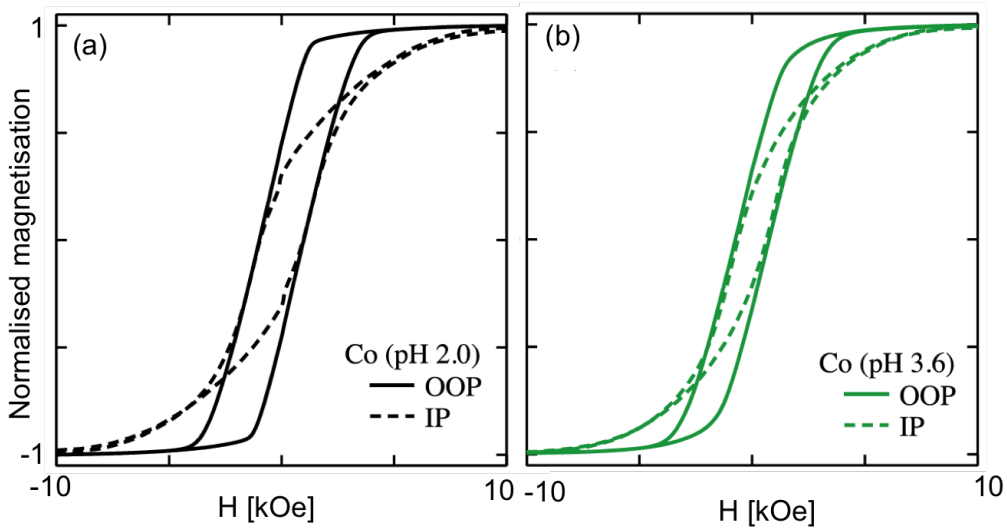


FIGURE 3.17: Hysteresis loop of HCNWs made of a pH2 (a) and pH4 (b), 0.8M Co electrolyte in high porosity template. [8]

However, when looking at the figure 3.18, the changes between pH2 and pH4 are much more visible. The coercive field in the OOP direction for the pH2 sample has a value of 0.47 kOe compared to 0.11 kOe for the pH4; the OOP normalised remanent magnetisation has a value of 0.46 and 0.11 for the pH2 and pH4 samples respectively. These results corroborate previous studies, showing larger shape anisotropy for the pH2 sample, and a diminution of the coercive field and remanent magnetisation with pH4 due to the competition between the shape and magnetocrystalline anisotropies.

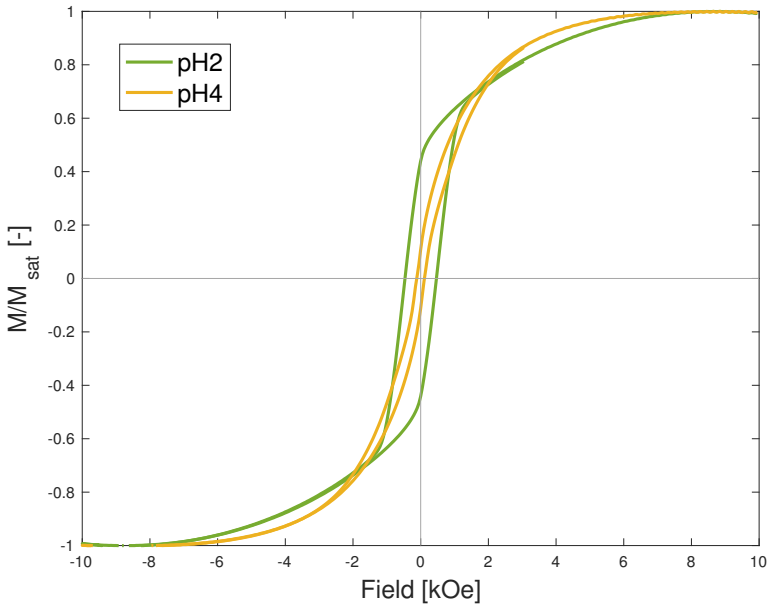


FIGURE 3.18: Hysteresis loop of HCNWs from Sol_CoCu_pH2 and Sol_CoCu_pH4 with in the low porosity templates at RT.

After observing the magnetic properties of HCNWs, the transport properties are analysed by looking at their MR curves. Figure 3.19(a) and figure 3.19(b) shows the MR curve for Sol_CoCu_pH2 and Sol_CoCu_pH4 in the low porosity template. The MR values is about 1.5% and 0.46 % for the pH2 and pH4 samples respectively. This decrease in AMR when the pH of Co increases has also been observed in previous studies [8]. In figure 3.19(a), as in the previous MR figures of this chapter, it can be clearly observed that the magnetic moment changes its direction in a sudden reversal in the OOP direction and in a rotation in the IP direction. Figure 3.19(b) shows a lot of noise but still a big difference with figure 3.19(a) can be observed. There seems to be a magnetic reversal in both direction and also rotation in IP and a slight rotation in OOP. These changes corroborate the results observed on the hysteresis loops and suggest the presence of MC anisotropy. However as the studied directions are IP and OOP, and not parallel and perpendicular directions, the shape anisotropy and MC anisotropy are more difficult to distinguish as is explained in section 1.2.4.

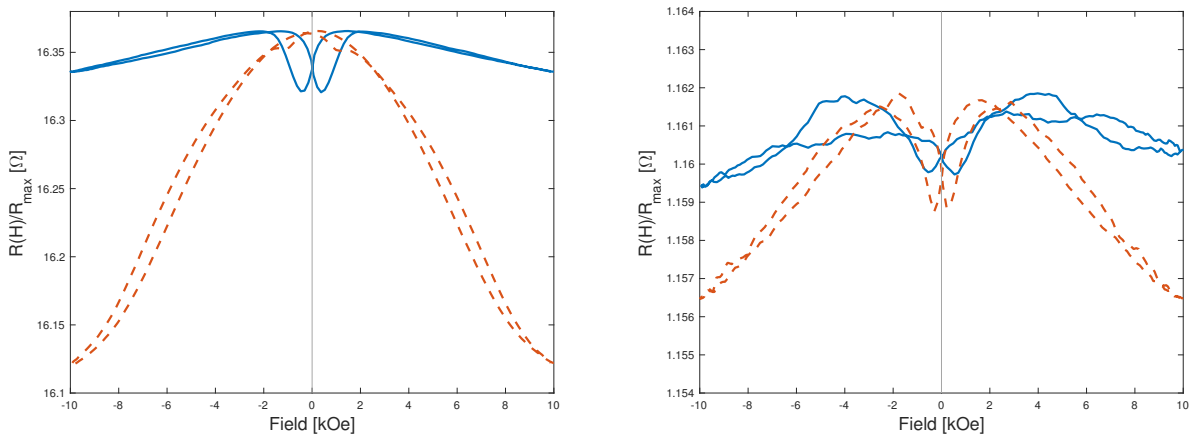


(a) pH2 (b) pH4

FIGURE 3.19: Result of MR for HCNWs for the Sol_CoCu_pH2 and Sol_CoCu_pH4 in the low porosity templates at RT.

### 3.3.1 Optimisation of the electrolyte

First, the two types of electrolyte are compared. The SEM results of HCNWs give 78±3.5% of Co and 22±3.5% of Cu for the pH2 electrolyte, and $90 \pm 12.45\%$ and $10 \pm 12.45\%$ for the pH4 electrolyte. The second electrolyte shows a high standard deviation, because the measurement of this sample was difficult to carry out but showed in general more than 90% of Co content. These SEM results indicate that the ferromagnetic layers of Sol_CoCu_pH4 will be more pure than the one of Sol_CoCu_pH2. First, the result of the Sol_Co_pH2 are described and then those of Sol_Co_pH4. The Sol_Co_pH2 did not show results as good as the Sol_Co_pH4. This is why the second electrolyte is optimised more deeply.

**CoCu pH2** Figure 3.20(a) shows the hysteresis loops for different magnetic layers for Sol_CoCu_pH2 in high porosity templates with 16 s of Cu layer deposition time. The 600 ms deposition time delivers the hysteresis loop with the most pronounced squareness while the other curves show more similar shapes with increasing coercive field and remanence magnetisation as the Co layers' thicknesses increase. Easy axis along the wire direction is expected for the Co solution with pH2 as it should adopt an fcc structure with major anisotropic contribution coming from the shape [8]. The homogeneous NWs show much larger coercive field and remanent magnetisation ($H_{c,OOP}$=1.1 kOe and $M_r/M_s$=0.58).

The IP GMR curves for the same samples are shown in figure 3.20(b). The 800 ms sample presents the best results. The 1000 ms one has a broader shape indicating that the antiparallel configuration is attained at larger field after passing the zero field than the two other samples. Table 3.7 shows the results found for the electrolyte Sol_Co_pH2. The $\Delta MR$ does not show the expected result as it decreases when the magnetic layer thickness increases.

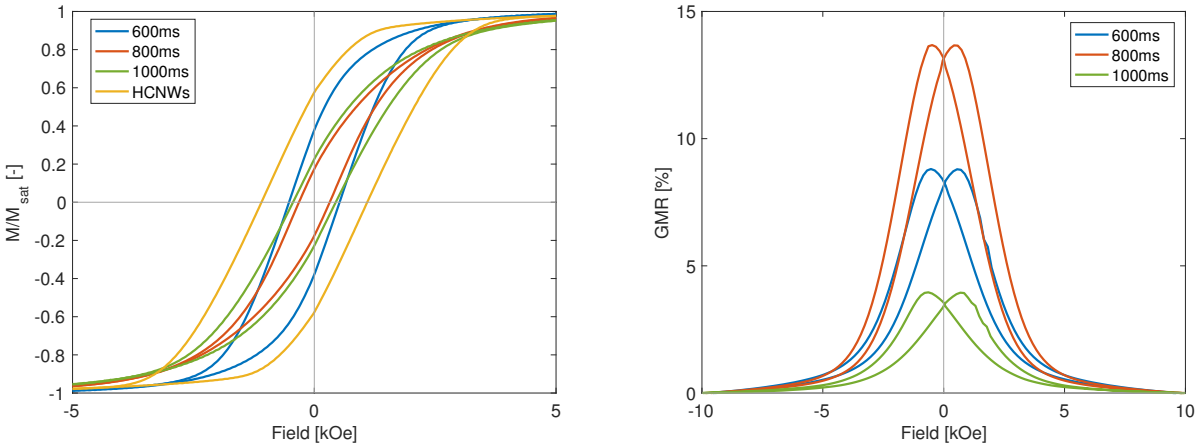


(a) OOP hysteresis loop direction

(b) IP GMR

FIGURE 3.20: Result of AGM and GMR for different NiCo layer deposition times (600 ms, 800 ms and 1000 ms) for the Sol_CoCu_pH2 in high porosity templates at RT. The Cu layer deposition time is 16 s. The hysteresis loop of the HCNWs is also depicted.

| Magnetic layer | $GMR_{IP}$ [%] | $\Delta$ MR [%] | $(M_r/M_s)_{OOP}$ [-] | $H_{c,OOP}$[kOe] |
|---|---|---|---|---|
| 600 | 8.81 | 0.56 | 0.38 | 0.52 |
| 800 | 13.68 | 0.34 | 0.18 | 0.32 |
| 1000 | 3.96 | 0.27 | 0.23 | 0.44 |

TABLE 3.7: Result of the $GMR_{IP}$, $\Delta MR$, $(M_r/M_s)_{OOP}$ and $H_{c,OOP}$ for different magnetic layer deposition time, for Sol_CoCu_pH2 in high porosity templates at RT. The Cu layer deposition time is 16 s.

**CoCu pH4** For this electrolyte (Sol_CoCu_pH4), the optimisation was done on both types of templates. First, in the "high porosity template section", different magnetisation layer deposition times are analysed. Then, in the low porosity template, both Co and Cu layers are optimised, and low temperature measurements are made on the best samples.

As a reminder, in the high porosity template used in this master thesis, NWs have a diameter of 80 nm while in the low porosity template, their diameter is 40 nm. Results suggest a relationship between the diameter of the deposited Co nanowires and their structural phase: for diameter larger than 40 nm, the structure of Co is hcp with and the c-axis can be oriented perpendicular to the wire [8] for electrolyte with pH4. This changes have consequences on the magnetic properties such a competition between the crystalline magnetic anisotropy along the c-axis perpendicular to the wire and the shape anisotropy which is along the axis of the wire. As a result, domain can be formed to reduce the magnetostatic and magnetocrystalline energies at the cost to create domain walls perpendicular to the axial direction. Domain wall propagation affect the magnetisation reversal properties and as a consequence reduce the coercive field and the remanent magnetisation [11].

Figure 3.21 compares two samples made on different templates with the electrolyte Sol_Co_pH4 and a deposition time of 800 ms and 16 s for the magnetic layer and Cu layer respectively. The first was made on a 80 nm 3% nanowire array and the second on a 40 nm 20% nanowire array. Both hysteresis loops (figures 3.21(b) and 3.29(b)) show easy axis of magnetisation in the OOP direction. However, differences in the shapes of the curves are observed. The sample with larger nanowire diameters has smaller remanent magnetisation $M_r/M_s = 0.194$ and smaller coercive field $H_c = 242,36$ kOe compared to $M_r/M_s = 0.365$ and $H_c = 522,84$ kOe for the sample with smaller

diameter in the OOP direction. This confirms the explanation given before: the shape anisotropy is more present for the smaller diameters. For larger NWs diameters, the MC anisotropy and the shape anisotropy are in competition, giving rise to a smaller coercive field. When looking at the general shape of the curve, the 80 nm - 20% porosity sample has very similar IP and OOP curves, showing isotropy. This is related to larger dipolar coupling when decreasing the distance between the wires. The GMR curves (figures 3.21(c) and 3.21(d)) show larger results for the low porosity sample, as expected. The IP GMR and OOP GMR curves are very similar for the high porosity sample, confirming the isotropic behaviour seen on the corresponding hysteresis loop.

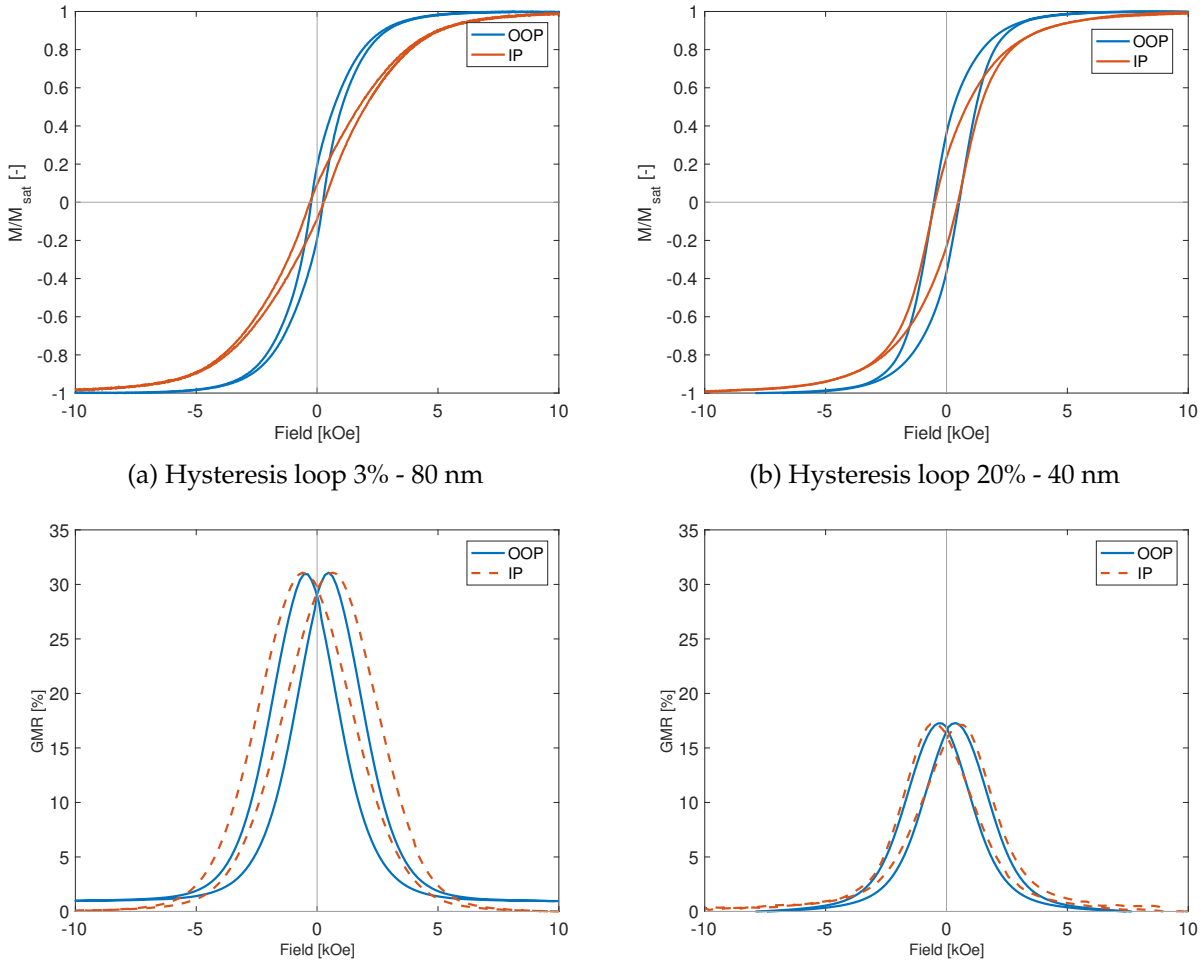


(a) Hysteresis loop 3% - 80 nm

(b) Hysteresis loop 20% - 40 nm

(c) GMR 3% - 80 nm

(d) GMR 20% - 40 nm

FIGURE 3.21: Comparison between low porosity and high porosity templates. Hysteresis loops and GMR curves in IP and OOP direction for the Sol_CoCu_pH4 at RT. The Cu layer deposition time is 16 s and magnetic layer deposition time 800 ms.

### 3.3.2 High porosity template

The Sol_CoCu_pH4 (and not the Sol_CoCu_pH2) is optimised more deeply for reasons explained before. For the high porosity template, only the magnetic layer thickness is optimised but a larger optimisation is done for the low porosity template.

### Optimisation of the magnetic layer

Figure 3.22 compares the results obtained for different magnetic layers (600 ms, 800 ms and 1200 ms) made from Sol_Co_pH4 on the high porosity template. In figure 3.22(a), a zoom of the hysteresis loop between -5 kOe and 5 kOe is given. The homogeneous sample shows the most pronounced squareness, indicating shape anisotropy. Then, the sample with a deposition time for the magnetic layer of 1200 ms is similar in shape with the homogeneous sample but shows a smaller coercive field and remanent magnetisation. The 800 ms sample shows a larger remanent magnetisation than the other MCNWs. The GMR curves in figure 3.22(b) show similar and good results for the 600 ms and 800 ms; for the thicker magnetic layer, a large decrease in GMR is observed.

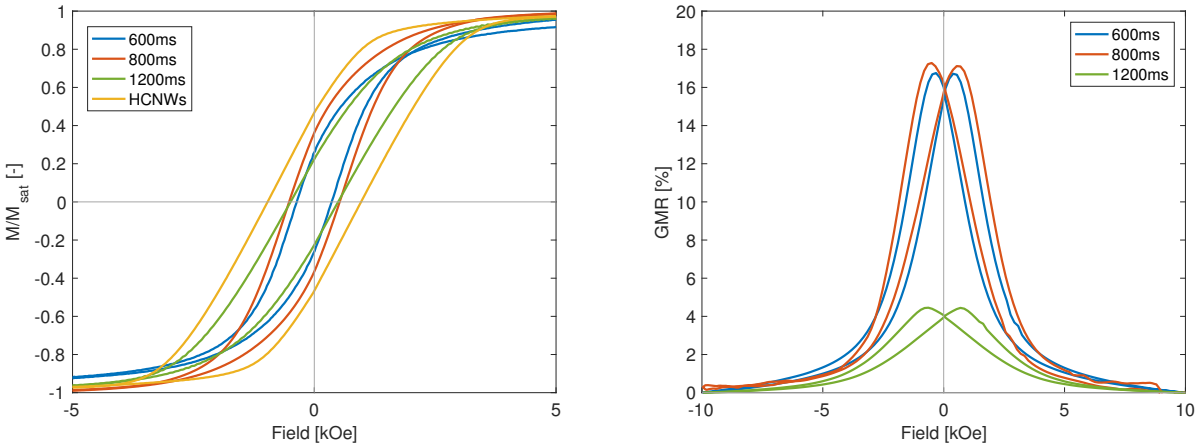


(a) OOP hysteresis loop

(b) IP GMR

FIGURE 3.22: Result of AGM and GMR for different NiCo layer deposition times (600 ms, 800 ms and 1200 ms) for the Sol_CoCu_pH4 in high porosity templates at RT. The Cu layer deposition time is 16 s. The hysteresis loop of the HCNWs is also depicted.

Figure 3.23 shows the hysteresis loop of the sample with 600 ms magnetic layer deposition time in IP and OOP direction between $-10$ kOe and $+10$ kOe. The isotropic behaviour can directly be observed. Hysteresis loops of both directions for 1200 ms deposition time are also given in figure 3.24. It shows a strange behaviour, as the coercive field in IP direction is larger than in OOP direction while the magnetisation saturation is attained faster for the OOP direction. Table 3.8 gives the results found for the analysis of Sol_Co_pH4 in the high porosity template.

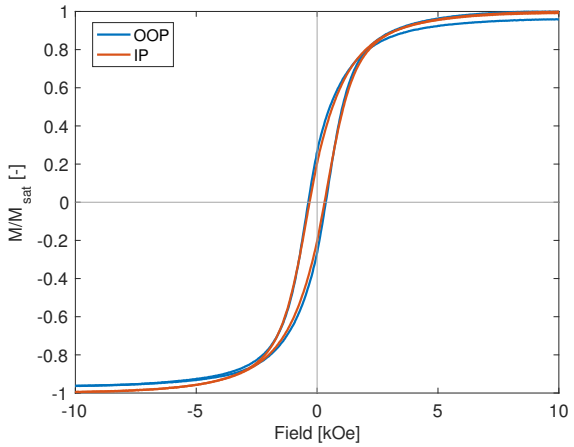


FIGURE 3.23: OOP and IP hysteresis loops for Sol_Co_pH4 in high porosity template. The Co layer deposition time is 600 ms and Cu layer 16 s.

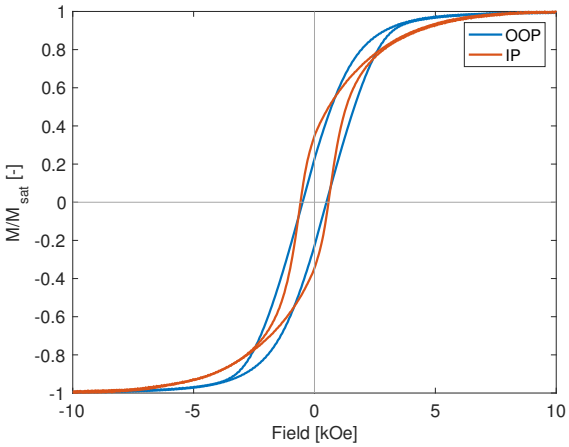


FIGURE 3.24: OOP and IP hysteresis loops for Sol_Co_pH4 in high porosity template. The Co layer deposition time is 1200 ms and Cu layer 16 s.

| Magnetic layer [ms] | $GMR_{IP}$ [%] | $\Delta$ MR [%] | $(M_r/M_s)_{OOP}$ [-] | $H_{c,OOP}$[kOe] |
|---|---|---|---|---|
| 300 | 6.23 | 0.25 | 0.02 | 0.02 |
| 600 | 16.75 | 0.25 | 0.26 | 0.36 |
| 800 | 17.51 | 0.20 | 0.37 | 0.52 |
| 900 | 17.23 | 0.09 | 0.23 | 0.33 |
| 1200 | 4.45 | 0.48 | 0.23 | 0.49 |

TABLE 3.8: Results of the $GMR_{IP}$, $\Delta MR$, $(M_r/M_s)_{OOP}$ and $H_{c,OOP}$ for different magnetic layer deposition time, for Sol_CoCu_pH4 in high porosity templates at RT. The Cu layer deposition time is 16 s.

For the GMR inside the high porosity template, for a deposition time of 600 ms for the magnetic layer and 16 s for the Cu layer, an impressive value of $27.96\%$ is obtained. When fabricating this sample again to get statistics, the result could not be reproduced. On average, $16\%$ of GMR was obtained. The GMR results of this sample are indicated as an isolated point on the different plots of figure 3.26. Because this sample gave a really good result, the GMR measurement of this sample was also performed at low temperature (15K); $40.46\%$ and $39.27\%$ GMR was measured in IP and OOP configurations, respectively, as shown in figure 3.25(b). This result shows a lower temperature dependence of the Co ferromagnetic layers compared to the alloys studied in the previous sections, which showed doubled GMR results when going to low temperature. The hysteresis loop (3.25(a) corresponding to this particular sample shows a similar behaviour for the IP and OOP around zero field, but the IP magnetisation saturation is attained more rapidly. This suggests the presence of a c-axis perpendicular to the NWs.

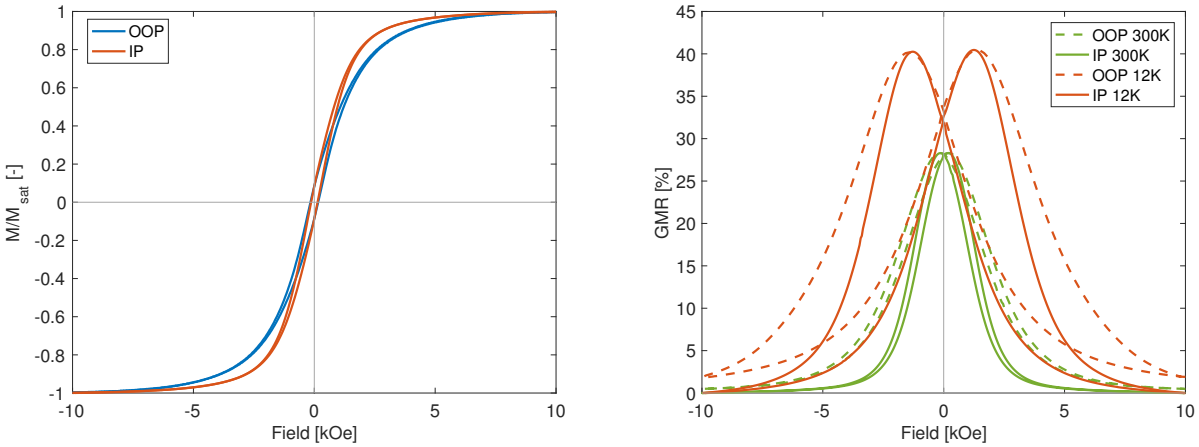


(a) Hysteresis loops

(b) GMR at RT and LT

FIGURE 3.25: Results of AGM and GMR for the sample with impressive GMR result; made from Sol_CoCu_pH4 in high porosity templates. The Cu layer deposition time is 16 s and magnetic layer deposition time is 600 ms.

Figures 3.26(a) and (b) summarise the results found for the coercive field and normalised remanent magnetisation. An increase is observed until 800 ms, which is expected. Then, particular results appear: first a decrease in both coercive field and remanence magnetisation at 900 ms; then, for 1200 ms, the curves of OOP and IP intersect, showing higher results of $H_c$ and $M_r/M_s$ in the IP direction. Figure 3.24 illustrates this particular hysteresis loop. The results for HCNWs are higher, as expected.

The GMR results, illustrated in figure 3.26(c), show a plateau between 700 ms and 900 ms of magnetic layer deposition time. Then, the GMR decreases. The $\Delta MR$ in figure 3.26(d) presents really small values, which is related to the isotropic behaviour shown in figure 3.23.

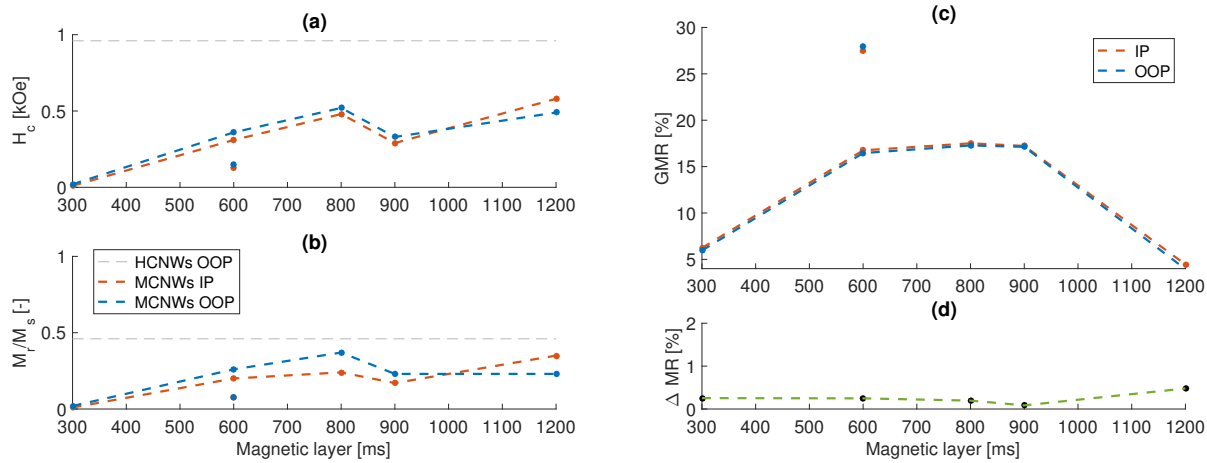


FIGURE 3.26: (a) Coercive field; (b) Normalised remanent saturation; (c) GMR ; (d) ΔMR as a function of magnetic layer deposition time, for Sol_CoCu_pH4 in high porosity template at RT. Cu layer deposition time is 16 s.

### 3.3.3 Low porosity template

Once the high porosity template is optimised, the low porosity template is analysed and optimised. First, the magnetic layer is optimised. The relationship between deposition time and magnetic layer thickness is studied; finally the Cu layer thicknesses are optimised.

### Optimisation of the magnetic layer

Figure 3.27 compares the magnetic and GMR results for magnetic layers of 700 ms, 900 ms and 1200 ms deposition times with Sol_Co_pH4 and the low porosity template. The different hysteresis loops show similar shapes. They are thin with low coercive field and small remanent magnetisation. When the magnetic layer's thickness increases, the shape becomes more vertical (higher remanent magnetisation), which is the same behaviour as for parallel NWs arrays. The GMR curves look similar as they are not very broad, with a higher result at 700 ms. Table 3.9 gives some numeric values of the magnetic and magnetotransport measurements of the fabricated samples to do the magnetic layer optimisation in the low porosity templates for Sol_CoCu_pH4.

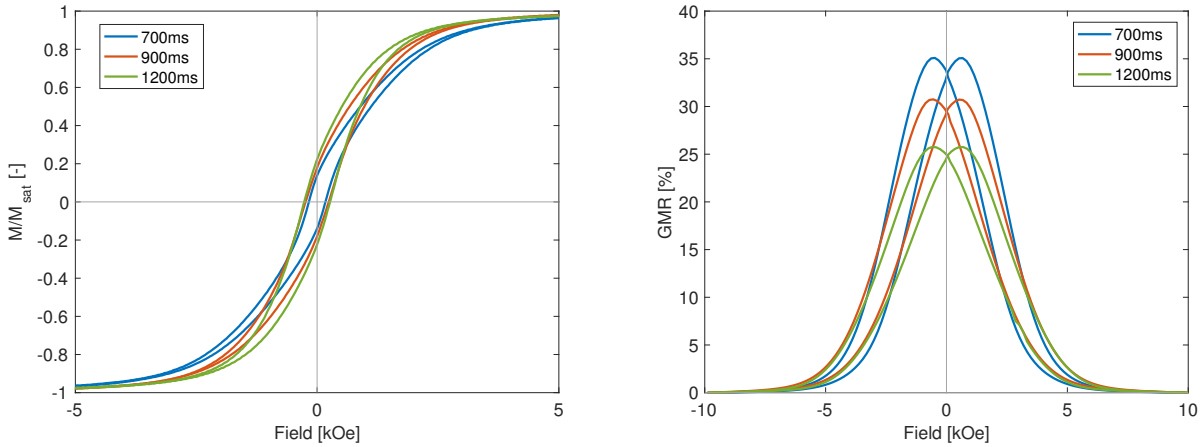


(a) OOP hysteresis loop (b) IP GMR

FIGURE 3.27: Result of AGM and GMR for different NiCo layer deposition times (700 ms, 900 ms and 1200 ms) for the Sol_CoCu_pH4 in low porosity templates at RT. The Cu layer deposition time is 16 s.

| Magnetic layer [ms] | $GMR_{IP}$ [%] | $\Delta$ MR [%] | $(M_r/M_s)_{OOP}$ [-] | $H_{c,OOP}$[kOe] |
|---|---|---|---|---|
| 600 | 14.49 | 0.18 | 0.16 | 0.24 |
| 700 | 35.09 | 0.83 | 0.14 | 0.17 |
| 800 | 31.08 | 1.53 | 0.19 | 0.24 |
| 900 | 30.75 | 2.00 | 0.18 | 0.24 |
| 1000 | 29.77 | 2.08 | 0.21 | 0.25 |
| 1200 | 25.76 | 3.23 | 0.17 | 0.24 |
| 1500 | 9.74 | 0.91 | 0.20 | 0.23 |
| 2000 | 9.48 | 4.31 | 0.25 | 0.31 |
| 2500 | 4.45 | 0.48 | 0.36 | 0.37 |

TABLE 3.9: Result of the $GMR_{IP}$, $\Delta MR$, $(M_r/M_s)_{OOP}$ and $H_{c,OOP}$ for different magnetic layer deposition times, for Sol_CoCu_pH4 in high porosity templates at RT. The Cu layer deposition time is 16 s.

Figure 3.28(a) illustrates the evolution of the coercive field when the magnetic layer increases for Sol_CoCu_pH4 in the low porosity template. A big difference between this plot and the previous ones illustrating the evolution of $H_c$ in this section is that the curve of $H_c$ in the IP direction is sometimes higher than $H_c$ in the OOP direction, and that for the HCNWs the $H_c$ is much lower than for MCNWs. This behaviour corroborates the possible presence of an easy magnetisation

perpendicular to the wires' direction in NWs with larger diameters. Figure 3.28(b) shows an increase of remanent magnetisation as the magnetic layer increases, which is expected.

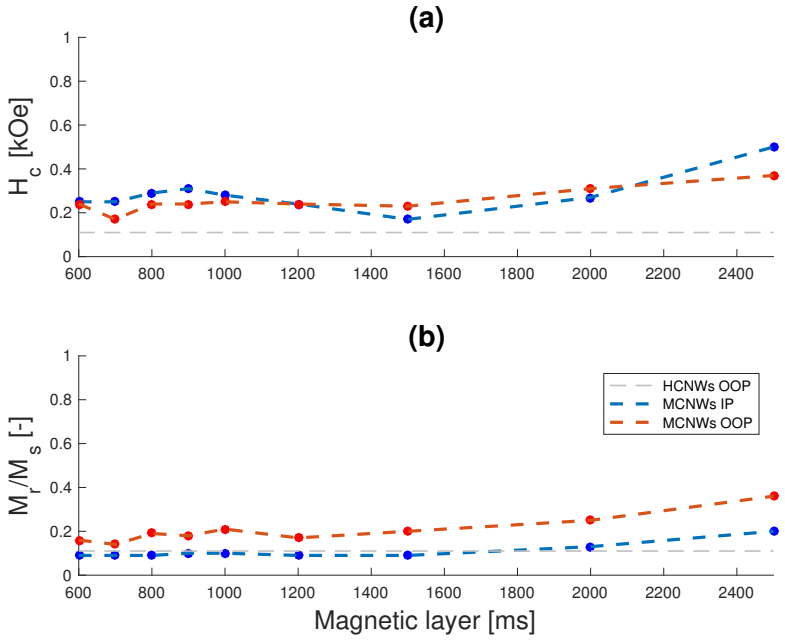


FIGURE 3.28: (a) Coercive field and (b) normalised remanent saturation as a function of magnetic layer deposition time, for Sol_CoCu_pH4 in low porosity template at RT. Cu layer deposition time is 16 s.

To better understand and show this change of magnetic properties in the low porosity templates with larger diameter, hysteresis loops in IP and OOP directions with increasing magnetic layer thickness are shown in figure 3.29. A large increase of the magnetic anisotropy as the Co layer thickness increases is observed. When $t_{Co}$ increases, for IP hysteresis loops, the saturation magnetisation is reached at higher field; on the opposite the saturation magnetisation is reached at lower field in the OOP direction when $t_{Co}$ increases. Easy magnetisation direction along the wires' axis are reinforced for larger magnetic layers. Thinner magnetic layers seem to favour the direction perpendicular to the wires' axis as an easy magnetisation direction [12].

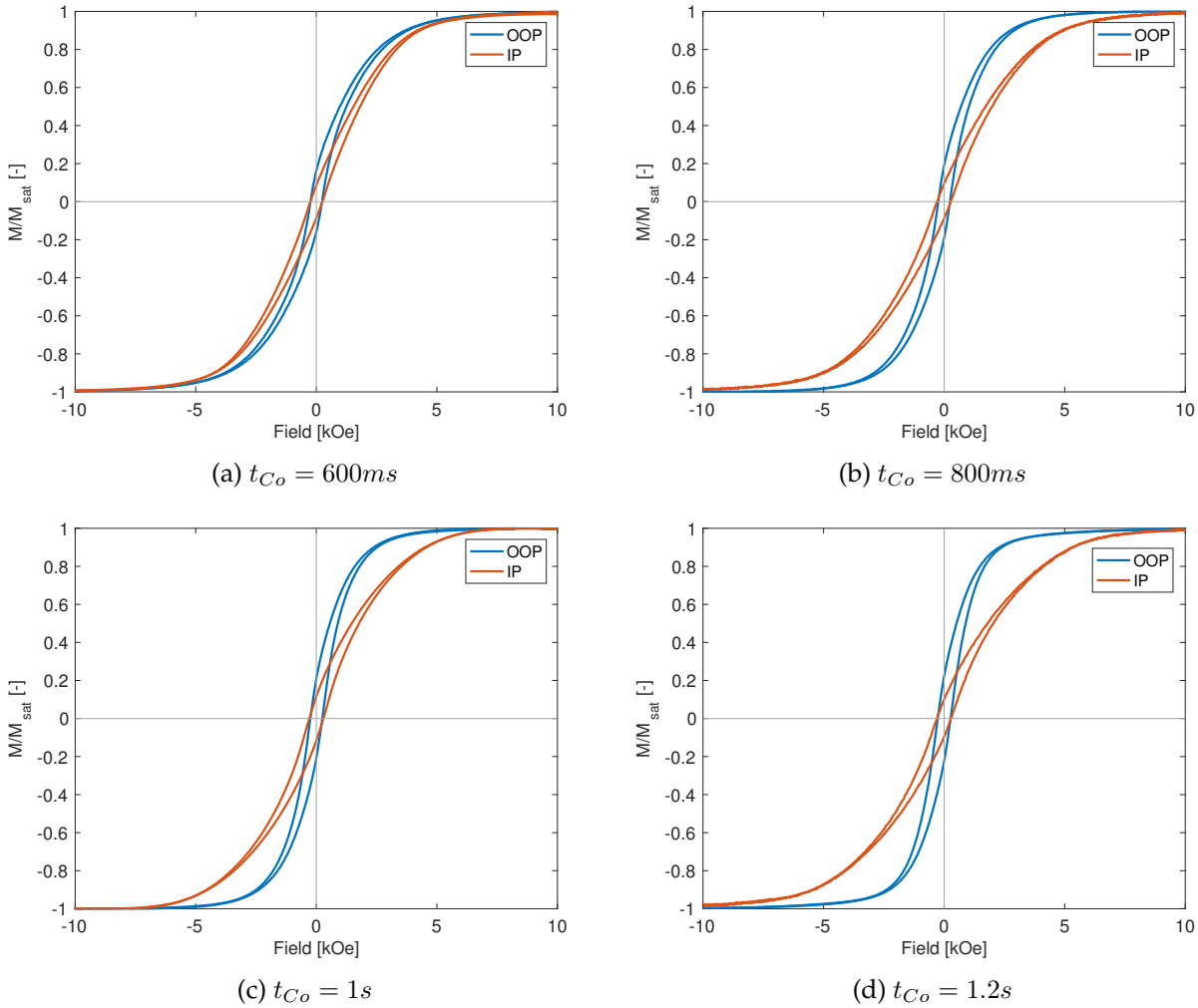


(a) $t_{Co} = 600ms$ (b) $t_{Co} = 800ms$

(c) $t_{Co} = 1s$ (d) $t_{Co} = 1.2s$

FIGURE 3.29: Hysteresis loops for various magnetic layer deposition times for Sol_CoCu_pH4 in low porosity template at RT. Cu layer deposition time is 16 s.

Figure 3.30 illustrates the GMR results as a function of the magnetic layer deposition time for Sol_CoCu_pH4 in the low porosity template at RT and Cu layer deposition time of 16 s. A peak is observed at 700 ms, but a general plateau with satisfying values is observed between 700 ms and 1000 ms. For higher deposition times, the GMR decreases. The $\Delta MR$ increases until 1200 ms and then shows a strange behaviour with low values at 1500 ms and 2500 ms.

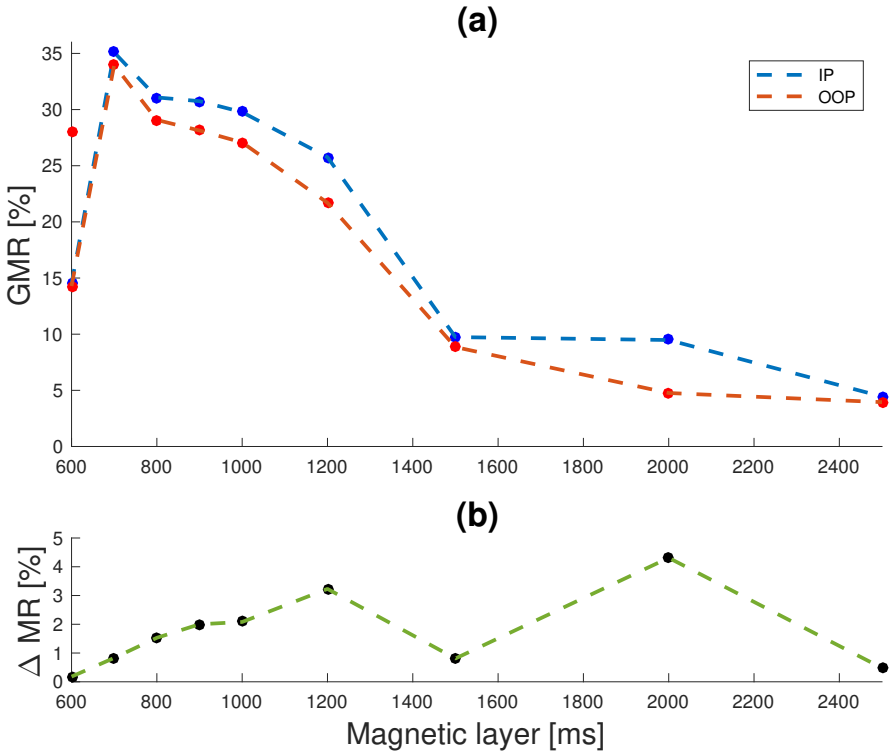


FIGURE 3.30: GMR and ΔMR as a function of magnetic layer deposition time, for Sol_CoCu_pH4 in low porosity template at RT. Cu layer deposition time is 16 s.

### Analysis of the deposition time and layer thickness

To check if the VF model (equation (1.6), page 25) could have been applied to the previous GMR result, the thickness of the layers is calculated. This can be done by observing the time at which the electrodeposition starts to overfill, as explained in section 2.1, page 49. Table 3.10 shows the deposition current as a function of the time. As can be seen, it is not easy to determine the exact time at which the overfilling appears. The calculations below are thus approximations, and should be considered as such.

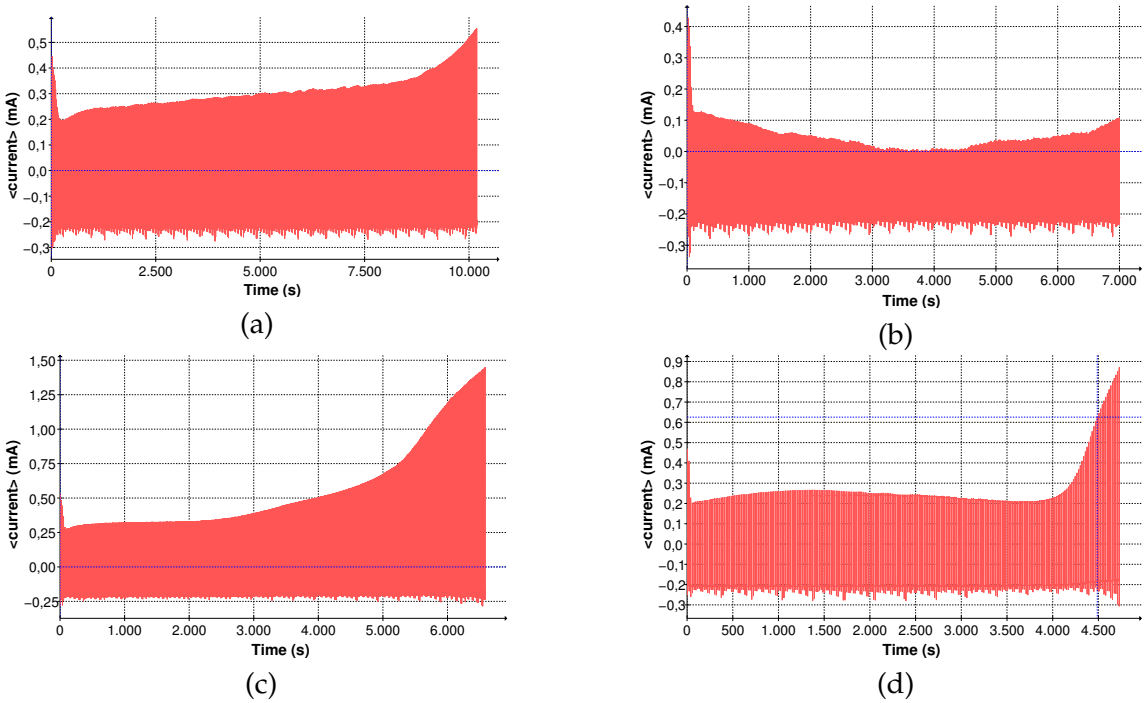


TABLE 3.10: Deposition current in samples made from Sol_CoCu_pH4 on the low porosity template. The deposition time of the Cu layer is 16 s and the deposition time of the magnetic layer is 1 s (a), 1.5 s (b), 2 s (c), 2.5 s (d).

Four samples with increasing magnetic layer deposition times (1 s, 1.5 s, 2 s, 2.5 s) were selected. For a magnetic layer of 1000 ms, overfilling is obtained at $\sim 8500$s; for 1500 ms, overfilling at $\sim 7000$s; for 2000 ms, at $\sim 5200$s and for 2500 ms, overfilling at $\sim 4100$s. When applying the formula given in this previous section, the results given in table 3.11 are obtained. One can notice that when the deposition time of the magnetic layer increases, the number of layers decreases really fast due to the high concentration of Co inside the electrolyte.

| Magnetic layer [ms] | Time at overfilling [s] | Number of layers | Height of a bilayer [nm] |
|---|---|---|---|
| 1000 | 8500 | 500 | 48.54 |
| 1500 | 7000 | 400 | 60.68 |
| 2000 | 5200 | 288 | 84.27 |
| 2500 | 4100 | 222 | 109.32 |

TABLE 3.11: Summary of the number of layers for different samples with different deposition times for the magnetic layers.

To determine the thickness of the Cu layer and the Co layer inside the bilayer, 4 equations are taken with two unknowns:

$$\begin{cases} 48.54 = t_{Cu} + t_{Co} \\ 60.68 = t_{Cu} + 1.5t_{Co} \\ 84.27 = t_{Cu} + 2t_{Co} \\ 109.32 = t_{Cu} + 2.5t_{Co} \end{cases}$$

with $t_{Cu}$ and $t_{Co}$ the thickness of the Copper layer and Cobalt layer respectively. For the Cu layer, a thickness of 3.627 nm (deposed during 16 s) is found. For Co, a thickness of 41.19 nm (deposed during 1 s) is obtained. Typically, the spin diffusion length in Cobalt is around 60 nm [36]. As a consequence the fit of the VF model should have been started at 1500 ms and would have implied only three samples for the fit, which is not sufficient and objective.

### Optimisation of the deposition time of the Cu-layer

The optimisation of the magnetic layer shows that good GMR results are obtained between 700 ms and 1000 ms. The 800 ms layer is chosen as laying in the middle of this plateau. This result is fixed and different Cu layer deposition times are tested in order to look how the magnetic properties and GMR change with the Cu layer thickness. Figure 3.31(a) shows the hysteresis loops in OOP for 12 s, 20 s and 24 s of Cu layer deposition time for Sol_CoCu_pH4 in the low porosity template. The 12 s and 24 s loops are very similar and more squared than the 20 s which reaches its saturation magnetisation at a larger applied magnetic field. Figure 3.31(b) compares the IP GMR curves for the same samples. The curves present the same shape and the 20 s shows the best result. Table 3.12 gives some numeric values of the measured magnetic and magnetotransport properties of the different samples elaborated to optimise the Cu layer.

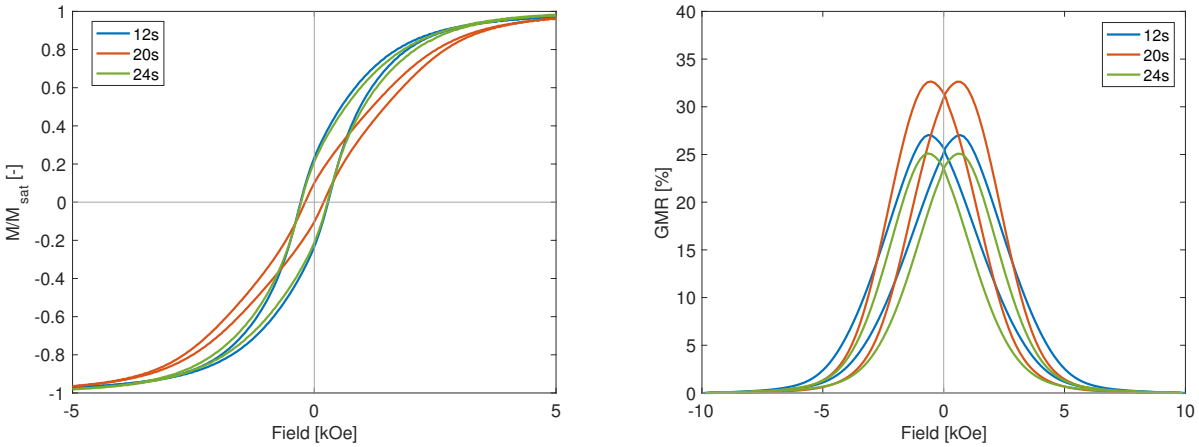


(a) OOP hysteresis loop

(b) IP GMR

FIGURE 3.31: Result of AGM and GMR for different Cu layer deposition time (12 s, 20 s, 24 s) for the Sol_CoCu_pH4 in low porosity templates at RT. The NiCo layer deposition time is 800 ms.

| Cu-layer [s] | $GMR_{IP}$ [%] | Δ MR [%] | $(M_r/M_s)_{OOP}$ [-] | $H_{c,OOP}$[kOe] |
|---|---|---|---|---|
| 12 | 27.04 | 1.33 | 0.23 | 0.28 |
| 16 | 31.08 | 1.53 | 0.19 | 0.24 |
| 20 | 32.65 | 1.10 | 0.1 | 0.19 |
| 24 | 25.1 | 1.19 | 0.21 | 0.27 |

TABLE 3.12: Result of the $GMR_{IP}$, $(M_r/M_s)_{OOP}$ and $H_{c,OOP}$ for different deposition times of the Cu-layer for the CoCu pH4 electrolyte in the 3%-80nm template for a magnetic layer deposition time of 800 ms.

Figure 3.32(a) and (b) illustrate the evolution of the coercive field and normalised remanent magnetisation as a function of the Cu layer thickness for Sol_CoCu_pH4 in low porosity templates with 800 ms of NiCo layer deposition time. The coercive field is higher in the IP direction than for the previous samples made on the low porosity template. The coercivity and remanent magnetisation decrease as the magnetic layer thickness increases, which is expected. The 24 s sample only has an OOP measurement because the IP measurement could not be carried out, probably due to the low magnetic content. Moreover, this sample shows an unexpected increase on both plots.

The GMR results are illustrated in figure 3.32(c). The GMR increases until 20 s. This suggests that larger non-magnetic layers can be made. This is probably linked to the larger spin diffusion length in Cobalt. The $\Delta MR$ illustrated in figure 3.32(d) shows a slight decrease when the Cu layer thickness increases which is the expected behaviour.

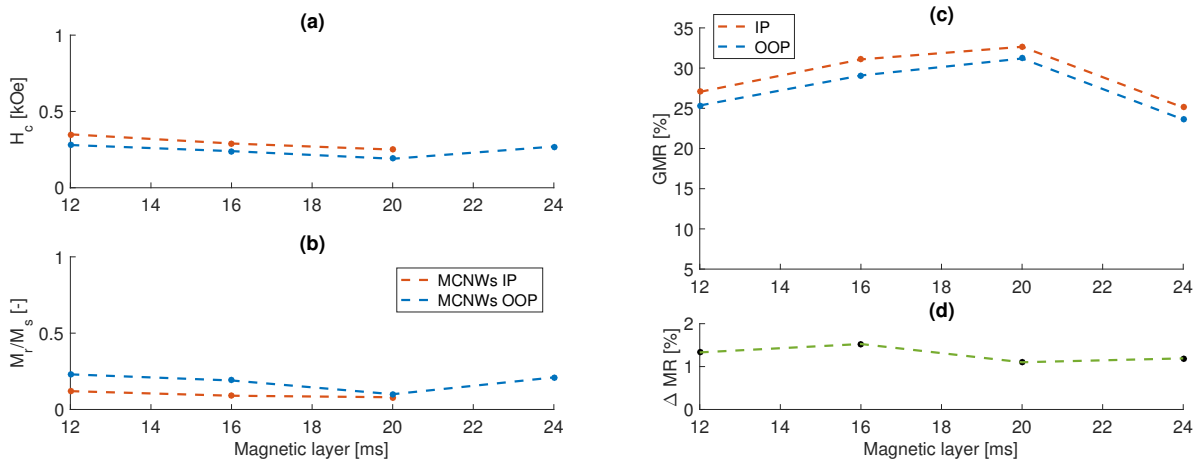


FIGURE 3.32: (a) Coercive field; (b) normalised remanent saturation; (c) GMR ; (d) ΔMR as a function of Cu layer deposition time, for Sol_CoCu_pH4 in low porosity template at RT. NiCo layer deposition time is 800 ms.

**Low temperature measurement**

The samples showing the best results were analysed at low temperature. As a consequence the 700 ms and 800 ms magnetic layers with 16 s of Cu layer deposition time were chosen. The 800 ms Co and 20 s Cu layer deposition time could have been chosen too, but as the result was close to the 800 ms Co and 16 s Cu, only these two samples were analysed at low temperature.

Figure 3.33 compares the GMR measurement at RT and LT of the 700 ms Co and 16 s Cu sample. The IP GMR result is 47.5% at LT compared to 31% at RT. As seen for the high porosity templates (section 3.25,page 82), the increase of GMR at LT is not as high as for NiCo alloys, which suggests that Co ferromagnetic layers are less affected by magnons scattering; indeed previous studies showed the weak temperature dependence of the spin asymmetry coefficient in Co layers [17]. The peaks of the GMR curves are closer from the zero field at RT than at LT. This shows that perfect antiparallel alignment is reached at a stronger magnetic field after passing the zero field. The $\Delta MR$ is $1.37\%$ at LT compared to 1.53% at RT. Results in literature already showed that the AMR of Co ferromagnetic layers decreases as the temperature decreases (see figure 3.2).

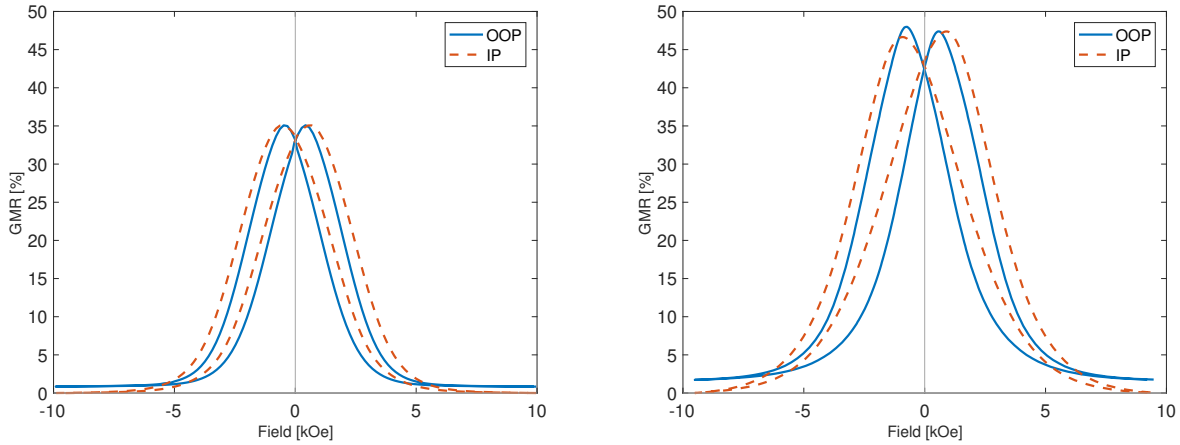


(a) T∼300K (b) T∼12K

FIGURE 3.33: GMR curves at different temperatures for the Sol_NiCoCu_0.4M in low porosity templates. The NiCo layer deposition time is 700 ms and Cu layer deposition time 16 s.

Figure 3.34 compares the IP GMR measurement of the 800 ms Co and 16 s Cu sample at RT and LT. The LT measurement of this samples shows a minimum temperature of 20K (and not 12K) because another set up where 20K is the lowest possible temperature was used for this measurement. The 800 ms shows better results than the 700 ms, with a $GMR_{IP}$ of 57.43% compared to 47.37% for the 700 ms while at RT the 700 ms showed higher results.

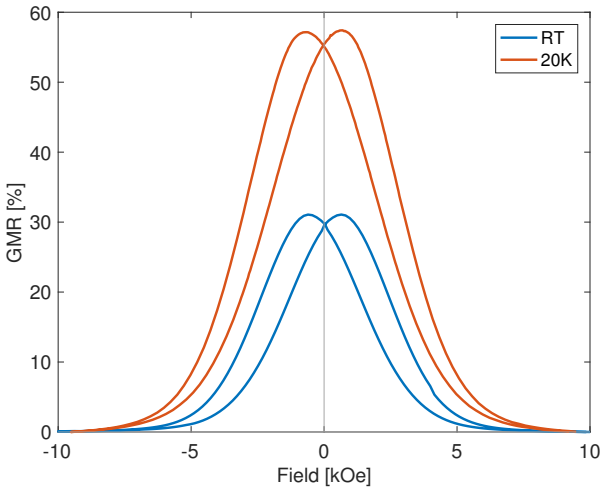


FIGURE 3.34: Low temperature measurements in IP direction. 700 ms and 800 ms of magnetic layer deposition time.

The fact higher GMR results at 20K for the 800 ms than at 12K for the 700 ms are obtained, could be related to the weak localisation phenomenon. Indeed, at temperatures close to 0K, the probability of backscattering increases and as a consequence tends to localise electrons and increase the resistance at LT [28].

## 3.4 Summary of the magnetotransport results

To conclude, a plot is given with the obtained results for increasing Co concentration in figure 3.35. Below 50% of Cobalt, Kyara Hallet made the analysis, while this work started from 50%. This final curve tells us that the Ni/Cu combination does not give good results. When the Co content is increased, the GMR increases until a $Ni_{50}Co_{50}$ alloy is reached. For this ratio, the effect of the temperature is really important. Indeed, when passing from RT to LT for the low porosity template the GMR results almost triple. Then, when the Co content increases to $Ni_{20}Co_{80}$, a general decrease is observed. The decrease is more marked for the low temperature measurement. Finally, for 100%

Co ferromagnetic layers, the RT measurements increase, while the LT measurements decrease compared to the previous ratio. This suggests that at RT, Co is a good material for ferromagnetic layers but when going to lower temperatures the NiCo alloy presents much more possibilities to get higher GMR.

The 'x' marks in figure 3.35 show the results of the previous thesis. They are always higher. Indeed, more concentrated electrolytes were used. The electrolyte of the previous thesis seems to be more optimal but was very instable, and often showed random results. Here, most of the time the samples do not show problems and give coherent results.

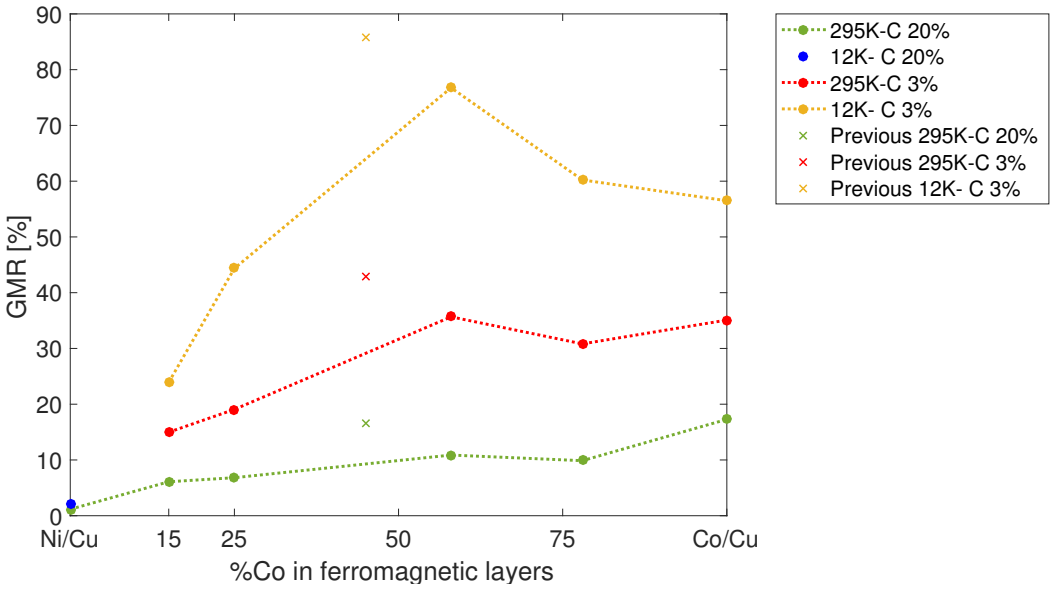


FIGURE 3.35: Evolution of the GMR result with the Cobalt content in the ferromagnetic layer. The 'x' marks show the result found in the previous thesis [44].

Figure 3.36 shows the evolution of the ΔMR (∼AMR) as a function of the Co content. When comparing this figure to the figure from the literature 3.2, page 63, a large similitude can be observed. This corroborates the fact that AMR is also present in MCNWs. The MCNWs show the same trend as HCNWs but with a slight decrease between the AMR of the HCNWs and the ΔMR of the MCNWs. The ΔMR is slightly under estimated compared to the AMR due to the assumption made at the beginning of this section $R_{max} \simeq R_{OOP}$. However, the condition $GMR \gg \Delta MR$ is always respected, assuring that the GMR measurement makes sense.

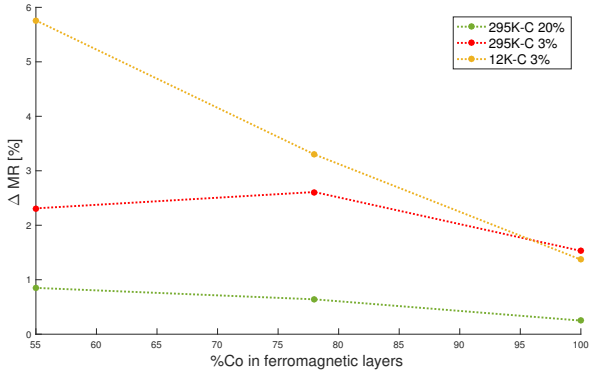


FIGURE 3.36: Evolution of the ΔMR results with the Cobalt content in the ferromagnetic layer.

# Conclusion and perspectives

Several magnetic and magnetotransport measurements presented in this master thesis give interesting results for further studies. Thanks to the simple and straightforward electrodeposition fabrication technique on PC templates, the nanowire networks could be easily elaborated. The NWs are grown by adapting the deposition potential (already optimised in previous studies [44]) and the deposition time. This technique allows for CPP-GMR measurements, which present much higher results than CIP-GMR. To obtain crossed nanowires, the polycarbonate membrane appears to be an appropriate template candidate: the pores are made from a sequential irradiation technique, which allows to vary the irradiation angles. The main advantage of this type of template is its versatility, as it allows to tune various geometric parameters including the NWs size, density and orientation. Furthermore, the CNWs configuration allows for mechanical stability, a self supporting structure and an increased electrical connectivity.

To grow NWs that enable efficient GMR results, an appropriate electrolyte should be found. The objective of this master thesis was to study multilayers composed of Cu non-magnetic layers and NiCo ferromagnetic layers where the NiCo ratio varied between 50%Ni-50%Co until 100%Co. Previous studies found an adapted Cu concentration with respect to the Ni and Co concentration in the electrolyte [44]. First, more concentrated electrolytes (2.3M Ni 0.4M Co 15mM Cu) were made. These gave unsatisfying results, as the templates' pores were blocked, resulting in inhomogeneous nanowire network. More diluted electrolytes with 1M of Ni, 0.2M of Co and 7.5mM of Cu were elaborated. The results were much more stable and showed homogeneous depositions. The Ni and Cu were thus fixed at these concentrations while the Co concentration was made to vary, to study its impact on the GMR results. Three electrolytes corresponding to three different NiCo ratios were finally selected and optimised: Sol_NiCoCu_0.17M (1M of Ni, 0.17M of Co and 7.5mM of Cu), Sol_NiCoCu_0.4M (1M of Ni, 0.4M of Co and 7.5mM of Cu) and Sol_CoCu_pH4 (0.17M of Co and 7.5mM of Cu). The ratio of NiCo inside the layers could be calculated thanks to SEM analyses. For the two first electrolytes, these gave: 42%Ni-58%Co, 22%Ni-78%Co with $\sim 10\%$ and $9\%$ of Cu present inside the ferromagnetic layers, respectively. In the 100% Co ferromagnetic layers, a 10% of Cu was found, on average.

The next step was to optimise the thickness of the ferromagnetic and non magnetic layers. To do so, the ferromagnetic layer deposition time was first optimised while the non-magnetic layer was fixed with a reasonable value from the literature [44], [9]. Then, the best result for the magnetic layer was kept and the non-magnetic layer was varied. For the Sol_NiCoCu_0.17M and Sol_NiCoCu_0.4M, an optimal GMR result was found for 600 ms of NiCo deposition time and 16 s of Cu deposition time. For the Sol_CoCu_pH4, better results were obtained for larger layers: between 700 ms and 800 ms for the magnetic layer and between 16 s and 20 s for the Cu layer. This result proves a larger spin diffusion length in Cobalt.

GMR measurements of MCNWs made on templates with different pore densities and pore sizes were compared. Results at RT show that the density of the NWs has a great influence on the GMR results, ranging from 11% in the high porosity template to 36% in the low porosity template for Sol_NiCoCu_0.17M. The effect is less pronounced for an increased Co content: 17.5% to 31%. This indicates that at high porosity, the MCNWs made of Co ferromagnetic layers are better suited; at

lower porosity, the NiCo composition takes over. The intersections constitute an obstacle to good GMR results, as the multilayers are not well formed and tend to favour domain wall formation in this region. Reducing the number of intersections is thus a key-point and this is done by reducing the porosity. The magnetic properties are also influenced by the porosity, as the dipolar coupling between the NWs is much greater for higher porosity templates, resulting in more isotropic hysteresis loops. The NWs diameter does not have a large effect on the magnetic and magnetotransport properties for the NiCo ferromagnetic layers, as for both types of diameter studied – 40 nm and 80 nm – the material remains mono-domain. Only the shape anisotropy was more marked for the 40 nm diameter. Then again, this was counter-balanced by the larger dipolar coupling coming from the larger porosity of this kind of template. However, for the Co ferromagnetic layers, changes in the magnetic properties were observed when larger diameters of NWs were used. The MC anisotropy could be observed with easy axis laying preferentially perpendicular to the NWs axis.

The best samples of each electrolyte were analysed at low temperature. This allowed to look at the effect of magnons scattering. Results show a large increase of GMR result, but similarly as for the transition from high to low porosity, the effect of temperature change is more marked for the Sol_NiCoCu_0.17M than for the Sol_CoCu_pH4, going from 36% to 76% and from 31% to 57.43% respectively. The Sol_NiCoCu_0.4M shows a result in between, going from 31% to 60%.

AMR effect has also been studied, as this effect was present in the fabricated MCNWs. The low porosity templates are more affected by this effect than the high porosity ones. The temperature also affects the AMR. An increase of AMR is observed in NiCo/Cu MCNWs at LT, while the opposite effect is observed in Co/Cu MCNWs. The same effect has been observed in HCNWs in previous studies [7].

Previous CPP-GMR measurements on MCNWs NiCo/Cu have obtained better results. The electrolyte was more concentrated, enhancing the purity of the layers as a consequence. However, the good results were difficult to reproduce reliably, due to inhomogeneous electrodeposition. In this master thesis, this inconvenience was eliminated. Further studies could be made to improve the purity inside the layers, as the $Ni_{50}Co_{50}$ alloy appears to be a promising candidate for high CPP-GMR measurement. Another element that could be changed is the type of template. Aluminum Oxide is known to generally deliver better results [16], [34]. However, making CNWs in this material would be a new challenge. Another solution could be to improve the template by finding a polymer with less hydrophobic properties and better diffusion behaviour of the reactive species of the electrolyte in the membrane.

A last important point to consider when discussing research about the materials used in this master thesis, cobalt in particular, is their origin. In the last 30 years, worldwide cobalt demand has surged dramatically. High technology industries in various domains such as rechargeable batteries, superalloys or catalyst use more and more cobalt [42]. In the Democratic Republic of Congo, specifically, studies reveal the human health impact of the current mining. The populations, and particularly the children living close to the mines, face high exposure to several metals and present various health problems as a consequence [3]. The large increase in cobalt exploitation leads to serious ethical and economical concerns including child labour, illegal mining operations, life-threatening working conditions and corruption. Unfortunately Ni and Cu face the same challenges, although at a lower scale. In the future, this crucial aspect should be taken into account, for example by trying to reduce the amount of Co used in our materials.

# Appendices

# Appendix A

# Appendix A

## A.1 Diamagnetism and paramagnetism

Each atom is a many-electron system. A homogeneous magnetic field acts on the orbital motion and the spins of the electron. The kinetic part of the hamiltonian of an independent atom can be described as[27]:

$$\mathcal{H} = \frac{p^2}{2m} + \frac{e\hbar}{2m} \cdot \overrightarrow{l} \cdot \overrightarrow{B} + \frac{e^2}{8m}(\overrightarrow{r} \times \overrightarrow{B})^2 \quad [\,\mathrm{J}\,] \tag{A.1}$$

In equation (A.1), the first term counts for the mechanical kinetic energy, the second term is the paramagnetic contribution and the last term of the sum represent the diamagnetic contribution.

#### Diamagnetism

Diamagnetism is associated with the tendency of electrical charges partially to shield the interior of a body from an applied magnetic field. It tends to oppose the flux change. The hamiltonian of this contribution can be described as:

$$\mathcal{H}_{dia} = \sum_{i=1}^{n} \frac{e^2}{8m}(\overrightarrow{B} \cdot \overrightarrow{r_i})^2 \quad [\,\mathrm{J}\,]$$

Knowing that the link between the energy and the magnetic moment is $\mu_{dia} = -\frac{\delta E_{dia}}{\delta B}$, the magnetic moment is found to be

$$\mu_{dia} = -\frac{\mu_0 N Z e^2}{6m} < r^2 > \quad [\mathrm{A{\cdot}m^2}]$$

And the suceptibility can be find by knowing that $\chi_{dia} = \mu_0 \frac{M_{dia}}{B}$. This results in:

$$\chi_{dia} = -\frac{N}{V}\frac{\mu_0 e^2}{6m} Z < r^2 > \quad [\,\text{-}\,]$$

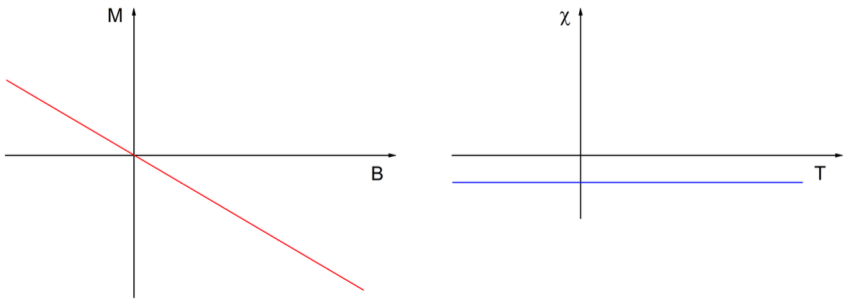


FIGURE A.1: Left: diamagnetic magnetisation as a function of applied magnetic field. Right: diamagnetic susceptibility as a function of temperature. [27]

**Paramagnetism**

In the case of free ions, the hamiltonian for the paramagnetism contribution is described as:

$$\mathcal{H}_{para} = \sum_{i=1}^{N} \mu_b(\overrightarrow{L_i} + g\overrightarrow{S_i}) \cdot \overrightarrow{B} = g_j \mu_B J_z B \quad [\,\mathrm{J}\,]$$

where $\mu_b = \frac{e\hbar}{2m_e}$ is the Bohr magneton, $\overrightarrow{L_i}$ is the orbital angular momentum, $\overrightarrow{S_i}$ is the spin angular momentum, $\overrightarrow{J_i}$ the total angular momentum and $g$ the Landé factor.

Due to the Zeeman effect, different discrete values of energies are possible. These values depend on the different quantum number and can be determined thanks to Hund's rules. In figure A.2, J equals $5/2$ so $m_j$ can have 6 different values: $-5/2$, $-3/2$, $-1/2$, $1/2$, $3/2$ and $5/2$.

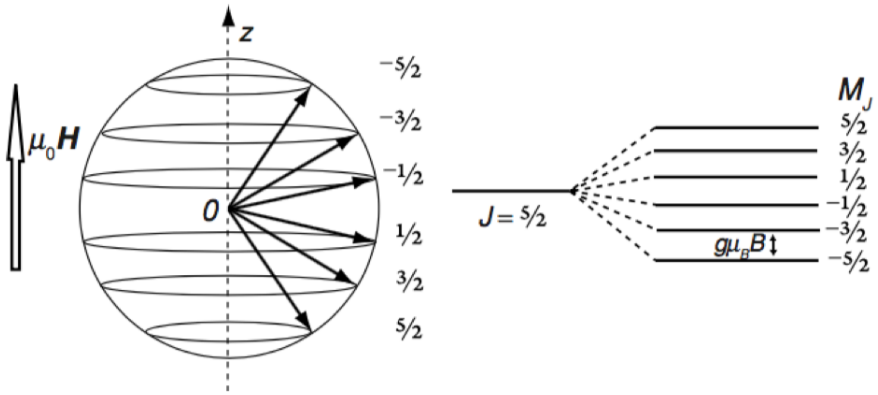


FIGURE A.2: Zeeman splitting for $J = 5/2$. [10]

The magnetisation is then described as:

$$M = \frac{N}{V} \sum_{m=-J}^{+J} \mu_z(m) \cdot P(m) \quad [\mathrm{A/m}]$$

with $P(m)$ the probability to find an ion in state m, which is function of the energy described just before. Finally after some development, the magnetisation appears to be:

$$M = \overbrace{\frac{N}{V} g_j \mu_b J}^{M_\infty} \overbrace{(\frac{2J+1}{2J}\text{coth}(\frac{2J+1}{2J} \cdot JX) - \frac{1}{2J}\text{coth}(\frac{JX}{2J}))}^{\text{Brillouin function } B_j(Y)} \quad [\text{A/m}]$$

with $Y = \frac{J\mu g_j B}{k_b T}$. Figure A.3 plots the Brillouin function as a function of Y.

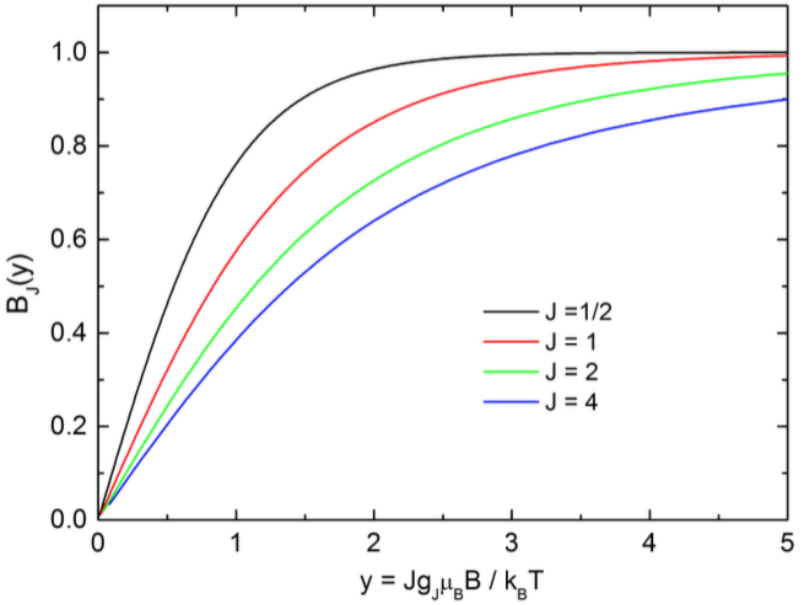


FIGURE A.3: Brillouin function. [27]

In the case of high temperature, and/or small magnetic field, $Y \to 0$, the magnetisation can be described as:

$$M = M_\infty \frac{g\mu_B JB}{3k_B T} \quad [\text{A/m}]$$

And from this result, the magnetic susceptibility appears to be:

$$\chi = \mu_0 \frac{M_\infty^2}{N/V} \frac{1}{3k_B T} \quad [\text{ - }] \tag{A.2}$$

Equation A.2 is also known as the Curie Law which shows that the magnetisation in inversely proportional to the temperature (Figure A.4). The value of $\chi$ is around $10^{-3}$.

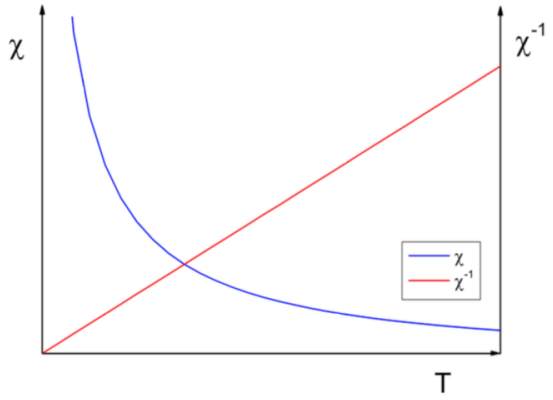


FIGURE A.4: Magnetic susceptibility as a function of temperature. Curie Law. [27]

The paramagnetic susceptibility arises from different contributions such as Langevin diamagnetic, Van Vleck and Pauli spin susceptibility, as well as the Landau susceptibility. Figure A.5 gives a summary of the different contributions and their relative importance.

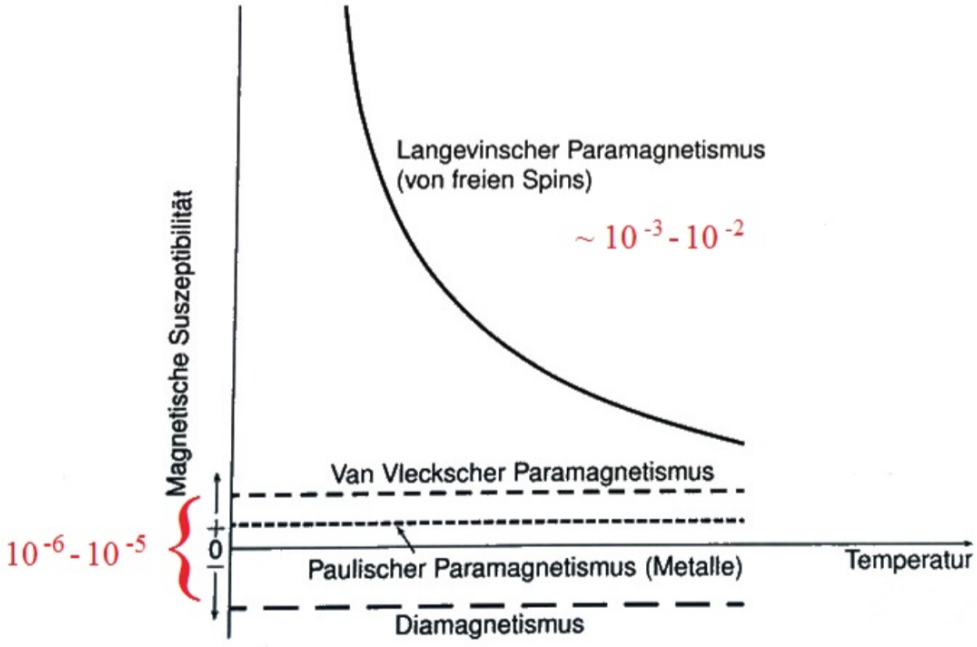


FIGURE A.5: Different contributions to the para- and dia-magnetic susceptibility. The Pauli susceptibility has only a small contribution. [10]

## A.2 Ferromagnetism

**Pauli Exclusion Principle** - The principle states that *no two Fermions, whose wavefunctions have non-zero overlap, can have exactly the same set of quantum number*. The quantum numbers $(n, l, m, s)$ are associated with total energy, orbital angular momentum, z-component of the angular momentum in a magnetic field, and the spin, respectively. This principle governs the behavior of all fermions (particles with half-integer spin). When we are dealing with a system of Fermions, the Symmetry Principle constrains us to accept the antisymmetric solution only.

**The Helium atom** - This element is used to study the Pauli exclusion principle in a simple way because it has only two electrons orbiting a nucleus.

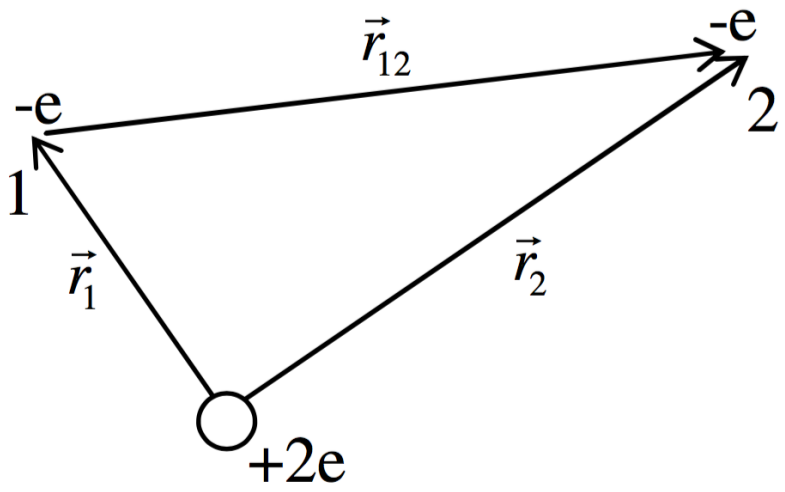


FIGURE A.6: Schematic of the Helium atom with the position of the nucleus and the two electrons. [5]

One consider a Helium atom composed of a heavy nucleus with charge $+2e$ and two surrounding electrons (figure A.6). The Hamiltonian of the Helium atom, taking into account the Coulomb attraction between each electron and the nucleus and the Coulomb repulsion between the electrons is given by:

$$\mathcal{H}_{He} = \frac{|\vec{p_1}|^2}{2m_0} + \frac{|\vec{p_2}|^2}{2m_0} - \frac{2e^2}{4\pi\epsilon_0|\vec{r_1}|} - \frac{2e^2}{4\pi\epsilon_0|\vec{r_2}|} + \frac{e^2}{4\pi\epsilon_0|\vec{r_{12}}|} \quad [\,\mathrm{J}\,] \tag{A.3}$$

where $\vec{p_1}$ and $\vec{p_2}$ are the momentum operators associated with electrons 1 and 2, respectively. Their spatial coordinates are denoted by $\vec{r_1}$ and $\vec{r_2}$, and $\vec{r_{12}} = \vec{r_1} - \vec{r_2}$. Equation A.3 can be written as $\mathcal{H}_{He} = \mathcal{H}_1 + \mathcal{H}_2 + \mathcal{H}_{int}$, where $\mathcal{H}_1$ and $\mathcal{H}_2$ stands for the hamiltonian of the separate atoms while $\mathcal{H}_{int}$ stands for the interaction hamiltonian between the two atoms. The possible energies of $\mathcal{H}_{He}$ are (a triplet state and a singlet state)[27]:

$$E^{\pm} = E_1 + E_2 + \int d^3r_1 \int d^3r_2 \phi^*_{\pm}(\vec{r_1}, \vec{r_2}) \mathcal{H}_{int} \phi_{\pm}(\vec{r_1}, \vec{r_2}) = 2E_0 + \frac{1}{1 \pm L^2}(C \pm A)$$

where C is the Coulomb integral, A the exchange integral and L the overlap integral. $J_{ij}$ describes the difference between energy states (triplet and singlet) associated with orbital (i,j) and $\overrightarrow{\sigma}$ the spin operator ($E^+ - E^- =: 2J$). Since $J_{ij}$ is positive, a parallele configuration (triplet state) has a lower energy than the anti-parallel configuration(singlet state).

Due to assumption, there is a small overlap and $L \longrightarrow 0$. One find the wavefunctions, which must be antisymmetric because we are dealing with fermions and because of the symmetry principle. This will determine the spin configuration. Finally, a spin dependent Hamiltonian is found to describe the ground state and first excited state. $\mathcal{H}^{spin} = J_0 - 2J\vec{s_1} \cdot \vec{s_2}$ with $J_0 = \frac{1}{4}(E^+ + 3E^-)$. This leads to the Heisenberg exchange term:

$$\mathcal{H} = -2J\vec{s_1} \cdot \vec{s_2}$$

The exchange energy term is truly quantum-mechanical in origin. It can be considered as an additional force ($F = \frac{dU}{dL}$) to the Coulomb force (positive repulsive force). The "exchange force" is positive for antiparrallel spin configuration (repulsion) and negative parallel spin congiguration

(attraction). For multiple particles the interpretation is more complicated. In the case of the Helium atom, the exchange energy term $J_{ij}$ is positive (antiparallel configuration), thus it increases the total energy.

Heisenberg proposed a scenario where ferromagnetism would come from exchange interaction between electrons. He proposed that the internal magnetic field in ferromagnets, arising from all spins within a domain lining up parallel to each other, could be linked to the presence of exchange coupling between neighboring ionic spins. For a given $J_{ij}$, if the lowest state of the Hamiltonian corresponds to all spins aligned, then this will account for the onset of ferromagnetism, since the lowest state corresponds to the ground state.

**Hartree-Fock approximation** - In the previous paragraph, a model with only two electrons was analysed. Here the case of many-body system comprising numerous electrons is considered. The many-body wavefunction of N interacting electrons is written as [5]:

$$\Psi = \Psi(\vec{r_1}s_1, \vec{r_2}s_2, ...\vec{r_N}s_N)$$

The *Variational Principle* states that if $\Psi$ is a solution of a many body Schrodinger equation, the quantity

$$< \mathcal{H} >= \frac{\Psi, \mathcal{H}\Psi}{\Psi, \Psi} \tag{A.4}$$

must be stationnary. The Hartree wavefunction is a product of wavefunction:

$$\Psi = \Psi(\vec{r_1}s_1, \vec{r_2}s_2, ...\vec{r_N}s_N) = \psi(\vec{r_1}s_1)\psi(\vec{r_2}s_2)...\psi(\vec{r_N}s_N)$$

This wavefunction however does not satisfy the Symmetry Principle which mandates that the sign of $\Psi$ should change if we interchange any of its two arguments. However, a wavefunction that does satisfy the Symmetry Principle is the *Slater determinant*.

$$\Psi = det \begin{pmatrix} \psi_1(\vec{r_1}s_1) & \psi_1(\vec{r_2}s_2) & ... & \psi_1(\vec{r_N}s_N) \\ \psi_2(\vec{r_1}s_1) & \psi_2(\vec{r_2}s_2) & ... & \psi_2(\vec{r_N}s_N) \\ . & . & ... & . \\ \psi_N(\vec{r_1}s_1) & \psi_N(\vec{r_2}s_2) & ... & \psi_N(\vec{r_N}s_N) \end{pmatrix} \tag{A.5}$$

This wavefunction satisfies the Pauli principle because it vanishes when $\psi_i = \psi_j$, showing that no two electrons can be put in the same state. It can be shown that if the energy in equation (A.4) is evaluated with the $\Psi$ given in equation (A.5), then the result is [5]:

$$\begin{aligned} < \mathcal{H} >= \sum_i \int d\vec{r}\psi_i^* \vec{r}(-\frac{\hbar^2}{2m^*})\psi_i\vec{r} \\ +\frac{1}{2}\sum_{i,j}\int d\vec{r}d\vec{r}\frac{e^2}{4\pi\epsilon|\vec{r}-\vec{r}|}|\psi_i(\vec{r})|^2|\psi_j(\vec{r})|^2 \\ -\frac{1}{2}\sum_{i,j}\int d\vec{r}d\vec{r}\frac{e^2}{4\pi\epsilon|\vec{r}-\vec{r}|}\delta_{s_i,s_j}\psi_i^*(\vec{r})\psi_i(\vec{r})\psi_j^*(\vec{r})\psi_j(\vec{r}) \end{aligned} \tag{A.6}$$

where $\delta$ is the Krönicker deltal indicating that the last term, which is the exchange term, is non-zero only between parallel spins. The second term is the Coulomb term. The exchang term is negative, and hence tends to lower the total energy. Evaluating $< \mathcal{H} >$ wiht the Slater determinant is known as the *Hartree Fock* approximation.

When minimizing equation (A.6), supposing that $\psi - s$ are plane waves, the total energy of N interacting electrons can be obtained.

$$E(\vec{k}) = \frac{\hbar^2 k^2}{2m^*} - \frac{e^2}{2\pi^2\epsilon} k_F f(\frac{k}{k_F}) \tag{A.7}$$

One need to summing the different energy tems (given in equation (A.7)) over all wavevector states $\vec{k}$ up to the Fermi wavvector $k_F$, multiply by 2 to account for the spin degeneracy, and then divide the last term by 2 to correct for double counting. The final result is:

$$E_N = [\frac{3}{5} E_F - \frac{3e^2 k_F}{16\pi^2\epsilon}] \quad [\,\mathrm{J}\,] \tag{A.8}$$

where N are the number of interacting electrons, $E_F$ the Fermi energy, $k_F$ is the Fermi wavevector the positive term is the Coulomb interaction, while the exchange term is negative because it tends to lower the total energy.

**The Bloch model of ferromagnetism** - The result of Hartree-Fock approximation (A.8) can explain ferromagnetism in a gas of electrons interacting through mutual Coulomb repulsion. In the result of Hartree-fock approximation, every state is assumed to be filled by two electrons of opposite spins, according to Pauli principle. In the case that the electron gas is completely spin polarised so that $N \uparrow = N$ and$N \downarrow = 0$. Then $E_N = E \uparrow$ and $k \uparrow = 2^{1/3} k_F$. As a result, for a completely spin polarised gas, we get:

$$E_N^{polarised} = N[\frac{3}{5} 2^{2/3} \frac{\hbar^2 k_F^2}{2m*} - 2^{1/3} \frac{3e^2 k_F}{16\pi^2\epsilon}] \quad [\,\mathrm{J}\,] \tag{A.9}$$

When doing the difference between the polarised state (A.9) and the unpolarised state (A.8), if the result is negative then the exchange term is larger than the first term, this mean that the polarised (ferromagnetic) state is preferred as the ground state. Generally speaking, low densities (smaller $k_F$) will favor the ferromagnetic state.

## A.3 GMR

### A.3.1 Development of the GMR definition

In figure 1.22, the overall resistance in the parallel configuration ($R_P$) and in the antiparallel configuration ($R_{AP}$) of the device can be expressed as:

$$\frac{1}{R_P} = \frac{1}{2R_{f,\uparrow} + 2R_n} + \frac{1}{2R_{f,\downarrow} + 2R_n} = \frac{2R_{f,\uparrow} + 2R_{f,\downarrow} + 4R_n}{(2R_{f,\uparrow} + 2R_n)(2R_{f,\downarrow} + 2R_n)}$$

$$\frac{1}{R_{AP}} = \frac{1}{R_{f,\uparrow} + R_{n,\uparrow} + R_{f,\downarrow}} + \frac{1}{R_{f,\downarrow} + R_{n,\downarrow} + R_{f,\uparrow}} = \frac{2}{R_{f,\uparrow} + 2R_n + R_{f,\downarrow}}$$

The spin injection efficiency is defined as:

$$\alpha = \beta \cdot \frac{R_f}{R_n} \cdot \frac{2}{2\frac{R_f}{R_n} + (1 - \beta^2)}$$

If $|\beta| = 100\%$, i.e. only majority spins (up-spins) are present in the ferromagnet, then $R_{f,\downarrow} \to \infty$ indicating that the resistance encountered by the (absent) minority spins (down-spins) is infinity. This would give a perfect spin polarisation in the initial current, and as a result a perfect spin injection efficiency, $\alpha = 1$.

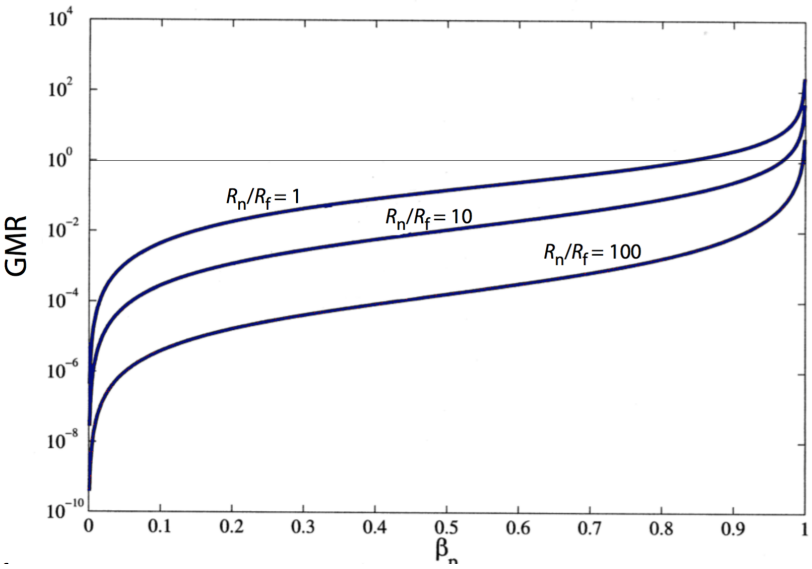


FIGURE A.7: GMR versus $\beta$. [21]

In a more realistic treatment, $\beta$ which is mostly dependent on the ratio $\frac{R_f}{R_n}$, is smaller than 1, as a consequence, $\alpha$ is massively reduced. This is known as the "resistor mismatch problem". $\alpha$ would approach $\beta$ if $R_f >> R_n$, but $R_f$ is usually much smaller than $R_n$.

The GMR can now be defined as:

$$\text{GMR} = \frac{R_{AP} - R_P}{R_P} = ... = \frac{\beta^2}{1-\beta^2}(\frac{R_f}{R_n})^2 \frac{4}{4(\frac{R_f}{R_n})^2 + 4(\frac{R_f}{R_n}) + (1-\beta^2)}$$

$$\approx \frac{\beta^2}{1-\beta^2} \quad \text{if} \quad R_n << R_f$$

Figure A.7 gives values of GMR as a function of $\beta$ for different values of $R_n/R_f$.

### A.3.2 Models for GMR measurements

Figure A.8 show a schematized presentation on how the current is going through a CIP configuration.

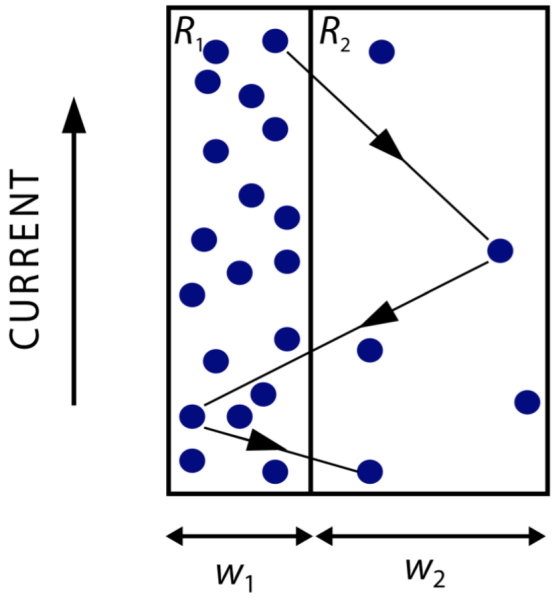


FIGURE A.8: Scattering process in CIP configuration. [21]

**2CSR model** - The 2CSR (two-current-series-resistance) equations hold when all layers are thinner than their spin-diffusion lengths. If scattering of electrons transiting a multilayer does not mix the moment up and down currents, then a 2C (two-current) model results. If, in addition, the spin-diffusion lengths in the ferromagnetic and non-magnetic layers are much longer than the layer thicknesses, an spin-flipping at interfaces is negligible, then for free electron Fermi surfaces and diffusive transport, it was shown that the CPP-MR should be given by a 2CSR model in which the total specific resistance $R_\uparrow$ and $R_\downarrow$ for each electron-moment direction is just the series sum of the specific resistance of each layer, and the specific resistance of each interface.

$$A\Delta R = \frac{n^2(\beta_F \rho_F^* t_F + \gamma_{F/N} 2AR_{F/N}^*)^2}{AR_{AP}}$$

**VF Model** - VF model, which is applied to thicker layers than the previous model, show that the same assumptions (free-electron Fermi surfaces and dominant diffusive scattering) that give the 2CSR model when $l_{sf}^F >> t_F$, and $l_{sf}^N >> t_N$, give more general equation that depend upon $l_{sf}^F$ and $l_{sf}^N$ when $l_{sf}^F \leq t_F$ and $l_{sf}^N \leq t_N$. The most general VF equations are so complex that they require numerical analysis. But the equations sometimes simplify enough for quantitative solution. This is an example that have been used to determine $l_{sf}^F$:

$$A\Delta R = \frac{(2\beta_F \rho_F^* l_{sf}^F + \gamma_{F/N} 2AR_{F/N}^*)^2}{2\rho_F^* l_{sf}^F + \rho_N t_N + 2AR_{F/N}^*}$$

where $AR_{F/N}^*$ is the specific resistance at the interface, $\beta$ a bulk spin asymmetry coefficient, $\gamma$ an interfacial spin asymmetry coefficient, and $\rho_F^*$ comes from:

$$\rho_{\uparrow(\downarrow)} = \frac{1}{\sigma_{\uparrow(\downarrow)}} = 2\rho_F^*[1 - (+)\beta]$$

**Electron mean free path vs spin flip scattering** For ferromagnetic metals, the spin-flip scattering due to electron-magnon collisions is frozen in the low temperature limit and the residual spin-flip scattering is due to spin orbit. It turns out, from figure A.9, that the $3d$ impurities are generally stronger spin-orbit scatterers than $s$ or $p$ impurities. For $3d$ elements the ratio between the spin-flip and non-spin-flip cross sections is around $10^{-2}$. As a consequence [32],

$$\frac{l_{sf}}{\lambda} \approx [\frac{\lambda_{sf}}{3\lambda}]^{1/2}$$

where $\lambda$ is the electron mean free path. Therefore, $l_{sf} \approx 10\lambda$ for structures composed of $3d$ elements with Cu or Ag. This shows that the condition $\lambda << l_{sf}$ is fulfilled in all the investigated sample of this thesis. Furthemore, the mean free path estimated to a few hundred angstrom in Cu layers, which means that the spin-diffusion length should amount to a few thousand angstrom. In the Co layers, even if the mean free path is somewhat shorter than in Cu, we are still expecting spin-diffusion lengths above $10^3$ Angstroms. In these conditions for all the samples with pure Cu spaces, the layer thickness $t$ should be definitely shorter than the spin-diffusion length, and the simple expression obtained for this limit can be applied.

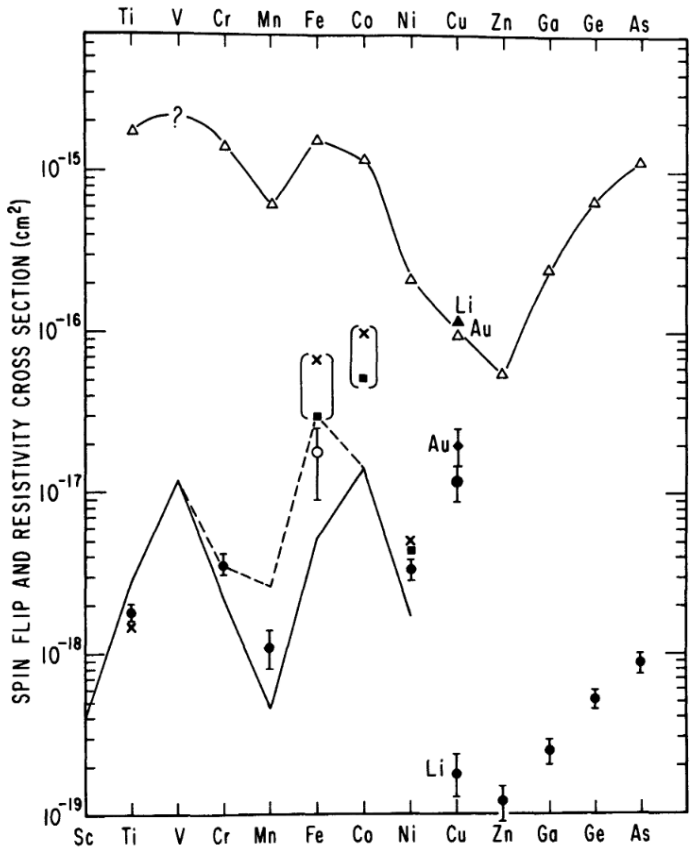


FIGURE A.9: Spin-flip cross-section (lower part) and resistivity cross section (triangles Δ, upper part) for transition impurities and s-p impurities in Cu. [32]

# Bibliography


[1] Elsie Araujo et al. "Artificially modified magnetic anisotropy in interconnected nanowire networks". In: *Nanoscale* 7.4 (2015), pp. 1485–1490. ISSN: 2040-3364, 2040-3372.

[2] Mario Norberto Baibich et al. "Giant magnetoresistance of (001) Fe/(001) Cr magnetic superlattices". In: *Physical review letters* 61.21 (1988), p. 2472.

[3] Célestin Lubaba Nkulu Banza et al. "High human exposure to cobalt and other metals in Katanga, a mining area of the Democratic Republic of Congo". In: *Environmental Research* 109.6 (Aug. 2009), pp. 745–752. ISSN: 00139351.

[4] A. E. Berkowitz et al. "Giant magnetoresistance in heterogeneous Cu-Co alloys". In: *Physical Review Letters* 68.25 (June 22, 1992), pp. 3745–3748. ISSN: 0031-9007.

[5] Marc Cahay. *Introduction to Spintronics*. Virginia Commonwealth University Richmond, U.S.A.: TCRC Press Taylor and Francis Group, 2008. 505 pp.

[6] Tristan da Câmara Santa Clara Gomes. *Magnetic and magneto-transport properties of 3D networks of interconnected magnetic nanowires*. 2016.

[7] Tristan da Camara Santa Clara Gomes et al. "3-D Interconnected Magnetic Nanofiber Networks With Multifunctional Properties". In: *IEEE Transactions on Magnetics* 53.11 (Nov. 2017), pp. 1–6. ISSN: 0018-9464, 1941-0069.

[8] Tristan da Câmara Santa Clara Gomes et al. "Interplay between the magnetic and magneto-transport properties of 3D interconnected nanowire networks". In: *Journal of Applied Physics* 120.4 (July 28, 2016), p. 043904. ISSN: 0021-8979, 1089-7550.

[9] Tristan da Câmara Santa Clara Gomes et al. "Magnetic and Magnetoresistive Properties of 3D Interconnected NiCo Nanowire Networks". In: *Nanoscale Research Letters* 11.1 (Dec. 2016). ISSN: 1931-7573, 1556-276X.

[10] J.M.D Coey. *Magnetism and magnetic materials*. OCLC: 819423378. Cambridge: Cambridge University Press, 2010. ISBN: 0-511-67743-X 978-0-511-67743-4 978-0-511-84500-0 0-511-84500-6 978-0-521-01676-6 0-521-01676-2 978-0-521-81614-4 0-521-81614-9.

[11] Michaël Darques et al. "Controlled changes in the microstructure and magnetic anisotropy in arrays of electrodeposited Co nanowires induced by the solution pH". In: *Journal of Physics D: Applied Physics* 37.10 (May 21, 2004), pp. 1411–1416. ISSN: 0022-3727, 1361-6463.

[12] J. De La Torre Medina et al. "Effects of layering on the magnetostatic interactions in microstructures of Co x Cu 1_x Cu nanowires". In: *Physical Review B* 77.1 (Jan. 14, 2008). ISSN: 1098-0121, 1550-235X.

[13] Marina Díaz-Michelena, Pedro Cobos, and Claudio Aroca. "Lock-in amplifiers for AMR sensors". In: *Sensors and Actuators A: Physical* 222 (Feb. 2015), pp. 149–159. ISSN: 09244247.

[14] Melinda J Duer. *Solid-state NMR: principles and applications*. OCLC: 322638015. Malden, MA: Blackwell Science, 2002. ISBN: 0-632-05351-8 978-0-632-05351-3.

[15] A. Encinas-Oropesa et al. "Dipolar interactions in arrays of nickel nanowires studied by ferromagnetic resonance". In: *Physical Review B* 63.10 (Feb. 15, 2001). ISSN: 0163-1829, 1095-3795.

[16] P. R. Evans, G. Yi, and W. Schwarzacher. "Current perpendicular to plane giant magnetoresistance of multilayered nanowires electrodeposited in anodic aluminum oxide membranes". In: *Applied Physics Letters* 76.4 (Jan. 24, 2000), pp. 481–483. ISSN: 0003-6951, 1077-3118.

[17] A. Fert and Luc Piraux. "Magnetic nanowires". In: *Journal of Magnetism and Magnetic Materials* 200.1 (1999), pp. 338–358.

[18] P. J. Flanders. "An alternating-gradient magnetometer (invited)". In: *Journal of Applied Physics* 63.8 (Apr. 15, 1988), pp. 3940–3945. ISSN: 0021-8979, 1089-7550.

[19] J. A. Gifford et al. "Continuous control of spin polarization using a magnetic field". In: *Applied Physics Letters* 108.21 (May 23, 2016), p. 212401. ISSN: 0003-6951, 1077-3118.

[20] R. Gross and A. Marx. *Lecture notes on Spintronics*. 2005.

[21] German Hammerl. *Lecture Notes Spintronics*. 2017.

[22] John C. Hulteen and Charles R. Martin. "A general template-based method for the preparation of nanomaterials". In: *Journal of Materials Chemistry* 7.7 (1997), pp. 1075–1087.

[23] Guwahati IIT. *Spin dependent scattering and transport*. NPTEL. 2013. URL: http://nptel.ac.in/courses/115103039/module6/lec13/2.html (visited on 05/21/2018).

[24] *ipPORE membranes*. it4ip. URL: https://www.it4ip.be/en/membranes/standard-filter-membranes/ (visited on 05/31/2018).

[25] Pascal Jacques. *LMAPR2642-Characterisation of inorganic materials*. 2017.

[26] M. Venkata Kamalakar et al. "Temperature dependent electrical resistivity of a single strand of ferromagnetic single crystalline nanowire". In: *Applied Physics Letters* 95.1 (July 6, 2009), p. 013112. ISSN: 0003-6951, 1077-3118.

[27] Hans-Albrecht Krug von Nidda. *Lecture notes Magnetism*. 2017.

[28] Aurélien Lherbier. *Quantum electronic transport*. 2018.

[29] Isao Mannari. "Electrical Resistance of Ferromagnetic Metals". In: *Progress of Theoretical Physics* 22.3 (1959).

[30] Max Headroom. *Introduction To Solid State Physics 8th Edition By Charles Kittel*. 2014.

[31] T. McGuire and R. Potter. "Anisotropic magnetoresistance in ferromagnetic 3d alloys". In: *IEEE Transactions on Magnetics* 11.4 (July 1975), pp. 1018–1038. ISSN: 0018-9464.

[32] P. Monod and S. Schultz. "Conduction electron spin-flip scattering by impurities in copper". In: *Journal de Physique* 43.2 (1982), pp. 393–401. ISSN: 0302-0738.

[33] Manuel Müller. "Finite Size Effects of the Anisotropic Magnetoresistance". In: (2017), p. 79.

[34] Ahmed El-Nemr, ed. *New developments in electrodeposition and pitting research, 2007*. Trivandrum: Transworld Research Network, 2007. 245 pp. ISBN: 978-81-7895-304-5.

[35] Werner Pepperhoff and Mehmet Acet. *Constitution and Magnetism of Iron and its Alloys*. Google-Books-ID: 4BfpCAAAQBAJ. Springer Science & Business Media, Mar. 9, 2013. 230 pp. ISBN: 978-3-662-04345-5.

[36] Luc Piraux. *LMAPR2471 Transports phenomena in solids and nanostructure*. 2018.

[37] Luc Piraux. *MAPR1492 Physique des matériaux*. 2013.

[38] *PMC MicroMag 2900 Series AGM | Overview | Lake Shore Cryotronics, Inc.* 2018. URL: https://www.lakeshore.com/products/Vibrating-Sample-Magnetometer/PMC-MicroMag-2900-Series-AGM/Pages/Overview.aspx (visited on 04/05/2018).

[39] R. C. Bell, D. T. Zimmerman, and N. M. Wereley. *Impact of Nanowires on the Properties of Magnetorheological Fluids and Elastomer Composites.* OCLC: 884028481. INTECH Open Access Publisher, 2010. ISBN: 978-953-7619-88-6.

[40] A. Ramazani, M. Almasi Kashi, and A. H. Montazer. "Fabrication of single crystalline, uniaxial single domain Co nanowire arrays with high coercivity". In: *Journal of Applied Physics* 115.11 (Mar. 21, 2014), p. 113902. ISSN: 0021-8979, 1089-7550.

[41] Conrad Rizal, Belaid Moa, and Boris B. Niraula. "Ferromagnetic Multilayers: Magnetoresistance, Magnetic Anisotropy, and Beyond". In: *Magnetochemistry* 2.2 (Apr. 16, 2016), p. 22.

[42] Stephen Roberts and Gus Gunn. "Cobalt". In: *Critical Metals Handbook*. Ed. by Gus Gunn. Oxford: John Wiley & Sons, Dec. 27, 2013, pp. 122–149. ISBN: 978-1-118-75534-1 978-0-470-67171-9.

[43] Mordechay Schlesinger and Milan Paunovic, eds. *Modern electroplating*. 5th ed. The electrochemical society series 52. Hoboken, NJ: Wiley, 2010. 729 pp. ISBN: 978-0-470-16778-6.

[44] Simen O. Sopp. *Magnetotransport properties of interconnected magnetic nanowires and multilayers*. 2017.

[45] C Tannous and J Gieraltowski. "The Stoner–Wohlfarth model of ferromagnetism". In: *European Journal of Physics* 29.3 (May 1, 2008), pp. 475–487. ISSN: 0143-0807, 1361-6404.

[46] *The History and Working Principle of the Scanning Electron Microscope (SEM)*. AZoNano.com. Mar. 19, 2015. URL: https://www.azonano.com/article.aspx?ArticleID=3995 (visited on 04/04/2018).

[47] T Valet and A Fert. "Theory of the perpendicular magnetoresistance in magnetic multilayers". In: (), p. 15.

[48] V Vega et al. "Tuning the magnetic anisotropy of Co–Ni nanowires: comparison between single nanowires and nanowire arrays in hard-anodic aluminum oxide membranes". In: *Nanotechnology* 23.46 (Nov. 23, 2012), p. 465709. ISSN: 0957-4484, 1361-6528.

[49] T. M. Whitney et al. "Fabrication and magnetic properties of arrays of metallic nanowires". In: *Science* 261.5126 (1993), pp. 1316–1319.

Rue Archimède, 1 bte L6.11.01, 1348 Louvain-la-Neuve **www.uclouvain.be/epl**